國 立 交 通 大 學

光電工程研究所

博 士 論 文

具耳語廊模態之光子晶體共振腔元件特性之研究

Researches on Photonic Crystal Microcavities and Devices Based on Whispering-Gallery Modes

研 究 生：盧贊文

指導教授：李柏璁　教授

中 華 民 國 九 十 八 年 七 月

具耳語廊模態之光子晶體共振腔元件特性之研究

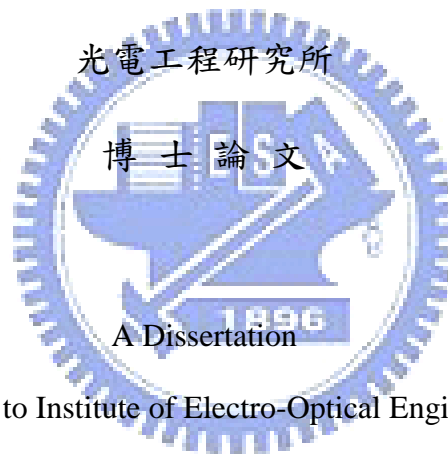# Researches on Photonic Crystal Microcavities and Devices Based on Whispering-Gallery Modes

研 究 生：盧贊文　　　　Student：Tsan-Wen Lu

指導教授：李柏璁　博士　　Advisor：Dr. Po-Tsung Lee

國 立 交 通 大 學

光 電 工 程 研 究 所

博 士 論 文

A Dissertation

Submitted to Institute of Electro-Optical Engineering

College of Electrical Engineering and Computer Science

National Chiao Tung University

in partial Fulfillment of the Requirements

for the Degree of Doctor of Philosophy

in

Electro-Optical Engineering

July 2009

Hsinchu, Taiwan, Republic of China

中 華 民 國 九 十 八 年 七 月

具耳語廊模態之光子晶體共振腔元件特性之研究

學生：盧贊文

指導教授：李柏璁 博士

國立交通大學光電工程研究所博士班

摘　　要

耳語廊模態所具有的高 Q 值與其多方向性共振是十分適合整合於積體光路中作為光源或具有特定功用的被動元件。在本論文中，我們設計、製作、量測並分析各種具有耳語廊模態的光子晶體共振腔元件特性，並探討其可能的應用。

論文一開始我們介紹了二維光子晶體共振腔元件相關的研究方法，包括數值模擬、製程技術以及量測系統。首先，本論文基於一種八對稱準光子晶體設計具有耳語廊模態的奈米共振腔，並在有限時域差分模擬與實驗上探討耳語廊模態的雷射特性、旁模抑制機制以及極小的元件尺寸。此外，論文中也探討一種新穎且具有等向均勻性光能隙的環形光子晶體，並設計出具有高 Q 值耳語廊模態的微共振腔雷射元件。

利用具有高對稱性的十二對稱準光子晶體晶格，我們設計具有高 Q 值的耳語廊模態雷射共振腔，並探討模態對共振腔邊界的強烈依存性，同時我們也進一步設計並探討多共振腔耦合的雷射元件。而由於耳語廊模態的分佈特性，吾人可以在該共振腔下製作一奈米柱作為電激發結構中的電流導路以及散熱器。透過製作不同尺寸的奈米柱，我們在模擬與實驗上探討由奈米柱所造成耳語廊模態的光學衰減與熱導改善特性。

基於整合在一般光子晶體積體光路的理由，我們將準光子晶體共振腔的共振腔邊界移植到一般光子晶體共振腔中以增強其中的耳語廊模態。藉由耳語廊模態的存在，我們探討了在不同共振腔-波導耦合排列下的均勻光耦合特性。而在應用上，我們提出並探討將此共振腔設計於雙層結構上，以作為高靈敏度光學應力偵測器的可能。最後，我們在正方晶格光子晶體上設計一具有最低階耳語廊模態的奈米共振腔，此耳語廊模態在具有較小模態體積的同時，同時具有較大的共振腔下奈米柱容許度。

Researches on Photonic Crystal Microcavities and Devices Based on Whispering-Gallery Modes

student：Tsan-Wen Lu

Advisors：Dr. Po-Tsung Lee

Institute of Electro-Optical Engineering,
National Chiao Tung University

Abstract

Whispering-gallery (WG) mode with high quality (Q) factor and multi-directional resonance is very suitable for serving as the active laser sources and passive devices with specific functionalities in photonic integrated circuits (PICs). In this dissertation, we design, fabricate, and characterize various photonic crystal (PhC) based micro- and nano-cavities with high Q WG modes. The possible applications are also investigated and discussed.

In the beginning of this dissertation, we introduce the related research resources for researches on two-dimensional PhC cavity devices, including numerical simulation methods, nano-fabrication processes, and measurement systems. At first, we propose a nanocavity design with WG mode based on 8-fold quasi-PhC (QPhC). Various WG modal properties are addressed both in experiments and simulations, including single mode lasing actions, side mode reduction mechanism, compact device size, and so on. Besides, we also investigate a novel circular-PhC (CPhC) lattice structure with isotropic photonic band gap effect and characterize the designed CPhC microcavity with high Q WG mode.

By using 12-fold QPhC lattice structure with high symmetry, we design a microcavity with high Q WG mode. WG mode lasing actions and the strong mode dependence on microcavity boundary are confirmed. Due to the WG mode field distribution, we insert a nano-post beneath the microcavity to serve as the current injection pathway and heat sink in electrically-driven structure. By fabricating microcavities with different nano-post sizes, we investigate the WG modal loss behaviors and heat sink improvement due to nano-post both in experiments and simulations.

For the purpose of integration in PhC-based PICs, we project the 12-fold microcavity boundary on a PhC microcavity and enhance a high Q WG mode in it. Due to the presence of WG mode, we investigate the uniform coupling properties of different waveguide-cavity

geometries. In applications, we propose a double-layered structure based on above PhC microcavity and investigate its possibility in serving as an optical stress sensor. In the end, we propose a nanocavity design with lowest order WG mode based on square PhC lattice. This WG mode can be with very small mode volume and large nano-post tolerance beneath the nanocavity at the same time.

Acknowledgements

Table of Contents

Table Captions

Chapter 4

Chapter 5

Figure Captions

Chapter 1

Chapter 2

Chapter 3

Chapter 4

Chapter 5

Chapter 1

Introduction

1-1 Micro-Photonics

Over last several decades, the silicon based VLSI technologies have made the microprocessors possible and lead to great success in high-speed electrical information processing. However, when the gate line-width further decreases, the performances toward high-speed processing will be limited to the resistance of the very tiny metal inside the microprocessors or systems and lead to large RC constant, high power and poor thermal dissipations, signal distortion and degradation, and cross talk between channels.

To overcome these problems, the researchers began to develop the optical communication and information processing systems in recent decades, that is, to replace electrons by photons. The wavelength division multiplexing (WDM) system [1] based on optical fibers has shown the potentials in high-speed processing since 1980's due to the low interactions between photons. Over 40 Gb / s communication rate has been achieved in recent years [2].

Due to the great success in WDM systems, researchers impatiently to promote them to be system-on-chip and make lots of efforts in recent decades in realizing the photonic integrated circuits (PICs) [3] with versatile functionalities, which are usually composed by optical waveguides and cavities in micrometer scale. Generally, optical waves in these devices are optically confined or guided by total-internal-reflection (TIR) effect.

Unfortunately, when researchers further promote the component size to the order of single wavelength, serious optical losses due to the limitation of ray optics greatly degrade their abilities in photon guiding and controlling. The concept of photonic crystal (PhC) with

photonic band gap (PBG) effect proposed by E. Yablonovitch and S. John in 1987 [4, 5] overcome the limitation and show another chance to realize the PICs in wavelength scale.

1-2 Photonic Crystal

In a narrow sense, the PhCs [6] can be regarded as the dielectric materials with periodic index arrangement on the order of an optical wavelength, which can be classified into one-, two-, and three-dimensional (1-, 2-, and 3-D) PhCs according to their periodic dimensions. Actually, the 1D PhC has been widely applied in various optical device known as Bragg distributed reflector, which is a steak of two dielectric materials with different refractive indices and can be fabricated by various thin film fabrication processes. Due to large design flexibility and easy to fabricate, 2D PhCs are the most widely used in various optical applications among these three kinds of PhCs. On the other hand, up to date, due to the complicated periodic structures of 3D PhCs, most researchers make their efforts on the fabrication methods and technologies instead of applications. In this dissertation, we will focus our researches on the 2D PhCs.

The photon behaviors in such dielectric periodic structures can be illustrated and understood by solving Maxwell's equations. The equations in MKS unit are listed as below:

$$\nabla \bullet \vec{B} = 0 \tag{1-1}$$

$$\nabla \bullet \vec{D} = \rho \tag{1-2}$$

$$\nabla \times \vec{E} = -\frac{\partial \vec{B}}{\partial t} \tag{1-3}$$

$$\nabla \times \vec{H} = \vec{J} + \frac{\partial \vec{D}}{\partial t} \tag{1-4}$$

where the terms of B, D, E, H, J, and ρ are magnetic induction field, displacement, macroscopic electric and magnetic fields, currents, and free charges in space, respectively.

There are some assumptions to simplify the following calculations: 1). The dielectric material is isotropic and leads to the relationship of $D(r, \omega) = \varepsilon(r, \omega)E(r, \omega)$, where the term of $\varepsilon(r, \omega)$ is determined by the given dielectric periodic structure, that is, the given PhC. 2). The frequency dependence of the dielectric material can be ignored, that is, $D(r) = \varepsilon(r)E(r)$. 3). The dielectric material is loss-less, that is, $\varepsilon(r)$ will be a real value. 4). The dielectric material is non-magnetic, that is, $B(r) \sim H(r)$. 5). No free charge exists in the space, that is, J and ρ are both equal to zero. Under these assumptions, equations (1.1) - (1.4) become the following equations:

$$\nabla \cdot \vec{H}(r,t) = 0 \tag{1-5}$$

$$\nabla \cdot \varepsilon(r)\vec{E}(r,t) = 0 \tag{1-6}$$

$$\nabla \times \vec{E} = -\frac{\partial \vec{H}(r,t)}{\partial t} \tag{1-7}$$

$$\nabla \times \vec{H} = \varepsilon(r)\frac{\partial \vec{E}(r,t)}{\partial t} \tag{1-8}$$
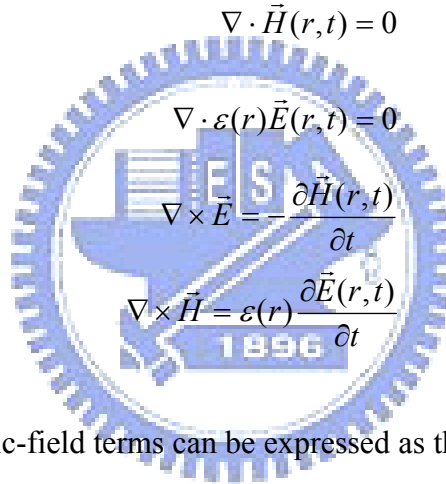
The electric- and magnetic-field terms can be expressed as the harmonic modes, which are products of terms with spatial and time function separately. The terms of $E(r, t)$ and $H(r, t)$ become as the following:

$$\vec{H}(r,t) = \vec{H}(r)e^{i\omega t} \tag{1-9}$$

$$\vec{E}(r,t) = \vec{E}(r)e^{i\omega t} \tag{1-10}$$

Thus, substituting equations (1-9) and (1-10), equations (1.5) - (1.8) further become the following equations:

$$\nabla \bullet \vec{H}(r) = 0 \tag{1-11}$$

3

$$\nabla \bullet \varepsilon(r)\vec{E}(r) = 0 \qquad\qquad (1\text{-}12)$$

$$\nabla \times \vec{E}(r) - i\omega\vec{H}(r) = 0 \qquad\qquad (1\text{-}13)$$

$$\nabla \times \vec{H} - i\omega\varepsilon(r)\vec{E}(r) = 0 \qquad\qquad (1\text{-}14)$$

And then we can obtain the master equation for magnetic field as the following:

$$\nabla \times (\frac{1}{\varepsilon(r)}\nabla \times \vec{H}(r)) = \frac{\omega^2}{c^2}\vec{H}(r) \qquad\qquad (1\text{-}15)$$

For a given PhC lattice structure, that is, a given *ε(r)* denotes the dielectric constant variation function in space, we can solve the master equation to find the modes *H(r)* for a given frequency, which is an eigen-value problem. And then the corresponding *E(r)* term can be obtained by substituting *H(r)* term into equation (1-14). From the solved eigen-values, we can construct the relationship between wave-vector and permitted optical wave frequencies of a given PhC, that is, the band diagram of PhC.

In specific frequency range, we will find the solved *H(r)* terms in some or all wave vectors will be with an exponential decay term, that is, the optical wave propagation in this frequency range is forbidden. Actually, this unique PBG effect is very similar to the electrical band-gap in crystalline solid materials illustrated by Shördinger's equation. In crystalline solid materials, in specific energy range, the electron existence possibility will become zero due to the potential function provided by the periodic atom arrangement and form the electrical band gap. Interestingly, the electron and periodic atom arrangement in
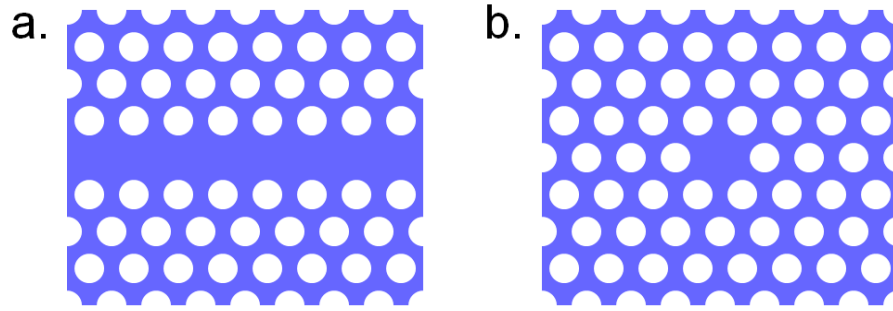
Fig. 1-1: Schemes of (a) line-defect for waveguide and (b) point-defect for cavity based on 2D triangular PhC lattice structure.

crystalline solid material can be analog to the photon and periodic index arrangement in PhC, respectively, and leads to the similar band gap effect.

Most importantly, the PBG effect provides researchers the abilities of controlling photon flows on the order of an optical wavelength by inducing defects in PhCs, for example, PhC waveguides and cavities, as shown in Fig. 1-1(a) and (b) based on 2D triangular PhC lattice. Due to the strong optical confinements in wavelength scale provided by PBG effect, various PhC-based optical devices have been proposed and demonstrated like raging fires in the past couple decades.

1-3 Photonic Crystal Micro- and Nano-Cavities

In micro-photonics researches, due to the ability of confining photon flow with specific frequency, optical microcavities [7] have long been the key components in active and passive optical micro-systems, for example, micro laser sources, optical filters, micro-sensors and detectors, micro-polarizers, optical buffers, and so on. Various TIR-confined microcavities, for example, micro-disks, micro-rings, and micro-toroids [7], have shown the excellent performances in above applications. However, most device sizes are quite large (> 100 μm) and not compact enough to realized PICs operating in wavelength scale. Although the device size can be down to several micrometers, the
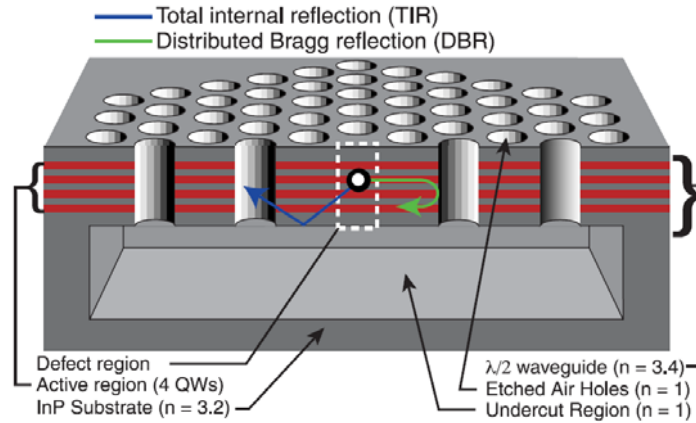
Fig. 1-2: Scheme of 2D PhC nanocavity firstly demonstrated by O. Painter *et al.* [8]

performances will degrade with the decreased device size.

On the other hand, in PhCs, researchers can easily create a point-defect region as shown in Fig. 1-1(b) and form a micro- or nano-cavity on the order of wavelength. Due to the PBG effect, the photon flow will not suffer serious bend losses due to TIR effect and can be well-confined in these wavelength-scale PhC micro- or nano-cavities. The scheme of firstly demonstrated 2D PhC nanocavity laser by O. Painter *et al.* [8] is shown in Fig. 1-2. The PhC lattices are composed by air holes on a suspended thin dielectric slab (with quantum wells) in the air. The nanocavity region is form by a missing air hole. Light will be confined inside the nanocavity by in-plane and vertical optical confinement provided by PBG and waveguide TIR effect, respectively. The slab thickness is designed to be half of one wavelength to support transverse-electrical fundamental mode in the vertical planar waveguide (air-slab-air) structure.

In very recent years, various active and passive 2D PhC micro- and nano-cavity design and applications has been proposed and demonstrated. Researchers have made efforts on several issues of basic optical properties of micro- and nano-cavities, including high quality (Q) factor, ultra-small mode volume (V), large spontaneous emission (β) factor, and so on. Recently, high theoretical and measured Q factors of 5×10^9 and 3×10^6 in passive nanocavities

have been achieved by Prof. M. Notomi's group [9] and Prof. S. Noda's [10] group, respectively. On the other hand, Prof. T. Baba's group [11, 12] and Prof. Y. H. Lee's group [13] also propose and demonstrated ultra-small mode volume close to $(\lambda/2n)^3$ from PhC nanocavities by shifting the lattice locally. Due to the high Q factor and small mode volume V, the resulted ultra-high Q/V value are very suitable for observing quantum electro-dynamics phenomenon, for example, vacuum Rabi splitting [14], and opto-mechanical energy transformation [15, 16]. On the other hand, PhC micro- and nano-cavities have also been regarded as a potential laser source with high β factor [17] for optical communication system and efficient single photon source [18]. Besides, due to the high Q factor and condensed device size, PhC micro- and nano-cavities are also expected for various highly sensitive micro-sensors or micro-sensor array, including index-sensing [19, 20, 21, 22], virus detection [23], stress sensing [24, 25], photo-detectors [26], and so on.

In constructing PICs, PhC cavities also play the key roles. There have been various ultra-high Q micro- and nano-cavities integrated with PhC waveguides to lead-in or lead-out the light with resonance frequency of nanocavity from or to the waveguides. In this manner, the nanocavity acts like an optical transistor. This integration on the order of wavelength can be used in add/drop filters [27, 28], optical bi-stable switches [29, 30], WDM PICs [31], slow-light devices for optical buffer [32, 33, 34], all-optical memory devices [35], and so on, which are all the key components in constructing PICs with versatile functionalities.

1-4   Motivations and Dissertation Overview

For serving as an active source, although various PhC micro- and nano-cavities with excellent properties have been reported and demonstrated as we mentioned in Chapter 1-3, most of them are under optical excitation and lack of proper electrically-driven structure. One promising and efficient approach is injecting current by a post structure like the approach of

micro-disk [36]. Undoubtedly, the whispering-gallery (WG) mode with large central field node will be the best mode candidate. However, the WG modes are rarely sustained in PhC-based micro- and nano-cavities [37, 38]. Besides, the multi-directional mode profile would also be beneficial and increase the design flexibility when applied in PICs. Thus, we will focus our researches on designing various quasi-PhC and PhC micro- and nano-cavities sustaining high Q WG modes and their optical properties. And this dissertation structure is illustrated as the following.

In Chapter 2, at first, we will introduce the essential research resources in designing, fabricating, and characterizing PhC micro- and nano-cavity laser devices, including numerical method in simulations, standard nano-fabrication processes on InP-based semiconductor material, and near-infrared micro-photoluminescence system with various accessories.

In Chapter 3, 8-fold QPhC and circular-PhC lattice structure with PBG effects will be introduced and applied in designing D_1 nanocavity and D_2 microcavity sustaining high Q WG modes, which are demonstrated and confirmed both in FDTD simulations and experiments. Except for the basic WG mode lasing actions, modal properties including side-mode reducing mechanism, compact device size, and isotropic PBG effect are also investigated by different experiments or simulations.

And then the 12-fold QPhC D_2 microcavity design sustaining high Q WG mode is investigated in Chapter 4 both in simulations and experiments. To examine the possibility of electrically-driven QPhC microcavity laser under continuous-wave operation, by fabricating various nano-posts beneath the microcavity, the influences on optical losses and thermal properties improvement of WG mode are investigated by a series of simulations and experiments.

In Chapter 5, for the purpose of easy to integrate in PhC-based PICs, we design a PhC CD_2 microcavity based on cavity geometry in 12-fodl QPhC D_2 microcavity in Chapter 4. The WG mode lasing action is confirmed and the coupling properties when the microcavity

integrating with different waveguides are investigated in experiments and simulations. Base on above CD_2 microcavity design, we propose an idea of microcavities on a double-layered structure to act like a highly sensitive optical stress sensor. Design rule and simulated results are analyzed and discussed. We also propose a D_0 nanocavity design based on square PhC lattice. The sustained lowest order WG mode with ultra-small mode volume is investigated in simulations.

In Chapter 6, we summarize our works on PhC-based micro- and nano-cavities sustaining high Q WG modes.

Modeling, Fabricating, and Characterizing Photonic Crystal Micro- and Nano-Cavity Lasers

In this chapter, we introduce our developed research resources for designing, fabricating, and characterizing photonic crystal (PhC) based light emitting devices, including numerical method in simulations, standard nano-fabrication processes on InP-based semiconductor material, and near-infrared (NIR) micro-photoluminescence (micro-PL) system with various accessories for different measurement purposes.

2-1   Numerical Methods

In designing PhC devices, the plane-wave expansion (PWE) and finite-difference time-domain (FDTD) methods are widely used to calculate the band diagrams of given PhC and light wave behaviors in various PhC devices. Due to wide developments in electro-magnetic wave applications, for researchers, commercial software and tools based on these methods have been available in recent years, for example, R-Soft [39], Photon Design [40], and so on. For briefly illustrating the algorism of PWE and FDTD method, several important equations in Chapter 1 are listed here again, including (1-5) - (1-8), and (1-15).

Maxwell's equations:

$$\nabla \cdot \vec{H}(r,t) = 0 \tag{2-1}$$

$$\nabla \cdot \varepsilon(r)\vec{E}(r,t) = 0 \tag{2-2}$$

$$\nabla \times \vec{E} = -\frac{\partial \vec{H}(r,t)}{\partial t} \qquad (2\text{-}3)$$

$$\nabla \times \vec{H} = \varepsilon(r)\frac{\partial \vec{E}(r,t)}{\partial t} \qquad (2\text{-}4)$$

Master equation:

$$\nabla \times (\frac{1}{\varepsilon(r)}\nabla \times \vec{H}(r)) = \frac{\omega^2}{c^2}\vec{H}(r) \qquad (2\text{-}5)$$

2-1-1 Plane-Wave Expansion Method

As we mentioned before, we can obtain the dispersion curve of a given PhC by solving the master equation (2-5) from Maxwell's equations by formulating an eigen-value problem out of it. And the PWE method provides a computational technique in this task. Because the master equation is time-independent, the solution is the stationary state of the given PhCs. And the algorism is illustrated briefly as the following.

In a given crystalline solid material, when we calculate the electronic band by Shördinger equation, the potential function provided by the atom periodic arrangement can be expressed by Fourier expansion. And one can suppose the electronic wave function is in the form of Bloch wave. Thus, we can obtain the allowed eigen-energy states as a function of its kinetic momentum, that is, the electronic band structure. Due to the electronic wave function is expressed as a superposition of plane waves, this method is named as plane-wave expansion.
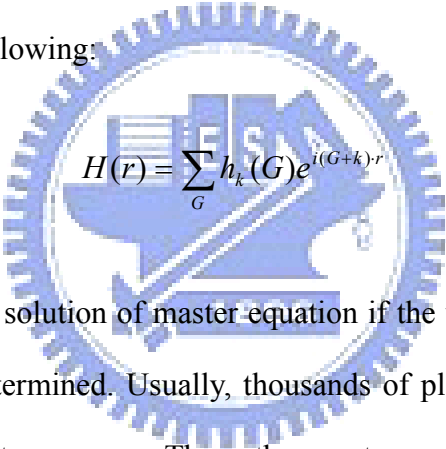
As we mentioned before, PhC and its photonic bands can be regarded as the optical analog of solid crystalline material and its electronic bands. Thus, the same derivation can be applied to PhCs. The potential function in solid crystalline is replaced by the periodic dielectric index constant expressed as:

$$\varepsilon(r) = \sum_{m=-\infty}^{\infty} K_{m,n}^{\varepsilon} e^{iG\cdot r} \qquad (2\text{-}6)$$

where G is the reciprocal lattice vector of the given PhC lattice and the Fourier series coefficient being the K numbers subscripted by m. However, due to the symmetries of PhC in space, including translational, rotational, and mirror symmetries [6], we can define the smallest repeat region of the PhC, that is, the unit cell, to describe the entire lattice structure and shorten the time consumption in calculation. Thus, the equation (2-6) becomes:

$$\varepsilon(r) = \sum_G \varepsilon_G e^{iG \cdot r} \text{, where } \varepsilon_G = \frac{1}{V_C} \int_{unit\_cell} \varepsilon(r) e^{-iG \cdot r} \tag{2-7}$$

where V_C is the volume of the unit cell. And the magnetic field $H(r)$ can be expressed in the form of Bloch wave as the following:

$$H(r) = \sum_G h_k(G) e^{i(G+k) \cdot r} \tag{2-8}$$

The term of $H_k(r)$ will be the solution of master equation if the vector amplitude $h_k(G)$ of the plane wave $(k+G)$ can be determined. Usually, thousands of plane waves will be applied in algorism to obtain sufficient accuracy. Thus, the master equation (2-5) become as the following by substituting (2-7) and (2-8):

$$(k+G) \sum_{G'} \varepsilon_{G,G'}^{-1} (k+G') h_k(G') = -(\frac{\omega}{c})^2 h_k(G') \tag{2-9}$$

where $\varepsilon^{-1}_{G, G'}$ is the Fourier coefficients of $\varepsilon(r)$ and $\varepsilon^{-1}(r)$ on the plane wave with wave vector (G'-G). By standard matrix diagonalization method, we can solve equation (2-9) and obtain the photonic band diagram.

2-1-2　Finite-Difference Time-Domain Method

Since 1990's, FDTD techniques have emerged as primary means to computationally model scientific and engineering problems dealing with electromagnetic wave interactions in various materials and structures, including PhCs. Comparing with PWE method, FDTD method is used to directly solve the time-dependent Maxwell's equations, the equations (2-3) and (2-4) in partial differential form. In Cartesian coordinates, these two equations can be derived as six scalar equations in (2-10), (2-11), and (2-12) [41]. The equations will be discretized using central-difference approximations to the space and time partial derivatives to obtain the dynamic behaviors of photon flow in PhC devices.

$$\frac{\partial E_x}{\partial t} = \frac{1}{\varepsilon}(\frac{\partial H_z}{\partial y} - \frac{\partial H_y}{\partial z}), \quad \frac{\partial H_x}{\partial t} = \frac{1}{\varepsilon}(\frac{\partial E_z}{\partial y} - \frac{\partial E_y}{\partial z}) \tag{2-10}$$

$$\frac{\partial E_y}{\partial t} = \frac{1}{\varepsilon}(\frac{\partial H_x}{\partial z} - \frac{\partial H_z}{\partial x}), \quad \frac{\partial H_y}{\partial t} = \frac{1}{\varepsilon}(\frac{\partial E_x}{\partial z} - \frac{\partial E_z}{\partial x}) \tag{2-11}$$

$$\frac{\partial E_z}{\partial t} = \frac{1}{\varepsilon}(\frac{\partial H_y}{\partial x} - \frac{\partial H_x}{\partial y}), \quad \frac{\partial H_z}{\partial t} = \frac{1}{\varepsilon}(\frac{\partial E_y}{\partial x} - \frac{\partial E_x}{\partial y}) \tag{2-12}$$

The basic FDTD space grid and time-stepping algorithm are proposed by Kane Yee in IEEE Transactions on Antennas and Propagation in 1966 [42]. In spatial domain, he proposed the vector components of the *E*- and *H*-field stagger spatially in rectangular unit cells of a Cartesian computational grid, which is named as "Yee cell" and shown in Fig. 2-1. In Yee cell, each *E*-field vector component is located midway between a pair of *H*-field vector components, and conversely.

On the other hand, in equation (2-4), the change in the *E*-field in time is dependent on the change in the *H*-field across space. Thus, in the simulation domain, the updated value of the *E*-field in time is dependent on the stored value of the *E*-field and the numerical curl of the local distribution of the *H*-field in space. The *H*-field is also in the similar time-stepping manner. Iterating the *E*- and *H*-field updates results in a marching-in-time process wherein

sampled-data analogs of the continuous electromagnetic waves under consideration propagate in a numerical grid stored in the computer memory. K. Yee proposed a leapfrog scheme for above marching-in-time progress as shown in Fig. 2-2. In Fig. 2-2, the *E*- and *H*-field updates are staggered in time domain sequentially. As a result, the *E*-field updates will be conducted midway during each time-step between successive *H*-field updates, and conversely. This process can be expressed as the following equations:

$$E_{z(i,j,k)}^{n+1} = E_{z(i,j,k)}^{n} + \frac{\Delta t}{\varepsilon \Delta x}(H_{y(i,j+1,k)}^{n+1/2} - H_{y(i,j,k)}^{n+1/2}) - \frac{\Delta t}{\varepsilon \Delta y}(H_{x(i,j,k+1)}^{n+1/2} - H_{x(i,j,k)}^{n+1/2}) \qquad (2\text{-}13)$$

$$H_{z(i,j,k)}^{n+1/2} = H_{z(i,j,k)}^{n-1/2} + \frac{\Delta t}{\mu \Delta y}(E_{x(i,j,k)}^{n} - E_{x(i,j,k-1)}^{n}) - \frac{\Delta t}{\mu \Delta x}(E_{y(i,j,k)}^{n} - E_{y(i,j-1,k)}^{n}) \qquad (2\text{-}14)$$
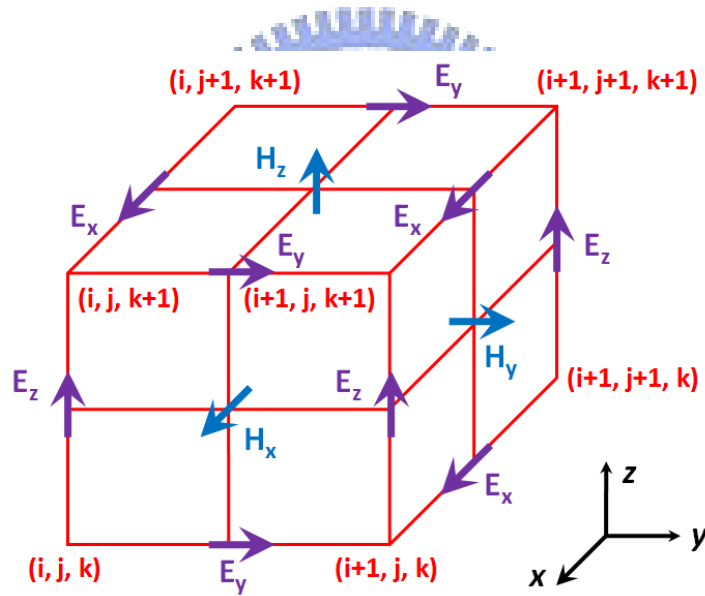
Fig. 2-1: Schemes of Yee cell in FDTD algorism.
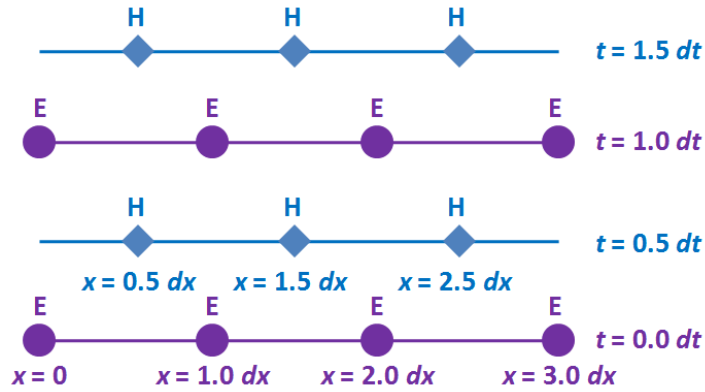
Fig. 2-2: Scheme of leapfrog time-stepping in FDTD algorism.

Another key issue in FDTD algorism is the boundary condition. To approximate an infinite domain to be a finite computational domain and save the computation time and computer memory, various boundary conditions are proposed, including Mur's Boundary, perfectly matched layer, and absorbing boundary condition, which all eliminate the reflections when the wave impinge the boundary of the computational domain.

In summary, the resulting finite-difference equations are solved in a grid deviation in spatial domain and leapfrog manner in time domain. In the computations, the E-field components inside the Yee cell in space will be manipulated at a given instant in time domain. And then the H-field components in the same cell will be manipulated at the next instant in time domain. The process will be repeated until the desired electro-magnetic field behavior is fully evolved. Since it is a time-domain method, solutions can cover a wide frequency range with a single simulation run. In this dissertation, we will simulate and design the PhC-based devices based on above two methods by commercial software [39].

2-1-3　Simulation of Photonic Crystal Device

Based on above numerical methods, in this section, we calculate the photonic band diagram and the PBG effect of two-dimensional (2D) triangular PhC lattice shown in Fig.
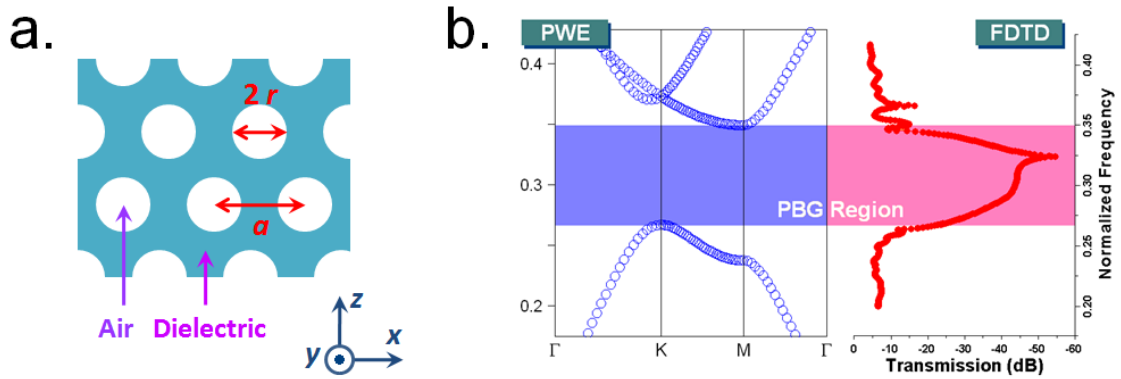
Fig. 2-3: (a) Scheme of 2D triangular PhC lattice and (b) the corresponding PWE and FDTD simulated PBG effect.

2-3(a), which is composed by air holes on dielectric slab with infinite thickness. The indices of dielectric material and air hole are set to be 2.7 and 1.0. The lattice constant (a) and air hole radius (r) are set to be 500 and 150 nm, respectively. The calculated band diagram for transverse-electrical (*TE*) polarization is shown in Fig. 2-3(b). We can observe a large PBG region between the first (dielectric-band) and second (air-band) allowed photonic band. Besides, we can also directly simulate the optical wave (usually a plane wave or Gaussian dipole source in simulation) transmission through the PhC by FDTD method to locate the PBG region. The simulated transmission spectrum is shown in Fig. 2-3(b). In Fig. 2-3(b), the low transmission region indicates the PBG effect, which agrees with that performed by PWE method quite well. Although the FDTD method is much time-consumed than PWE method, this approach will be very promising in calculating PhC lattice structures cannot define the unit cell or be with very large unit cell, for example, the quasi-PhCs.

On the other hand, to investigate the designed PhC micro- and nano-cavities, the FDTD simulation will be applied very often to obtain the resonance spectrum, quality (Q) factor, effective mode volume, and so on. The Q factor is a very important parameter to evaluate the optical confinement ability of a microcavity. In FDTD simulations, there are two main approaches to evaluate the Q factors of resonance modes. The first one is directly recording

the energy decay rate of the resonance mode to evaluate the optical loss and calculate the Q factor by the following equation:

$$U(t) = U_o \exp(-\frac{2\pi\omega t}{Q})$$

(2-15)

where ω denotes the resonance frequency. Obviously, for microcavity with ultra-high Q factor, the evaluation process needs great amount of time steps in FDTD simulation to obtain sufficient accuracy in exponential fitting, which is usually time-consuming and executed by cluster computations. The other approach evaluates Q factor by the resonance line width in frequency domain base on Padé approximation [43] and Fourier harmonic analysis, which provide a fast and better frequency resolution can be obtained without using longer simulation times.

Besides, the effective mode volume can be evaluated by the following equation [8]:

$$V_{eff} = \frac{\int_V \varepsilon(r)|E(r)|^2 d^3r}{\max[\varepsilon(r)|E(r)|^2]}$$

(2-16)

Here, we take optimized high Q PhC L_3 microcavity [44] proposed by Prof. S. Noda's group for example, to verify the accuracy of the simulation tools we use. The scheme of optimized L_3 microcavity design by three missing air holes is shown in Fig. 2-4(a). The microcavity is optimized by shifting lattices A, B, and C with $0.2a$, $0.025a$, and $0.2a$ outward, respectively, as shown in Fig. 2-4(a). The lattice constant, r/a ratio, slab thickness and index are set to be 420 nm, 0.29, 240 nm, and 3.4, respectively, according to reference [44]. The simulated resonance spectrum and the main resonance mode profile in electrical field are shown in Fig. 2-4(b), which agree with the results in reference [44]. The Q factor and effective mode volume are calculated to be 2.3×10^5 and 0.079 μm^3, which also agree with
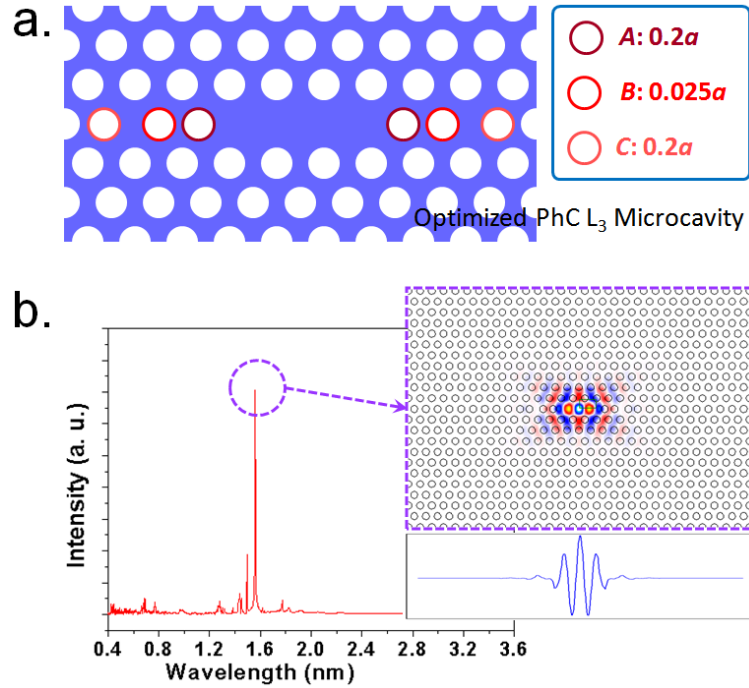
Fig. 2-4: (a) Scheme of optimized high Q PhC L_3 microcavity. (b) 3D FDTD simulated resonance spectrum and main resonance mode profile in electric field.

2.6×10^5 and 0.071 μm^3 in reference [44] quite well and verify the accuracy of the used simulation tools.

2-2 Nano-Fabrication of Two-Dimensional Photonic Crystal Cavities

The epitaxial structure of InGaAsP multi-quantum-wells (MQWs) for membrane structure is shown in Fig. 2-5. The epitaxial wafer consists of four 10 nm 0.85 % compressively-strained InGaAsP quantum wells which are separated by three 20 nm unstrained InGaAsP barrier layers. The summated thickness of MQWs is 220 nm, which is design for supporting single *TE* fundamental mode near wavelength of 1550 nm. It has been confirmed that the PL spectrum of the MQWs is centered at 1500 nm with 200 nm gain spectrum at room temperature, as shown in Fig. 2-5. The 60 nm InP capping layer is used to protect the MQWs during a series of dry etching processes.
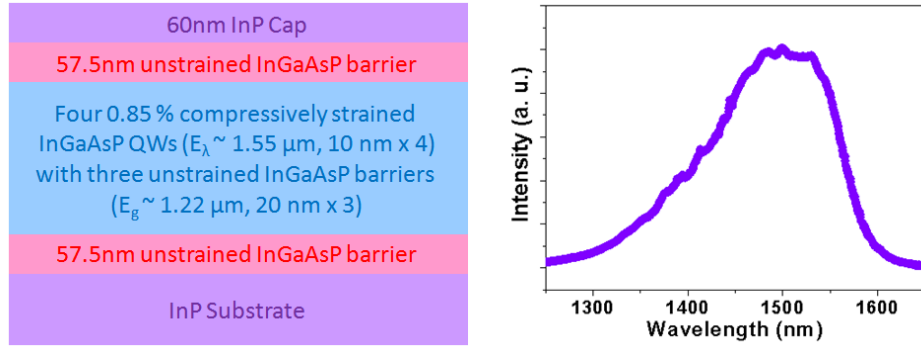
Fig. 2-5: Designed epitaxial structure of InGaAsP MQWs, which is grown by Union Optronics Corporation, Taiwan. The PL spectrum centered near 1550 nm with 200 nm spectral span is also confirmed.

The nano-fabrication process of 2D PhC microcavity is illustrated as the following. First, the 140 nm silicon-nitride (Si_3N_4) layer served as hard mask for latter dry etching process is deposited by plasma-enhanced chemical vapor deposition (PECVD) process. Then a 240 nm polymerthylmethacrylat (PMMA) layer is spin-coated on the Si_3N_4 layer. The PhC pattern is defined on the PMMA layer by electron beam lithography technology (JSM-6500F, JEOL). After a series of development and fixation processes, the first mask for PhC pattern is prepared. The PhC pattern can be observed in scanning electron microscopy (SEM) picture shown in the inset *A* in Fig. 2-6. It is also worthy to note that we can gradually tune the PhC lattice cell size, that is, the air hole radius by choosing different point dosages during the electron-beam lithography process [45-47].

Second, for transferring the defined PhC pattern on PMMA mask into Si_3N_4 and InGaAsP MQWs, the inductively coupled plasma / reactive ion etching (ICP / RIE) system (Plasmalab-100, Oxford Inc.) is used. The Si_3N_4 hard mask is etched by CHF_3 / O_2 mixed gas in RIE mode, and then CH_4 / Cl_2 / H_2 mixed gas is used to transfer the patterns into MQWs at 150 °C in ICP etching mode. The cross-section SEM pictures of etched PhC lattice on Si_3N_4 and InGaAsP MQWs are shown in the insets *B* and *C* in Fig. 2-6, respectively.
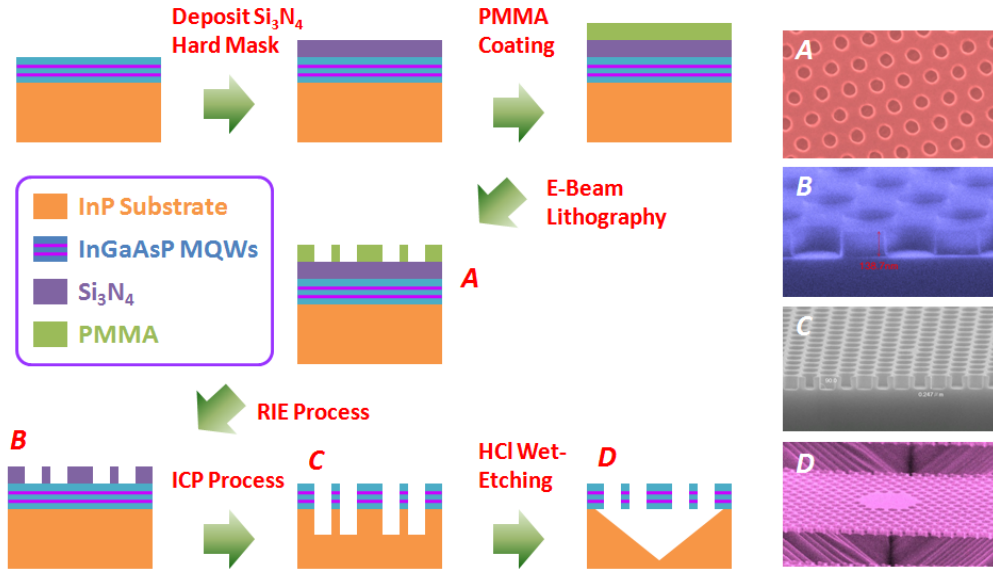
Fig. 2-6: The overview of the fabrication process of 2D PhC microcavity. The insets *A* to *D* show the SEM pictures of each PhC pattern transferring step during the fabrication process.

Third, to form the suspended slab structure, the InP substrate beneath the MQWs should be removed. The undercut can be achieved by using a mixture of HCl : H_2O = 4 : 1 at 2 °C. This process also removes the Si_3N_4 residue and the 60 nm InP capping layer and smoothes the surface and the sidewall of the air holes. This process could be also regarded as a gentle wet etching process to reduce the scattering, i.e. optical loss, caused by the surface roughness [48]. The wet etching process is anisotropic. The wet etching stops at 95° and 40° from <-1, 0, 0> direction in the (0, -1, -1) and (0, 1, -1) planes, respectively [49]. The undercut trench under the PhC pattern can be formed for the larger air holes. For smaller air holes, the wet etching results in a small wedge-shape undercut in each air hole. The small wedges under every air hole have no chance to meet each other. As a result, no undercut trench can be formed. Thus, a window opening surrounds the device is applied to prevent the wet etching of the air holes from stopping. Then a 2D PhC suspended slab structure is completed, as shown in the inset *D* in Fig. 2-6.

2-3   Measurement Setup

2-3-1   Near-Infrared Micro-Photoluminescence System

To characterize the epitaxial materials and various fabricated PhC micro- and nanocavities, a NIR confocal micro-PL system with sub-micrometer-scale resolution in microscope and sub-nanometer-scale resolution in spectrum is setup. The system configuration and photo of the micro-PL system are illustrated and shown in Fig. 2-7(a) and (b).

In this system, an 845 nm transistor-transistor logic (TTL) laser (APMT-60 ,Power Technology Inc.) is used as the pump source. This TTL laser can be operated both under pulse operation and continuous-wave (CW) operation. In pulse mode, the driving current output from a DC power source will be modulated by a function generator (DG-535,
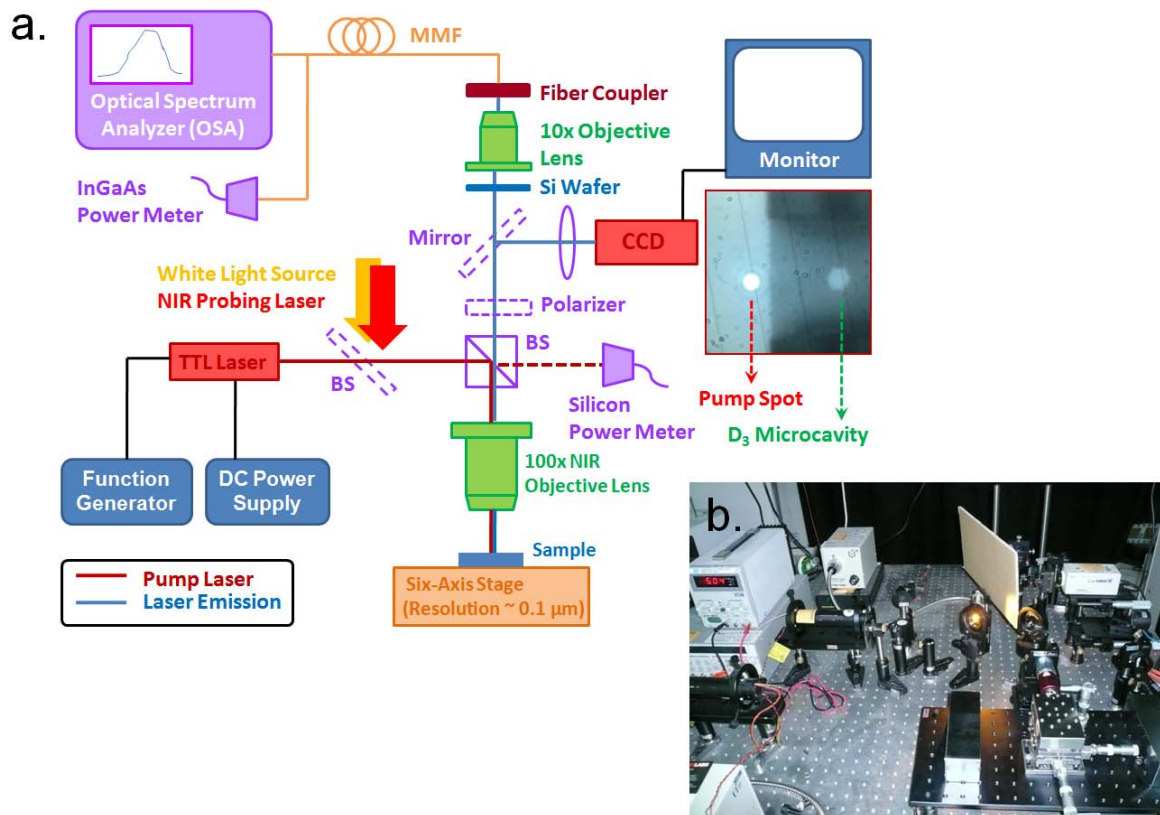
Fig. 2-7: (a) Scheme and (b) photo of NIR con-focal micro-PL system setup.

Stanford Inc.), and then the laser light output will be under pulse operation. The pulse signal is generated by time-differential between two logic gate outputs and the pulse width of 200 fs can be achieved. However, the smallest achievable pulse width is limited to the summation of rise and fall time of the laser diode in TTL laser, which is about 19 ns. In CW operation case, the function generator is turned off and the internal circuit is short. In this case, the driving current will not be modulated and the laser output is in CW wave. Besides, the TTL laser output profile and beam divergence are shaped to a circle and collimated by its internal shaping module and mounted output collimator, respectively. These will be beneficial for the optical path alignment when setting up the system.

The TTL laser pump beam is split into two beams by a 50 / 50 beam splitter with 10 μm thickness (BP-150, Throlab. Inc.). One beam will be feed into a 100x long working distance NIR objective lens (M-Plan APO NIR series, Mitsutoyo Corp.) with numerical aperture of 0.42 mounted on a 3-axis stage. And then the pump beam is focused to a spot with 3 to 2.5 μm in diameter on the measured sample by the objective lens. The incident laser power on the sample will be estimated by detecting the other beam by a silicon power meter (1815-C, Newport Inc.), as shown in Fig. 2-7.

The simple microscopic function is also setup in this micro-PL system. By using a co-axial white light source and a charge-coupled device (CCD) camera, the sample mounted on a high resolution 3-axis stage can be observed from the monitor. A typical PhC D_3 microcavity (formed by removing 19 missing air holes, cavity size ~ 2.6 μm in diameter) image captured by CCD camera is shown in the inset photo in Fig. 2-7(a). In this photo, the PhC microcavity laser can be observed clearly. One can see the positions of the microcavities and the 845 nm pump spot with 2.5 to 3 μm in diameter can be determined by comparing with the microcavity. By the 3-axis stage (561-series, Newport Inc.) with high resolution of 0.1 μm, the pump spot can be moved to the region we want to excite.

Once the sample is excited, the objective lens will collect the output light from the top
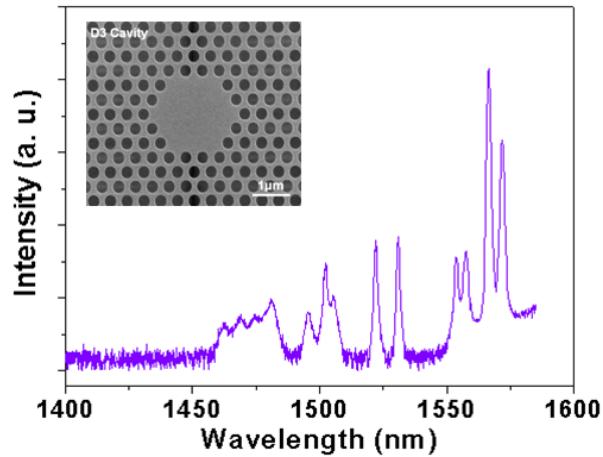
Fig. 2-8: The measured resonance spectrum from PhC D_3 microcavity laser. The SEM picture of Ph D_3 microcavity is also shown in the inset.

of the sample. A silicon wafer is put after the beam splitter in order to block the reflected pump laser light. We use a 10x objective lens to feed the output signal into a FC / FC multimode fiber (MMF), and then detecting the signal by an optical spectrum analyzer (OSA) (AQ-6315A ,Ando Inc.) and an InGaAs power meter (Q8221, Advantest Inc.), respectively. The spectral resolution of the OSA is 0.05 nm and detection responsibility is from 350 to 1700 nm. By this NIR micro-PL system, the PL spectrum of the InGaAsP MQWs can be obtained, as shown in Fig. 2-5. Besides, we also measure a typical PhC D_3 microcavity [50, 51] to verify the system setup. The measure resonance spectrum is shown in Fig. 2-8. The lasing peak is at 1595 nm and not shown in Fig. 2-8. The measured resonance peaks agree with the simulated mode in PhC D_3 microcavity [50] quite well.

2-3-2 Systematic Accessories

For different purposes of measurement, we setup different system and sample stage accessories including substrate temperature controlling system for thermal behaviors investigation, current injection platform for electrically-driven devices, in-plane laser emission collection stage for waveguide-type laser devices, NIR tuning probe system for
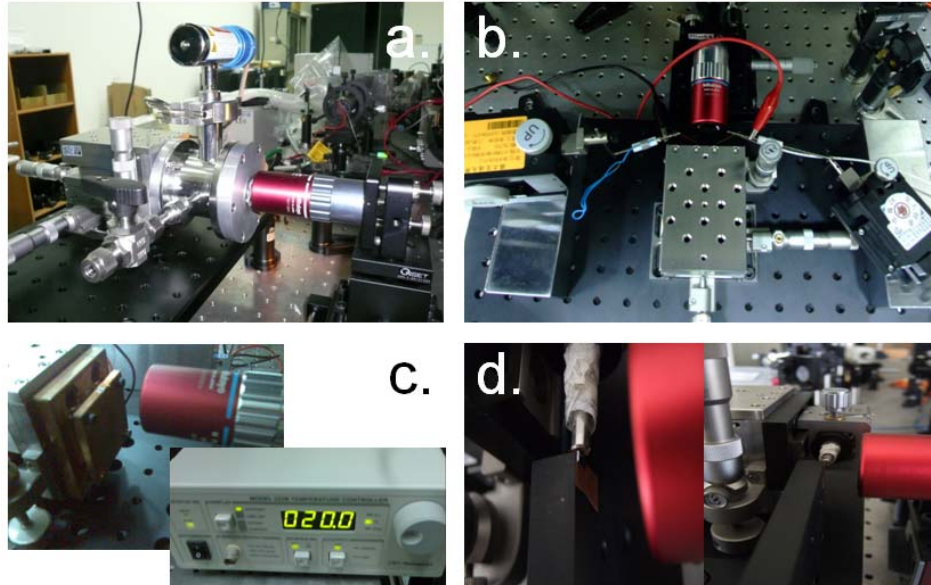
Fig 2-9: Various sample stage accessories of NIR con-focal micro-PL system, including (a) gas detection chamber, (b) current injection platform, (c) substrate temperature controlling system, and (d) in-plane laser emission collection stage.

reconfigurable laser investigations, gas detection chamber for sensor device measurements, and so on. The photos of these accessories are shown in Fig. 2-9(a)-(d).

Among these accessories, the substrate temperature controlling system will be applied in Chapter 4 in this dissertation and the setup is illustrated as the following. We design a substrate temperature controlling system by clapping a thermo-electric cooler (TEC) between two copper slabs. The sample will be fixed on the top copper slab. Thus, we can control the sample substrate temperature by controlling the top copper slab temperature. In this system, a 10 kΩ thermistor with ± 0.01 °C accuracy is used to monitor the temperature of the top copper slab. The thermistor feedbacks data to the temperature controller (325-B, Newport Inc.) to decide the TEC driving current. A stable temperature will be achieved in 10 seconds.

2-4   Summary

In this chapter, at first, we introduce the theories of numerical methods for designing PhC devices, including PWE and FDTD methods. And then we illustrate our developed

nano-fabrication processes for fabricating PhC micro- and nano-cavity devices on InP-based semiconductor materials, which are composed by e-beam lithography technology, a series of dry- and wet-etching processes. We also setup a NIR con-focal micro-PL system with high spectral resolution and sensitivity to characterize the fabricated devices. And various systematic accessories for different measurements are also setup.

<div align="right">

Chapter 3

</div>

8-Fold Quasi-Photonic Crystal Nanocavity & Circular Photonic Crystal Microcavity with Whispering-Gallery Modes

In this chapter, at first, we briefly introduce the lattice structures and photonic band gap (PBG) effects of quasi-photonic crystals (QPhCs). And then we propose a D_1 nanocavity design with well-confined whispering-gallery (WG) mode based on 8-fold QPhCs under proper cavity modification. In experiments and simulations, including WG modal lasing actions, side mode reducing mechanism, and compact device size are investigated. In additions, we also investigate a novel circular-PhC (CPhC) lattice structure with isotropic PBG effect and apply it to construct a microcavity sustaining high quality (Q) WG mode.

3-1   Quasi-Photonic Crystals

Since the PhC nanocavity laser was firstly demonstrated by O. Painter *et al.* in 1999 [8], various attractive designs have been widely investigated as we mentioned in Chapter 1. With the PBG effect, well-controlled photon flows in PhC micro- and nano-cavities are extremely potential for quantum-electron dynamics (QED) devices and photonic integrated circuits (PICs) applications due to its ultra-high Q factor and ultra-low threshold. However, the anisotropy of PBG caused by the low-level symmetry in wave-vector (k) space has been found and investigated [52, 53]. Actually, higher-level symmetry can be obtained by the idea of quasi-periodic lattice comes from the solid-state physics and the anisotropy of PBG can be reduced. According to different symmetry level, various QPhC lattice structures have been proposed and demonstrated, for example, penrose (5-fold) [54], octagonal (8-fold) [55],
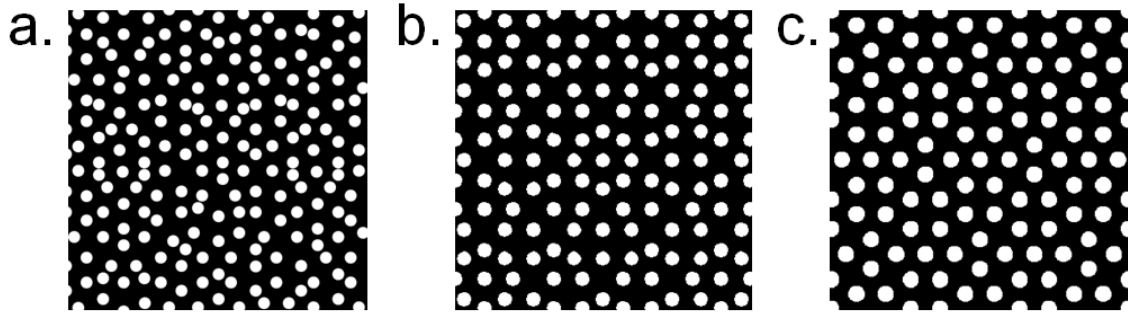
Fig. 3-1: Lattice structures of (a) penrose (5-fold), (b) octagonal (8-fold), and (c) dodecagonal (12-fold) QPhCs.

dodecagonal (12-fold) [56], and so on, as shown in Fig. 3-1. These lattice structures in spatial coordinates can be obtained by transforming specific periodic wave-vector arrangements in Fourier space [56].

In serving as the mirror of microcavity, the QPhCs would provide more efficient and uniform in-plane confinement in all directions due to the isotropic PBG effects [54, 56], which will be beneficial for achieving lasing properties with low threshold and high Q factor. Most importantly, various WG modes with high Q factors can be easily sustained in 2D micro- and nano-cavities based on different QPhCs. Very recently, various QPhC micro- and nano-cavity lasers have been investigated in theory and demonstrated in experiments by several groups [57-59].

3-2　8-Fold Quasi-Photonic Crystal Single-Defect Nanocavity

3-2-1　Cavity Design, Simulated, and Measured Modal Properties

In the beginning, we design a single defect nanocavity by removing a central air hole (named D_1 nanocavity) based on 8-fold QPhC lattice as shown in Fig. 3-2(a). Then we investigate the sustained defect modes in this nanocavity by three-dimensional (3D) finite-difference time-domain (FDTD) method. In the simulation setup, the slab thickness is 220 nm and the designed air-hole radius (r) over lattice constant (a) ratio is 0.3. From
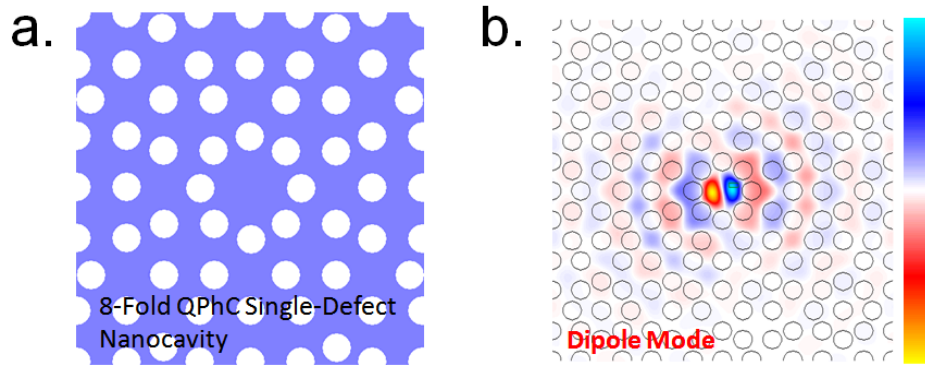
Fig. 3-2: (a) Scheme of original 8-fold QPhC D_1 nanocavity by removing a central air hole and (b) the sustained dipole mode profile in magnetic field by FDTD simulation.
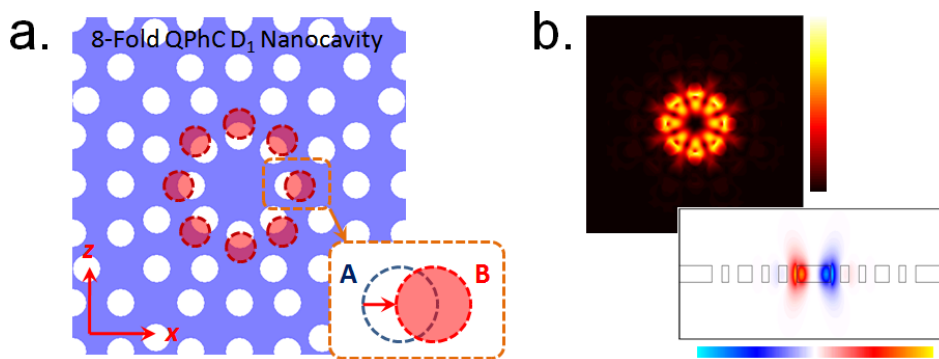
Fig. 3-3: (a) Scheme of 8-fold QPhC D_1 nanocavity by shifting the eight nearest air holes from original positions A to B. (b) FDTD simulated $WG_{4, 1}$ mode profiles in electrical field in x-z and x-y planes well-sustained in 8-fold QPhC D_1 nanocavity with modification.

the simulated results, we find the main resonance mode in this nanocavity design is dipole mode as shown in Fig. 3-2(b).

In order to obtain a well-confined WG mode, the eight nearest air holes are shifted outward from position A to position B as shown in Fig. 3-3(a) until the distance between two neighboring air holes is equal to the lattice constant. This design approach actually comes from the micro-gear lasers [60], where the gears at the cavity boundary have to satisfy the constructive interference condition for the standing wave of WG mode. From FDTD simulations, we successfully create a well-confined $WG_{4, 1}$ mode (the former sub-number denotes the azimuthal number and the latter one denotes the order of radial mode) in the modified 8-fold QPhC D_1 nanocavity. The simulated electrical fields in x-z and x-y planes

with significant zero-field distribution are shown in Fig. 3-3(b). The number of mode lobes matches with the number of gears as we predicted.

According to the nanocavity design, the real devices are fabricated by the standard fabrication process illustrated in Chapter 2-2. The top-view scanning-electron-microscope (SEM) picture of the fabricated 8-fold QPhC D_1 nanocavity is shown in Fig. 3-4(a). The fabricated r/a ratio is 0.30 with lattice constant of 550 nm. In characterization, the nanocavity is optically pumped by the NIR micro-PL system illustrated in Chapter 2-3. The light-in light-out (L-L) curve and the typical lasing spectrum at room temperature of a 8-fold QPhC D_1 nanocavity with r/a ratio of 0.30 are shown in Fig. 3-5(a) and (b). The threshold can be estimated as low as 0.35 mW. The lasing wavelength is 1499 nm with 25 dB side-mode suppression ratio (SMSR). The measured Q factor is about 7,500, which is estimated from the measured line-width of 0.20 nm near the transparency pump power. In order to identify the lasing mode, we fabricate various devices with different r/a ratios from 0.25 to 0.34. The measured wavelengths of the lasing mode quite agree with the 3D FDTD calculated resonant frequencies of $WG_{4,1}$ mode, as shown in Fig. 3-6. Hence, we can identify the lasing mode as $WG_{4,1}$ mode.
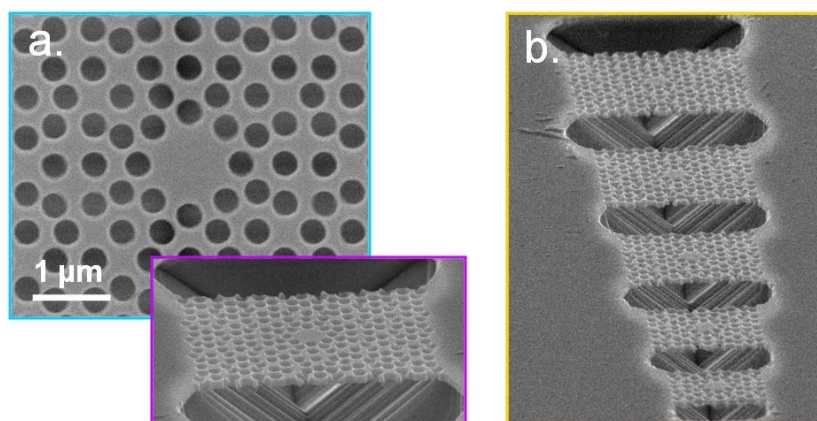
Fig. 3-4: (a) Top-view SEM picture of the designed 8-fold QPhC D_1 nanocavity. The inset shows its titled-view image. (b) Titled-view SEM image of 8-fold QPhC D_1 nanocavities with lattice periods of eight to four from top to bottom.
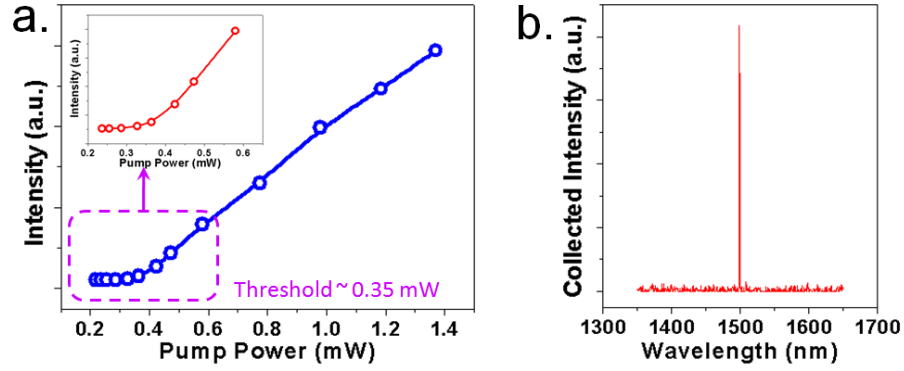
Fig. 3-5: (a) The measured *L-L* curve of 8-fold QPhC D_1 nanocavity. The inset shows the *L-L* curve near threshold and indicates its threshold as low as 0.35 mW. (b) The measured lasing spectrum at 1499 nm with SMSR of 25 dB.
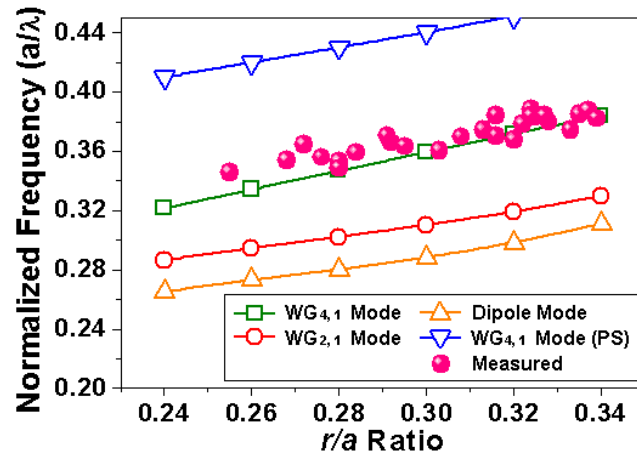
Fig. 3-6: Defect modes in normalized frequency of 8-fold QPhC D_1 nanocavity as a function of *r/a* ratio. The PS denotes the phase-shifting mode [61]. The solid spheres denote the measured data, which match with $WG_{4,1}$ mode quite well.

3-2-2   Side-Mode Reduction Mechanism

Due to the zero field distribution of $WG_{4,1}$ mode shown in Fig. 3-3(b), intuitively, one can add a central post or a central air hole beneath or inside the nanocavity region without disturbing the $WG_{4,1}$ mode, as the scheme shown in Fig. 3-7(a). In addition, the other side modes can also be reduced [62] or destroyed due to this disturbance. To understand these assumptions, we perform FDTD simulation of the 8-fold QPhC D_1 nanocavity with a central air hole. The ratio of central air hole radius (*r'*) over *a* (*r'/a* ratio) is 0.30. The well-confined

WG$_{4, 1}$ mode is still sustained in the nanocavity region as shown in Fig. 3-7(b). To further confirm above inference, we compare the lasing spectra from fabricated 8-fold QPhC D$_1$ nanocavities with and without the central air hole. Except the central air hole, the two devices are both with similar lattice parameters as shown in the SEM pictures in Fig. 3-8(a) and (b) insets. The measured lasing spectra in dB scale are shown in Fig. 3-8(a) and (b). One can see that the side mode is greatly reduced and the SMSR increases from 25 dB to larger than 30 dB after adding a central air hole, which agrees with our predictions. Besides, the WG$_{4, 1}$ mode is not affected significantly as predicted and the estimated Q factor is 7,000, which is only a little smaller than that without a central air hole. And this also indicates that the lasing mode is WG$_{4, 1}$ mode.
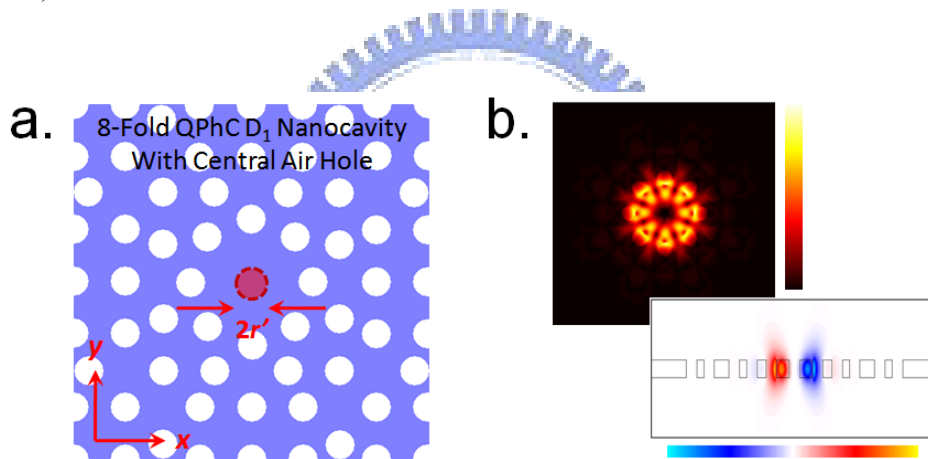
Fig. 3-7: (a) Scheme of an 8-fold QPhC D$_1$ nanocavity with central disturbance (air hole inside or nano-post beneath). (b) FDTD simulated WG$_{4, 1}$ mode profile in electrical field in *x-z* and *x-y* planes in 8-fold QPhC D$_1$ nanocavity.
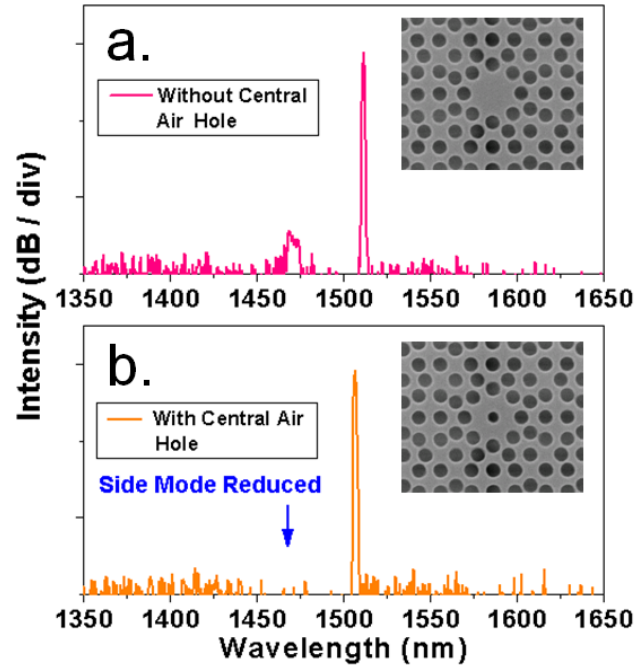
Fig. 3-8: Lasing spectra in dB scale of 8-fold QPhC D_1 nanocavities (a) without and (b) with a central air-hole. The side mode is greatly reduced by inserting the central air hole. The SEM pictures of measured devices are also shown in the insets. The inserted air hole radius is 0.24a.

From the view point of fabrication, the large central disturbance implies larger fabrication tolerance and less sensitivity of the $WG_{4,1}$ mode to the central disturbance, air hole or nano-post. In the former case, large air hole size would be benefit in serving as micro-biosensors for catching and detecting virus [23]. In the latter case, with large nano-post size, there would be lower threshold voltage and better heat dissipation when the central nano-post served as electrically-driven structure we will investigate in next chapter. As a result, we also investigate the threshold variation of $WG_{4,1}$ mode lasing from 8-fold QPhC D_1 nanocavities under different central air hole radius from 0.24a to 0.5a and the measurement results are shown in Fig. 3-9. Significant increase of threshold is observed when central air hole radius is larger than 0.32a, where $WG_{4,1}$ mode will be destroyed by the large central air hole.
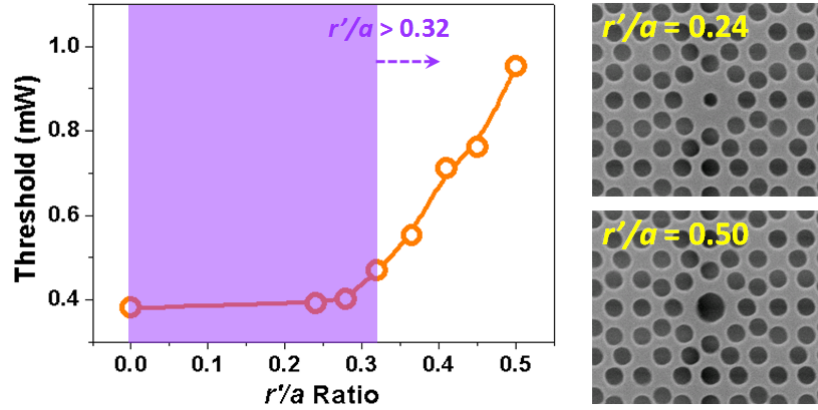
Fig. 3-9: Threshold variation of $WG_{4,1}$ mode lasing as a function of different central air hole sizes.

3-2-3 Compact Device Size

We also fabricate 8-fold QPhC D_1 nanocavity arrays with different cladding lattice periods from eight to three. The tilted-view SEM picture is shown in Fig. 3-4(b). The plot of lasing threshold versus number of cladding lattice periods is shown in Fig. 3-10. The threshold of 8-fold QPhC D_1 nanocavity with eight lattice periods is 0.71 mW and the lasing wavelength is 1454 nm. The higher threshold of this cavity than the one in Fig. 3-5 is caused by different gain spectrum alignment. In Fig. 3-10, the thresholds are almost the same when the number of lattice periods is larger than six. Although the threshold increases when the number of lattice periods is smaller than six, the threshold with four lattice periods is 0.95 mW, which is only 36 % increase compared to that with eight lattice periods. With four cladding lattice periods, the device size is only 3.5×3.5 μm^2 as shown in the inset SEM picture of Fig. 3-10, which is a very condensed device size and suitable for integrating in PICs without affecting or being affected by other integrated components. Lasing action is not always observed when the number of lattice periods is reduced to three. We also clarify that the lasing action under very condensed device size are attributed to both PBG effect from 8-fold QPhCs and TIR effect from air windows on top and bottom sides of the nanocavity as shown in SEM picture in Fig. 3-4 [63]. To confirm this inference, we simulate the Q factor of $WG_{4,1}$ mode in 8-fold QPhC
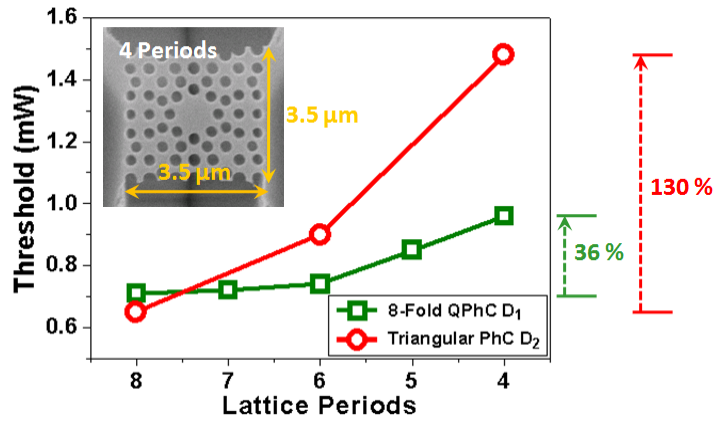
Fig. 3-10: Plot of $WG_{4, 1}$ mode lasing threshold versus number of cladding lattice periods. There is only 36 % increase in threshold of 8-fold QPhC D_1 nanocavity when the number of lattice periods is reduced from eight to four, which is much smaller than the 130 % of triangular lattice PC D_2 micro-cavity. The inset shows the SEM image of the 8-fold QPhC D_1 nanocavity with four lattice periods and very condensed size of 3.5×3.5 μm^2.

D_1 nanocavities with and without air windows under the same lattice period of four. The simulated Q factors of these two cases are 3,500 and 2,000, respectively. The simulated results agree with above inference.

We also fabricate triangular lattice PhC microcavity with similar cavity size formed by seven missing air holes (D_2 microcavity) for comparison. The fabricated r/a ratio and lattice constant are 0.29 and 480 nm. As shown in Fig. 3-10, the thresholds of triangular lattice PhC D_2 microcavities with eight, six, and four cladding lattice periods are 0.65 mW, 0.9 mW, and 1.48 mW, respectively. And the lasing wavelength is near 1560 nm, which aligns better with the gain peak of multi-quantum-wells (MQWs) better than 8-fold QPhC D_1 nanocavity in this experiment, and leading to a smaller threshold of triangular lattice PhC D_2 microcavity with eight lattice periods than that of 8-fold QPhC D_1 nanocavity. For the number of lattice periods below seven, one can see that the thresholds of 8-fold QPhC D_1 nanocavity are much lower than that of triangular lattice PC D_2 microcavity even the lasing wavelength of the former is much farther away from the gain peak of MQWs. In addition, the threshold of triangular lattice PhC D_2 microcavity increases about 130 % from eight periods to four periods, which is

much larger than the 36 % of 8-fold QPhC D_1 nanocavities.

In triangular lattice PhC D_2 microcavity, the lasing mode is similar to A_1 mode [51] instead of WG mode, which is due to the low Q factor (only several hundred or lower) of WG mode in it [64]. However, a high Q $WG_{4, 1}$ mode can be sustained in 8-fold QPhC D_1 nanocavity, and its performance is even better than the high Q mode in triangular lattice PhC D_2 microcavity. Nevertheless, actually, this PhC D_2 microcavity design can be further modified to enhance a high Q WG mode in it and we will mention this in Chapter 5.

3-3   Circular Photonic Crystal C_2 Microcavity
3-3-1   Circular Photonic Crystal and Its PBG Effect

In 2003, a microcavity design named annular circular resonator (ACR) is proposed by J. Scheue and A. Yariv [65, 66]. In ACR, the confinement of the circular microcavity is provided by Bragg reflection of the surrounded annular Bragg distributed reflectors (DBRs) formed by concentric periodic circular air trenches, which can be regarded as 1D PhC microcavity. Scheme of ACR is shown in Fig. 3-11(a). However, there are two problems in ACR due to the discontinuous annular Bragg reflector structure. First, the widely used membrane structure cannot be applied in ACR. Second, the current injection structure cannot be achieved. To solve this problem, one promising solution is replacing the air trenches by air holes, which is called circular-PhC (CPhC) lattice, as shown in Fig. 3-11(b). This kind of CPhC lattice could provide more uniform PBG confinement in different directions, which has been applied in microcavities [58, 67-69] and low-loss waveguide bends [69-71].

ACR with DBR Composed by Air Trenches   ACR with CPhC Composed by Air Holes
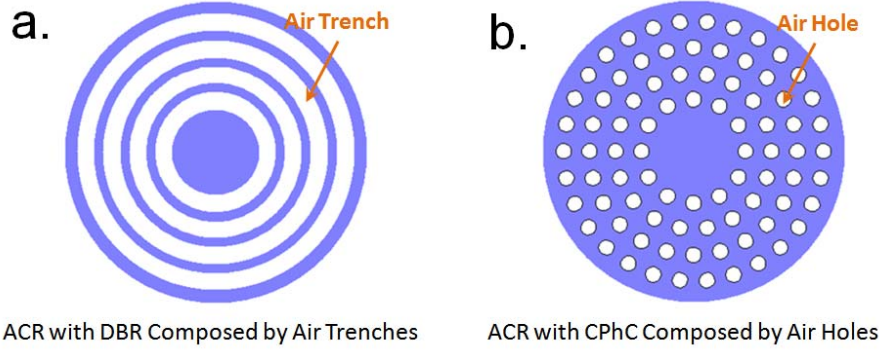
Fig. 3-11: Scheme of the ACR surrounded by (a) air trenches (DBRs) and (b) the CPhC lattice composed by the air holes.

In general, the CPhC lattices are arranged to be concentric circles in different formations including square, triangular, and sunflower type [68]. Scheme of a sunflower type CPhC lattice we investigate here is shown in Fig. 3-12, and the spatial lattice positions on the *x-z* plane are given by

$$x = aN\cos(\frac{2n\pi}{6N}), \quad z = aN\sin(\frac{2n\pi}{6N}), \quad n = 1 \sim 6N \qquad (3\text{-}1)$$

where *a* and *N* denote the lattice constant and number of the concentric lattice periods, which are also defined in Fig. 3-12. To investigate its PBG effect, we calculate its transmission spectrum by 3D FDTD method as we mentioned in Chapter 2-1. A Gaussian dipole source with 0.366 central normalized frequency is put on one side of the CPhC lattice formed by 127 air holes. Then, the transmitted electromagnetic wave is detected by a detector on the opposite side. The calculated transmission spectrum of CPhC with *a* = 500 nm and *r/a* ratio of 0.42 is shown in Fig. 3-13(a). In this figure, significant PBG region lower than -15 dB transmission for normalized frequency from 0.29 to 0.354 is observed.
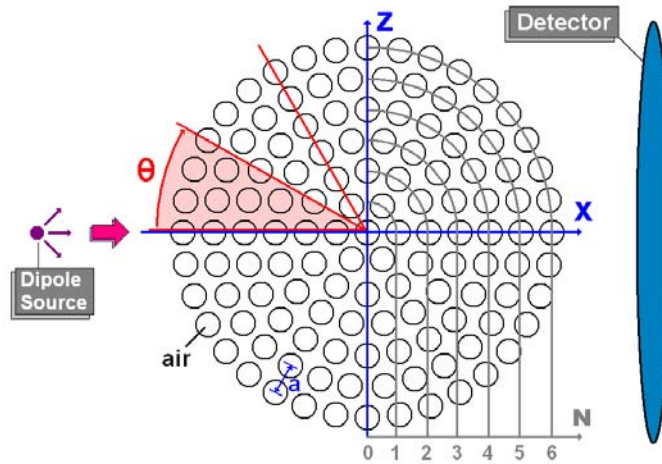
Fig. 3-12: Scheme of sunflower type CPhC lattice structure and the FDTD simulation setup of transmission spectrum.

To investigate the PBG isotropy, we rotate the CPhC lattice by an angle θ with 3° increment as shown in Fig. 3-12. In the simulation, we only deal with the case of $\theta = 0 - 30$° due to the 12-fold-like rotational symmetry of CPhC lattice. The normalized frequency of upper and lower gap boundaries as a function of θ is shown in Fig. 3-13(b). The variations of PBG width and upper and lower boundaries compared to the PBG width (defined at 0 degree) are only 6.7 %, 7.9 %, and 4.5 %, respectively, which shows the isotropic PBG of CPhC [72]. We also numerically study the PBG directional variation of triangular PhC for comparison by the same simulation setup. Its PBG width variation is found to be 10.1 %, which is larger than that of CPhC. Besides, the transmission depth variation of PhC PBG is about 15 dB, which is also much larger than 5 dB of CPhC PBG. Thus, above numerical results clearly indicate the isotopic PBG effect of CPhC. In chasing for threshold-less micro- and nano-laser sources, the reduction of unnecessary spontaneous emission by the PBG effect becomes a key issue. To suppress the spontaneous emission efficiently, the directional difference of PBG has to be relatively small compared to the width of PBG itself [73], that is, the PBG must be isotropic. As a result, the CPhC with isotropic PBG can be considered as a potential candidate of lattice structure to realize threshold-less laser sources.
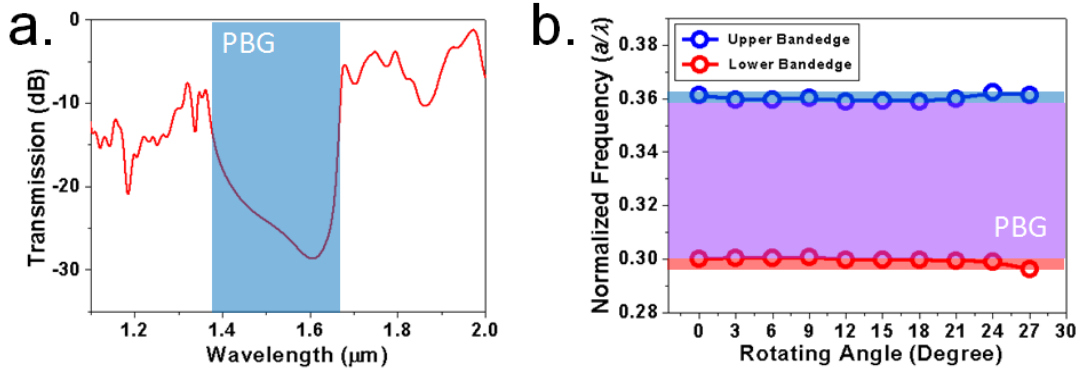
Fig. 3-13: (a) 3D FDTD simulated transmission spectra of CPhC lattice structure. The spectrum indicates the PBG region for normalized frequency from 0.29 to 0.354. (b) By rotating the whole CPhC lattice, the variations of PBG width and upper and lower gap boundaries are calculated, which are 6.7, 7.9, and 4.5 %, respectively, compared to PBG width at $\theta = 0$.

3-3-2　Microcavity Design & Modal Behavior

As a result, we design a microcavity formed by seven missing air holes, named CPhC C_2 microcavity, as shown in the scheme in Fig. 3-14. The simulated modal characteristics by 3D FDTD simulations indicate the WG mode can be well sustained in this microcavity. Some lattice parameters are also denoted in Fig. 3-14. The normalized frequencies of calculated defect modes versus r/a ratio of CPhC C_2 microcavity are shown in Fig. 3-15(a). Although lots defect modes exist within the PBG region, we only show WG modes in Fig. 3-15(a), including $WG_{5,1}$, $WG_{6,1}$, $WG_{7,1}$, and $WG_{6,1}$ PS modes. Their mode profiles in electrical fields and calculated Q factors are shown in Fig. 3-15(b). High Q factor of 30,000 is obtained from $WG_{6,1}$ mode. Thus, we will focus on this $WG_{6,1}$ mode in our following experiments and discussions.
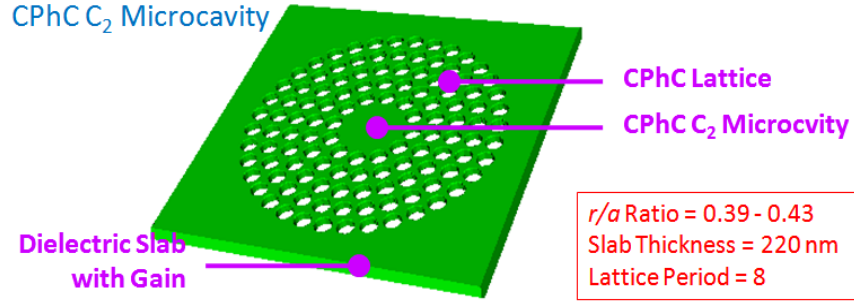
Fig. 3-14: Scheme and lattice parameters in simulations of CPhC C_2 microcavity.
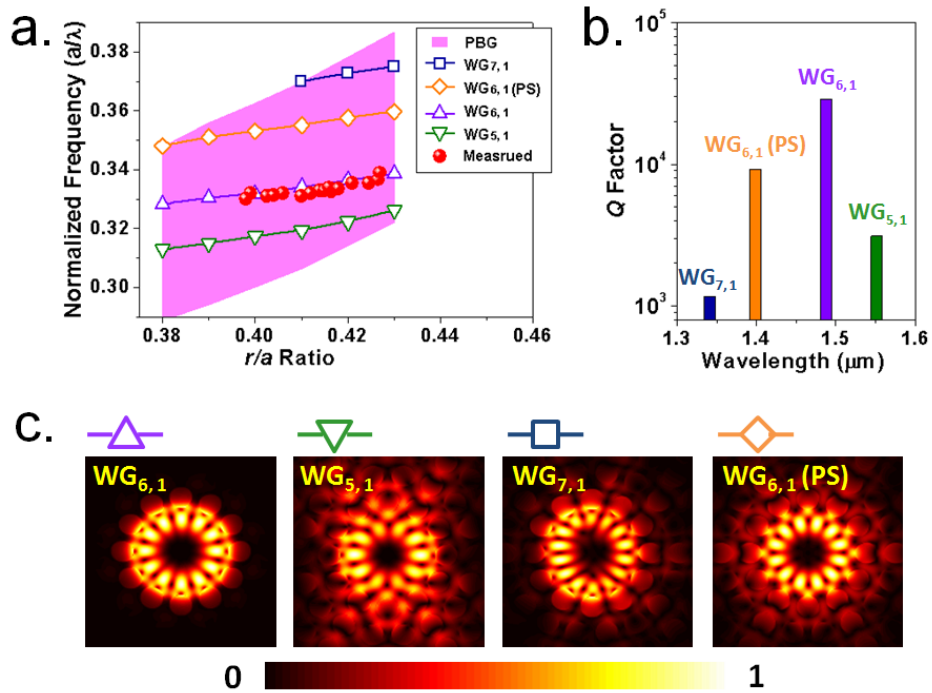
Fig. 3-15: (a) Simulated WG modes in normalized frequency with different r/a ratios of CPhC C_2 microcavity by 3D FDTD simulations. The measured results denoted by open circles indicate that the lasing mode is $WG_{6,1}$ mode. The FDTD simulated (b) Q factors and (c) mode profiles in electrical field of WG modes in CPhC C_2 microcavity.

According to our design, the CPhC C_2 microcavities with different lattice parameters are fabricated. Top- and tilted-view SEM pictures of CPhC C_2 microcavity array are shown in Fig. 3-16. In characterizations, the fabricated microcavities are optically pumped at room temperature by 845 nm laser pulse with 0.5 % duty cycle in the NIR micro-PL system. The measured lasing actions are denoted by the red spheres in Fig. 3-15(a) and they clearly indicate the lasing mode is $WG_{6,1}$ mode when comparing with the FDTD simulation results.

39

The small difference between simulated and measured results is arisen from the fabrication imperfections and the inaccuracy when estimating lattice parameters from SEM pictures. The typical *L-L* curve is shown in Fig. 3-17(a) and the threshold can be estimated as low as 0.13 mW from the curve. The spectra of near and above threshold at lasing wavelength 1520 nm are shown in Fig. 3-17(b) and (c). The line-width (Δ_{FWHM}) of 0.16 nm is obtained by Lorentzian fitting from the spectrum near the transparency pump level shown in Fig. 3-17(b). And the measured Q factor of 9,500 can be estimated from the formula of $Q = \lambda / \Delta_{FWHM}$.
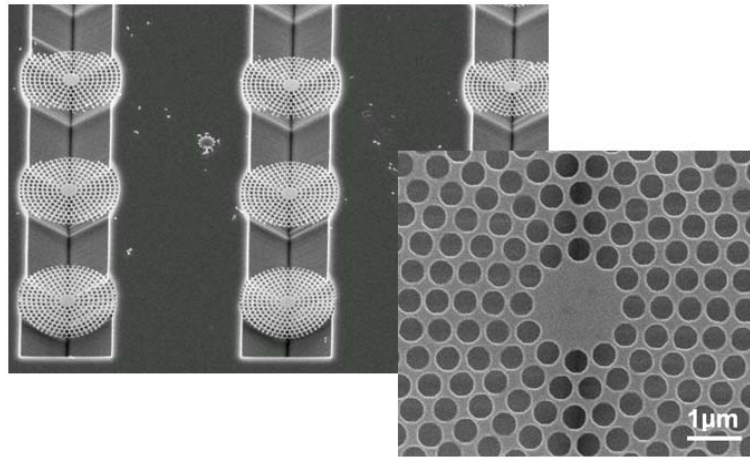
Fig. 3-16: Tilted-view SEM picture of CPhC C_2 microcavity array. Top-view image is also shown in the inset.
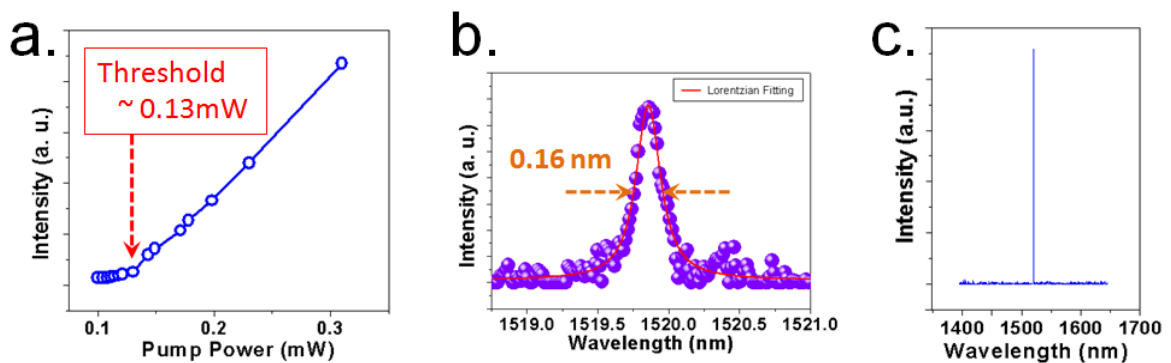
Fig. 3-17: (a) *L-L* curve and spectra of (b) near and (c) above threshold of $WG_{6,1}$ mode lasing action at 1520 nm for a typical CPhC C_2 microcavity. Its threshold and Q factor are estimated as 0.13 mW and 9,500 from the *L-L* curve and the spectrum near threshold.

3-4 Summary

In this chapter, we propose an 8-fold QPhC D_1 nanocavity design can well confine a $WG_{4,1}$ mode under proper cavity modification. The $WG_{4,1}$ single mode lasing action with low threshold of 0.35 mW and high Q factor of 7,500 are obtained from the well-fabricated devices and confirmed by FDTD simulations. A side mode reducing mechanism by inserting a central air hole in the nanocavity without affecting the $WG_{4,1}$ mode significantly is also proposed and investigated. The SMSR is improved from 25 dB to larger than 30 dB. In addition, the $WG_{4,1}$ single mode lasing is obtained under very compact device size of 3.5 × 3.5 μm^2 by reducing the QPhC periods.

Besides, we investigate a novel CPhC lattice structure with isotropic PBG effect in simulation, which is beneficial to achieve threshold-less laser source when served as the mirror of microcavity. Thus, a CPhC C_2 microcavity sustaining high Q $WG_{6,1}$ mode is design and demonstrated. $WG_{6,1}$ single mode lasing actions with low threshold of 0.13 mW and high Q factor of 9,500 are obtained.
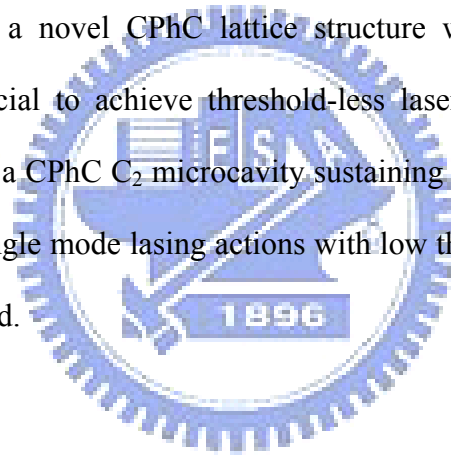
Chapter 4

Whispering-Gallery Mode in 12-Fold Quasi-Photonic Crystal Microcavity

In this chapter, we design a D_2 microcavity design based on 12-fold quasi-photonic crystal (QPhC), which sustains high quality (Q) factor whispering-gallery (WG) mode in it. The WG single mode lasing actions with high Q factor and low threshold are obtained in experiments. We also investigate and confirm the strong WG mode dependence on the cavity geometry both in experiments and simulations. Besides, we propose and demonstrate the WG mode coupling microcavities based on 12-fold QPhC D_2 microcavity.

And then we investigate the variations of optical and thermal properties of WG mode in 12-fold QPhC D_2 microcavity when different nano-posts are inserted beneath the microcavity both in simulations and experiments. The nano-post structure is potential in serving as an efficient current injection pathway. The lasing performance degradation and thermal properties improvements are confirmed by comparing experimental results with the simulated results.

4-1   12-Fold Quasi-Photonic Crystal D_2 Microcavity

In Chapter 3, we have used the 8-fold QPhC with high symmetry in designing QPhC nanocavity. Actually, the higher rotational symmetry level can be achieved by 12-fold QPhC lattice structure [56]. Scheme of 12-fold QPhC lattice structure is shown in Fig. 4-1(a). From the FDTD simulated transmission spectrum shown in Fig. 4-1(b), significant PBG effect can be observed from the two neighboring low transmission frequency ranges. It has been
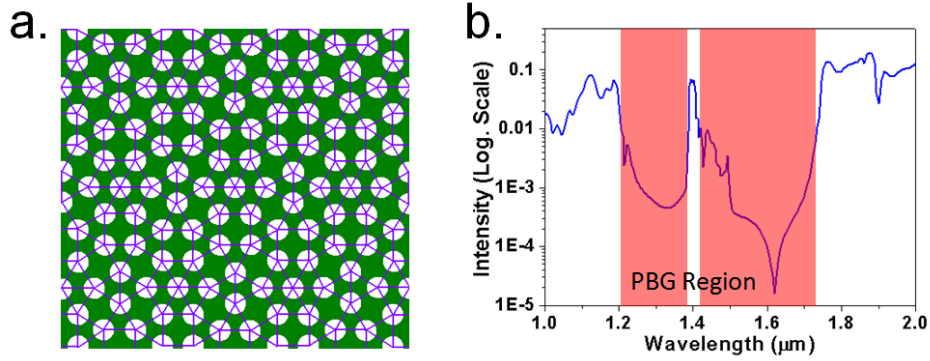
Fig. 4-1: (a) Lattice structure of 12-fold QPhCs. (b) 3D FDTD simulated transmission spectrum of 12-fold QPhC on a 220 nm dielectric slab. Two neighboring low-transmission region indicate the PBG region.

reported that the large, directionally uniform, and complete PBG effect can be found in 12-fold QPhCs theoretically and experimentally [56, 74]. This directional uniform PBG effect from 12-fold QPhCs is very beneficial for electromagnetic wave propagation and confinement, which has been reported and demonstrated by metallic periodic structures in waveguide [75, 76] and microcavity [77, 78] applications in microwave range.

4-1-1 Microcavity Design, Simulated, and Measured Modal Properties

Based on this 12-fold QPhC lattice structure, we design a microcavity formed by seven missing air holes (named D_2 microcavity). The microcavity design and structure are shown in Fig. 4-2. The QPhC patterns are defined by air holes on a thin dielectric slab with 220 nm thickness and refractive index of 3.4. At first, we calculate the resonance modes in this microcavity by 3D FDTD method. The relationship between hole radius (r) over lattice constant (a) (r/a) ratio and normalized frequencies of defect modes inside the PBG region is shown in Fig. 4-3(a). The mode profiles in magnetic field of each defect mode in microcavity are shown in the insets in Fig. 4-3(c). By evaluating energy decay curve, the Q factor of each defect mode in the microcavity is shown in Fig. 4-3(b). We obtain a relatively high Q factor of 38,000 from $WG_{6,1}$ mode, which indicates $WG_{6,1}$ mode will be the dominant mode. Besides,

43
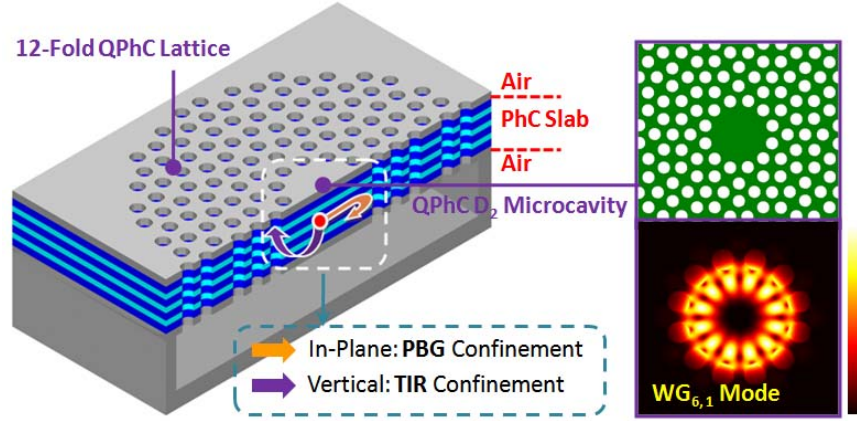
Fig. 4-2: Scheme of 12-fold QPhC D_2 microcavity. The right insets show the microcavity geometry and the sustained high Q $WG_{6,1}$ mode profile in electric field, respectively.
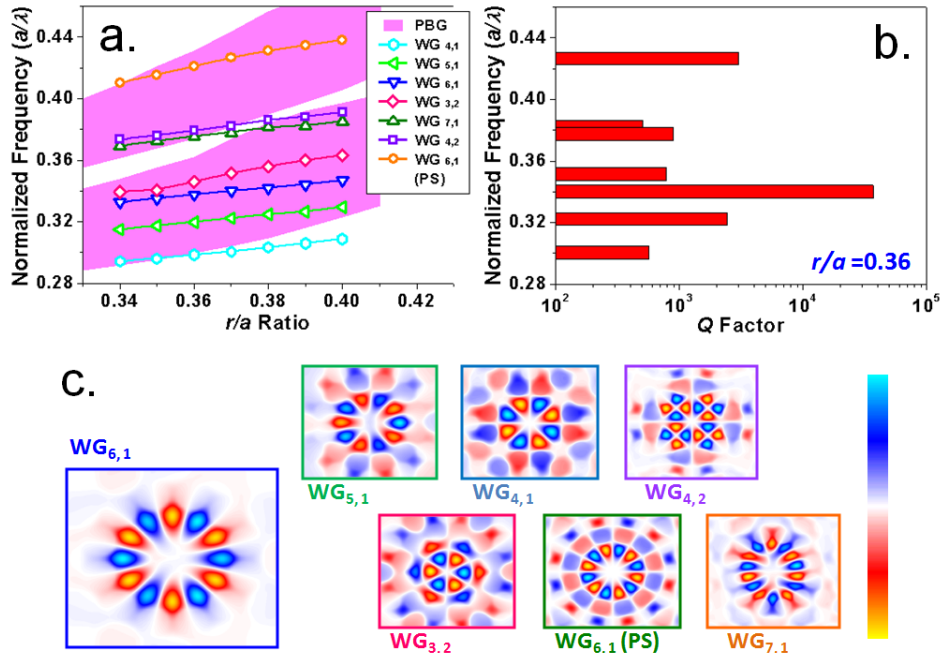
Fig. 4-3: (a) The plot of simulated defect mode frequency versus QPhC r/a ratio. (b) The FDTD simulated Q factor of each defect mode. The highest Q factor of 38,000 from $WG_{6,1}$ mode is obtained. (c) The FDTD simulated mode profiles in magnetic fields of each defect mode.

relative to the cavity volume (~ 0.70 μm^3), a small effective mode volume of 1.6 $(\lambda/n)^3$ (~ 0.16 μm^3) is also confirmed. The simulated $WG_{6,1}$ mode profile in electric field with significant central zero-field is also shown in the inset of Fig. 4-2.

According to this design, the 12-fold QPhC D_2 microcavities with different lattice

44

parameters are fabricated. Top- and tilted-view SEM pictures of fabricated device are shown in Fig. 4-4. By performing NIR micro-PL measurements at room temperature, the $WG_{6,1}$ single mode lasing is obtained and identified by comparing the measured results with the FDTD simulated results. The light-in light-out (L-L) curve and the spectrum of $WG_{6,1}$ single mode lasing are shown in Fig. 4-5(a) and (b), respectively. From the L-L curve, we obtain an ultra-low threshold of 0.15 mW. And from the spectrum near transparency, the spectral line width is estimated as 0.15 nm by Lorentzian fitting at 1572 nm, which corresponds to a high Q factor of 10,000. We also fabricate triangular lattice PhC D_2 microcavity laser by the same process and on the same wafer for comparisons. The Q factor of main lasing mode of PhC D_2 microcavity is only 3,000 - 4,000 [79]. The L-L curve and SEM picture of PhC D_2 microcavity are also shown in Fig. 4-5(a) and the inset. The threshold and transparency line width of PhC D_2 microcavity laser with single mode lasing at similar wavelength are 0.6 mW and 0.3 nm, respectively, which both indicate the better performance of 12-fold QPhC D_2 microcavity lasers resulted from the directionally uniform PBG confinement provided by 12-fold QPhC and the presence of high Q $WG_{6,1}$ mode. Besides, this threshold of 0.15 mW is also lower than the 0.35 mW from 8-fold QPhC D_1 nanocavity we presented in Chapter 3.
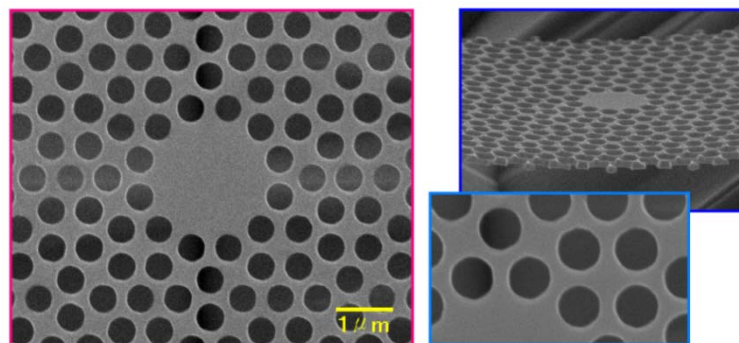
Fig. 4-4: Top- and tilted-view SEM pictures of fabricated 12-fold QPhC D_2 microcavity. The fabricated r/a ratio is 0.37.
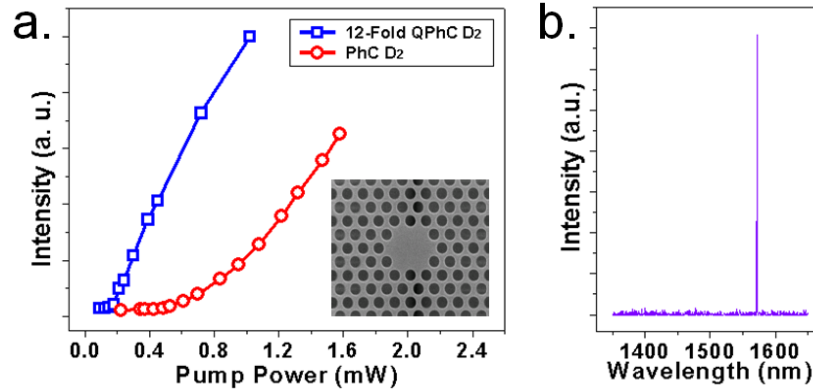
Fig. 4-5: (a) Typical *L-L* curves of 12-fold QPhC D_2 and triangular PhC D_2 microcavity lasers. Their thresholds are estimated as 0.15 mW and 0.6 mW at similar lasing wavelengths, respectively. (b) Typical lasing spectrum of 12-fold QPhC D_2 microcavity laser. The lasing wavelength is 1572 nm and the line width near transparency pump level is estimated as 0.15 nm by Loretzian fitting.

4-1-2 WG Mode Dependence on Cavity Geometry

In micro-disk lasers, it is well known that one can split or enhance specific WG mode by shaping the disk, for examples, square, stadium, elliptical, notched micro-disks [80], and micro-gear (micro-flower) lasers [60, 81]. In micro-gear lasers, the spacing of the gears formed at the edge of microdisk is designed to be half of WG mode lasing wavelength. And the specific WG mode with azimuthal lobes match with the gears will be well sustained and other resonance modes including π-phase shifting mode, WG modes with mismatched azimuthal lobes, and different order WG modes will be destroyed or weaken. In Fig. 4-2, the $WG_{6,1}$ mode profile has good consistency with the gears formed by the nearest air holes of the D_2 microcavity. This may imply the strong mode dependence of $WG_{6,1}$ mode on positions of the twelve nearest air holes.

To obtain more direct evidence for supporting this assumption, we randomly vary the positions of the twelve nearest air-holes (denoted by red circles, region-*A*) and the three outer layer air holes (denoted by blue circles, region-*B*) separately, as shown in Fig. 4-6(a).
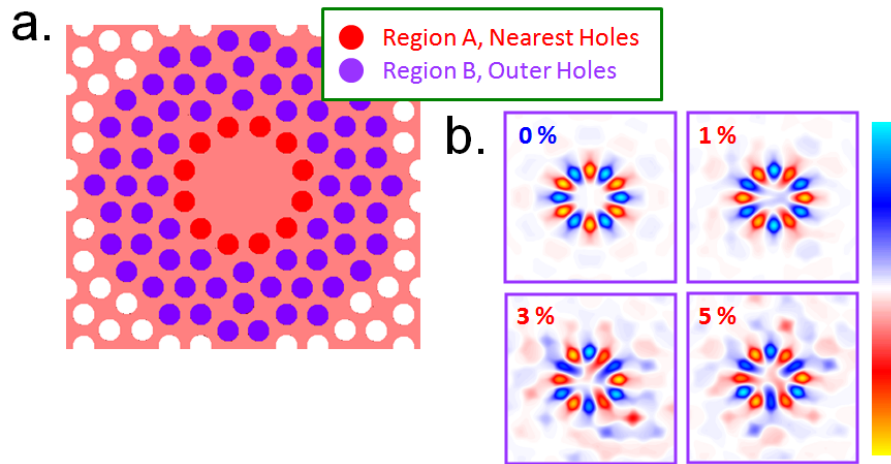
Fig. 4-6: (a) Scheme of two variation regions, the twelve nearest air-holes (denoted by red circles, region-*A*) and the outer air-holes (denoted by blue circles, region-*B*) in 12-fold QPhC D$_2$ microcavity. (b) The FDTD simulated WG$_{6,1}$ mode profiles in magnetic field of region-*A* case with lattice variation degree from 0 to 5 %. Significant mode distortions are observed when variation degree is larger than 3 %.

The degrees of variation are from *1 to 7 %* of lattice constant with fixed *r/a* ratio and lattice constant. In Fig. 4-6(b), we show the FDTD simulated WG$_{6,1}$ mode profiles in magnetic fields for the region-*A* case with the variation degree from 0 to 5 %. One can see significant mode distortion compared to the original mode profile also shown in Fig. 4-6(b). And the WG$_{6,1}$ mode wavelength is also varied significantly when randomly varying the region-*A* lattice in FDTD simulations. In contrast, there are no significant mode profile distortions and wavelength variation in region-*B* case. Thus, above simulated results indicate the strong mode dependency of WG$_{6,1}$ mode on the twelve nearest air holes.

In experiments, the lasing spectra of fabricated devices with randomly varying the air hole positions in region-*A* and -*B* are shown in Fig. 4-7(a) and (b), respectively. The wavelength fluctuations for the region-*A* and -*B* cases are 20 nm and 2.5 nm, respectively. In the region-*A* case, when the twelve nearest air-holes positions are randomly shifted, the original WG$_{6,1}$ mode tends to self-optimize its resonance behavior according to this fluctuation and the constructive interference condition provided by the nearest air-holes is degraded. However, in
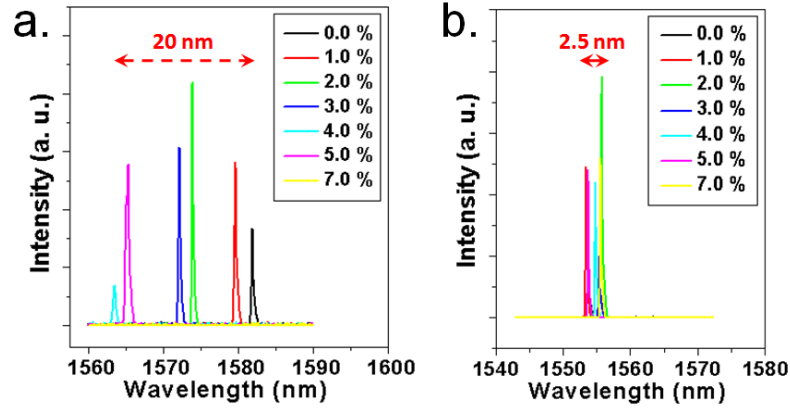
Fig. 4-7: Measured lasing spectra of devices with different variation degrees from 0 to 7 % in (a) region-*A* and (b) -*B*. Lasing wavelength variations for the region-*A* and -*B* cases are 20 nm and 2.5 nm.

the region-*B* case, it can be treated as the cavity boundary condition (positions of twelve nearest air-holes) is invariant, leads to almost the same lasing wavelength and threshold. The small wavelength variation 2.5 nm in the region-*B* case is caused by very slight hole-radius fluctuations occurred during the electron beam lithography process. Besides, the PBG position and width shifts caused by the lattice fluctuation can be neglected due to the relatively large band-gap of 12-fold QPhCs [59].

The statistical measurement results of these two cases are summarized in Table 4-1. The number of sampling devices is over 300. For the region-*A* case, lasing actions are not always observed with lattice variation degree 5 %. When the lattice variation degree increases up to 7 %, only 40 % of devices exhibit lasing actions with much higher thresholds (typically, larger than 0.8 mW) than those without lattice variation. However, for the region-*B* case, we still observe lasing actions for 90 % of devices with invariant thresholds when the variation increases up to 7%. These statistical results, once again, directly indicate the strong mode dependence of $WG_{6,1}$ mode on the twelve nearest air holes, that is, the microcavity geometry. This $WG_{6,1}$ mode dependence on microcavity geometry will be an important basis to enhance WG mode in other PhC-based microcavities that we will investigate in next chapter.

Table 4-1: Observed lasing actions of 12-fold QPhC D_2 microcavity lasers with different variation regions and degrees. Over 300 devices are measured.

Variation	0 %	1-4 %	5 %	7%
Region-A	100 %	100 %	70 %	40 %
Region-B	100 %	100 %	100 %	90 %

4-1-3 Coupling Microcavity Devices

Optical coupling microcavity or "Photonic molecules" (PMs) have long been regarded as good candidates for components with logical functions in PICs due to their special light-matter interactions, which can be analog to electronic states in chemical molecules and achieved by micro-spheres [82], micro-cylinders [83], micro-disks [84], and so on. The simplest and most widely-investigated PM is consisted of two identical semiconductor micro-disks sustaining high Q WG modes, which exhibits unique behaviors including optical filtering, switching, bi-stability [85, 86], and so on. Furthermore, this kind of PMs can be extended to a series of coupling microcavities, that is, the well-know coupling resonance optical waveguides (CROWs) [87, 88] for slow-light or optical buffer purposes in PICs. Recently, by using PhC micro- and nano-cavities, several PMs and CROWs designs have also been proposed and reported [89-92] for purposes of slow-light or optical bi-stability.

Due to the lattice structure of 12-fold QPhCs, at first, we design a twin microcavity composed by two neighboring D_2 microcavities, as shown in Fig. 4-8(a). From the FDTD simulations, the confined bonding (denoted as B-mode) and anti-bonding (denoted as A-mode) modes based on WG mode are confirmed. The mode profiles in magnetic fields are shown in Fig. 4-8(b), where the neighboring magnetic fields (mode lobes) are with opposite and positive signs in anti-bonding and bonding mode, respectively. It is worthy to note that the phase-shifted states in microdisk PMs [84] will be eliminated in this QPhC design due to the
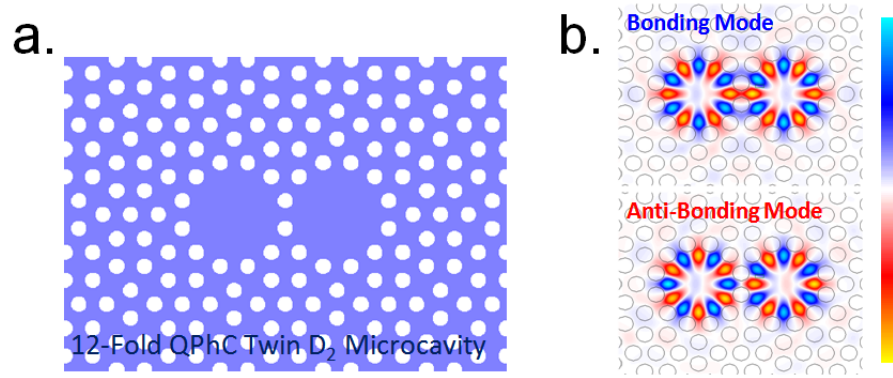
Fig. 4-8: (a) Scheme of 12-fold QPhC twin D_2 microcavity and (b) the FDTD simulated bonding (*B*-) and anti-bonding (*A*-) mode profiles in magnetic fields in it.
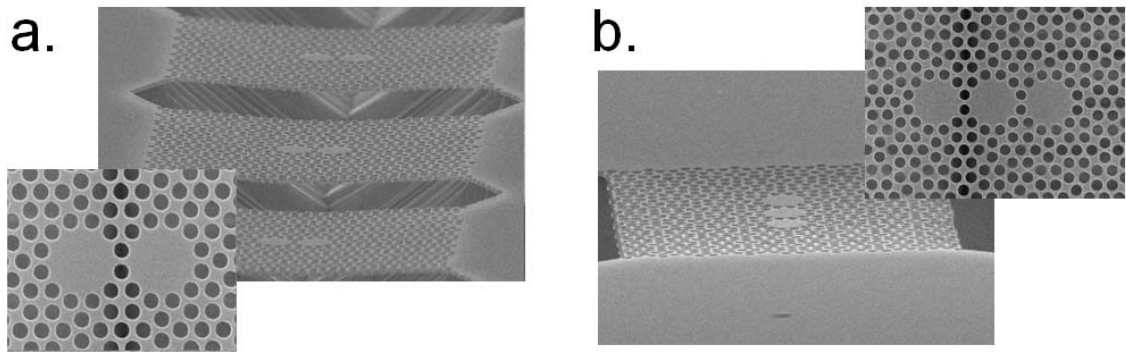
Fig. 4-9: SEM pictures of fabricated 12-fold QPhC (a) twin and (b) triple D_2 microcavities.
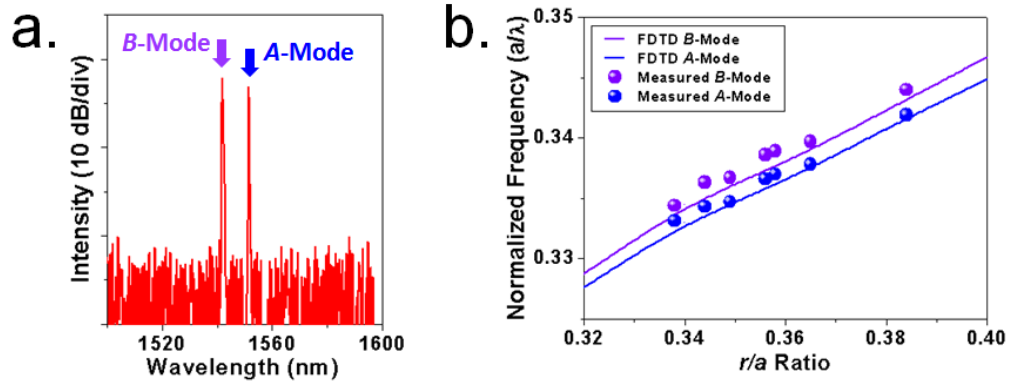
Fig. 4-10: (a) Lasing spectrum of bonding and anti-bonding modes. (b) The plot of simulated bonding and anti-bonding modes frequency versus QPhC *r/a* ratio. The purple and blue solid spheres denote the measured bonding and anti-bonding modes, respectively, which match with the simulated results quite well.
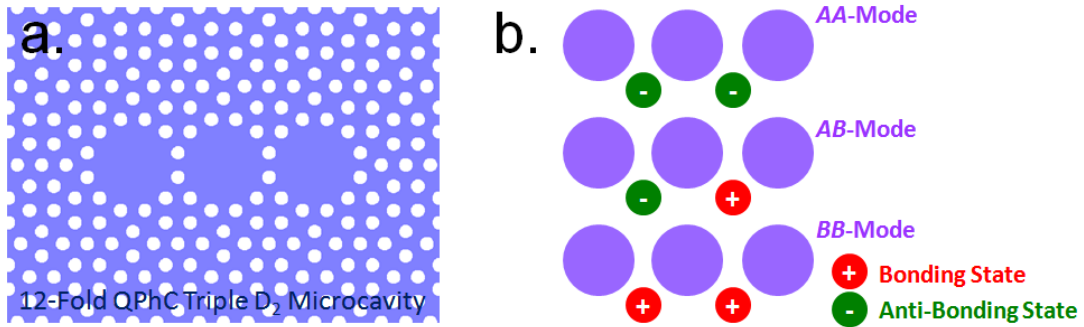
Fig. 4-11: (a) Scheme of 12-fold QPhC triple D_2 microcavity and (b) the PM mode catalog in it.

microgear effect. From the well fabricated devices shown in Fig. 4-9(a), we obtain bonding and anti-bonding modes lasing as shown in Fig. 4-10(a).

And then we further promote this twin microcavity design to be triple microcavity design shown in Fig. 4-11(a). According to the PM state of neighboring microcavities, the sustained PM mode can be classified into *AA*, *AB*, and *BB* modes, as shown in Fig. 4-11(b), where *A* and *B* represents anti-bonding and bonding state, respectively. The SEM picture of the fabricated 12-fold QPhC triple D_2 microcavity is shown in Fig. 4-9(b). In measurements, we also obtain three lasing modes shown in Fig. 4-12(a) correspond to *AA*, *AB*, and *BB* modes, respectively, which are identified by comparing the statistic measurement results with the simulated results shown in Fig. 4-12(b). This triple coupling microcavity design can be further extended to be a multi-microcavity design to form a CROW device as shown in Fig. 4-13.
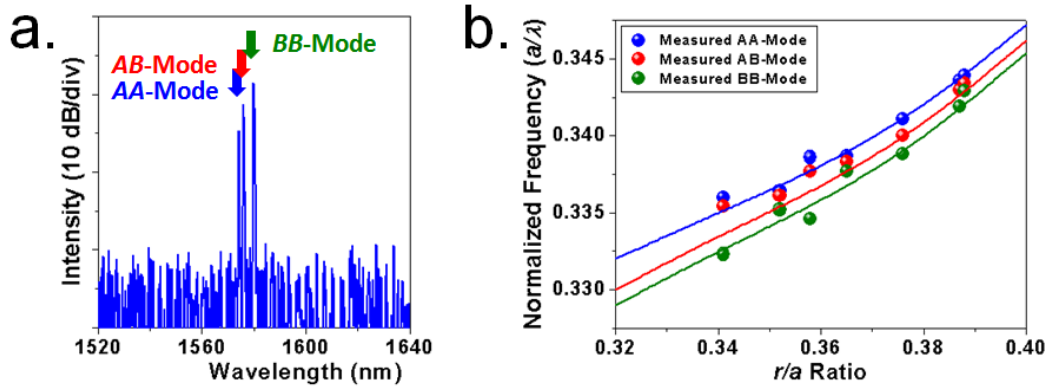
Fig. 4-12: (a) Lasing spectrum of *AA*-, *AB*-, and *BB*-modes. (b) The plot of simulated *AA*-, *AB*-, and *BB*-modes frequency versus QPhC *r/a* ratio. The solid spheres denote the measured results, which match with the simulated results quite well.
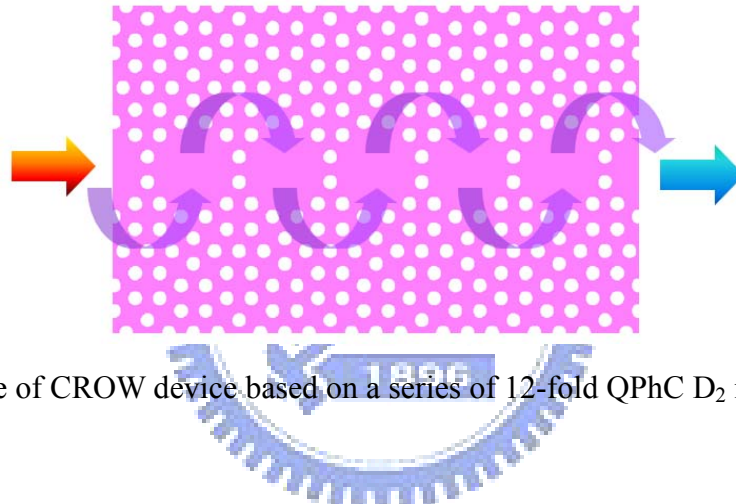
Fig. 4-13: Scheme of CROW device based on a series of 12-fold QPhC D_2 microcavities.

4-2   Nano-Post Structure in 12-Fold Quasi-Photonic Crystal D_2 Microcavity

Since the first demonstration in 1999 [8], various PhC micro- and nano-cavities with excellent properties and functionalities have been proposed and demonstrated as we mentioned before. However, most of them are still operated by optical excitation. To promote PhC microcavity lasers into industrial applications, the electrically-driven structure is necessary. Typically, most present PhC microcavities are constructed based on a suspended slab in air to obtain good optical confinement in vertical direction, which leads to high *Q* factors. However, to build a pathway for highly efficient current injection on such suspended
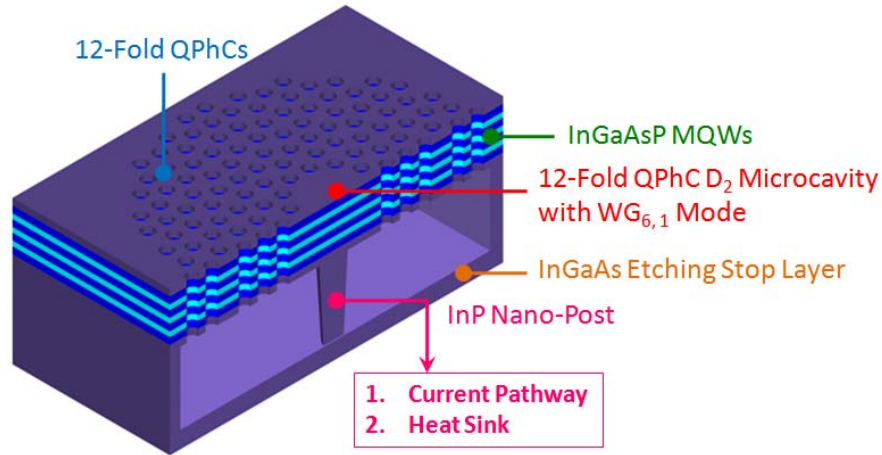
Fig. 4-14: Scheme of 12-fold QPhC D_2 microcavity with a nano-post beneath. This nano-post can be served as the current injection pathway and heat sinker at the same time.

structure has long been an arduous task. Actually, this goal can be achieved by inserting a central nano-post as a current pathway beneath the PhC microcavities [93, 94], which is similar to the approach in electrically-driven microdisk lasers [36]. In addition to the current pathway, the nano-post can also play the role of heat sink for the microcavity, which could be expected to provide the possibility of continuous-wave (CW) operation due to the improved heat dissipation. But this point has not been addressed and investigated in experiments yet.

As a result, in this section, we insert a nano-post beneath the 12-fold QPhC D_2 microcavity, as shown in Fig. 4-14. Under different nano-post sizes, we will investigate the influences on WG modal and thermal properties induced by different nano-post sizes both in experiments and simulations.

4-2-1　Influences on Optical and Thermal Properties by Nano-Post

At first, we investigate the influence on the $WG_{6,1}$ modal behavior caused by the inserted central nano-post with different post sizes beneath 12-fold D_2 microcavity. From 3D FDTD simulations, the plot of simulated Q factor and wavelength of $WG_{6,1}$ mode versus nano-post size in diameter is shown in Fig. 4-15(a). In the beginning, the Q value shows very little

variation with the increased nano-post size. However, when the nano-post size is larger than 1.6*a* in diameter, the *Q* factor degrades dramatically. To further understand this phenomenon, the electrical field distributions in *x-y* plane are shown in the inset of Fig. 4-15(a). There is no significant leaky energy flow through the post observed when the post size is 0.8*a* in diameter. However, when the post size increases to 2.4*a* in diameter, the WG mode is destroyed by the significant leaky energy flow through the nano-post, which corresponds for the degradation of *Q* factor. Also, from the Fourier-transformed electrical fields in *x-z* plane shown in Fig. 4-15(b), we can observe the significant extra leaky components inside the light cone (black circle) induced by the larger nano-post size of 2.4*a* in diameter when compared with that of 0.8*a* in diameter. Nevertheless, from the simulated results, we can still conclude that there would be only very1.6*a* in diameter.

On the other hand, the nano-post is expected for serving as an efficient heat sink. To further confirm this, we simulate the thermal behaviors of 12-fold QPhC D_2 microcavity with slight influences on the $WG_{6,1}$ mode lasing performance when the post size is smaller than and without the nano-post beneath by finite-element method (FEM). The simulation setup
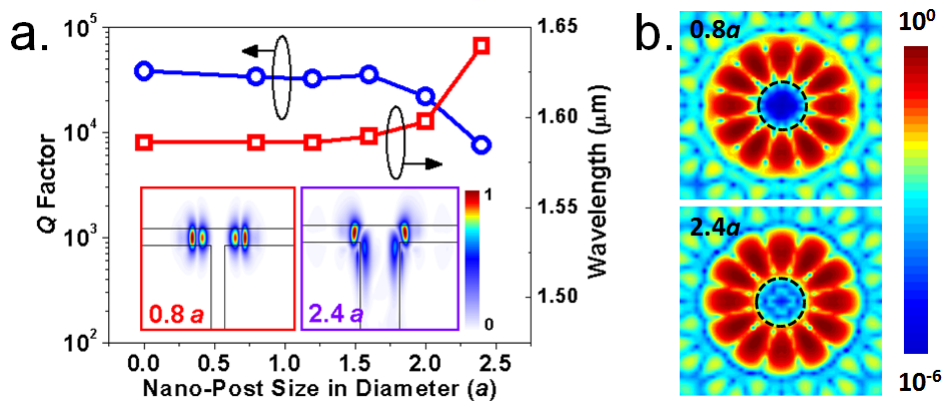
Fig. 4-15: (a) The relationship between the nano-post diameter and *Q* factor and wavelength of $WG_{6,1}$ mode. The *Q* factor dramatically degrades when the nano-post size is larger than 1.6*a* in diameter. The insets indicate the energy flows in *x-y* plane. (b) Fourier-transformed electric fields in *x-z* plane when the nano-post sizes are 0.8*a* and 2.4*a*, which show the extra leaky components induced by larger nano-post.

and scheme of 12-fold QPhC D$_2$ microcavity slab formed by Air / InGaAsP / Air is illustrated in Fig. 4-16(a). The QPhC lattice constant, *r/a* ratio, and slab thickness are set to be 550 nm, 0.38, and 220 nm, respectively. To accelerate our simulation, we reduce the simulation domain to be one-sixth of the whole structure due to the lattice symmetry feature. The initial temperature of the simulation domain is 300 K and the boundaries are set to be axial symmetric [95]. Besides, during the simulations, we also find that the contributions of heat radiation and convection are relative low compared with that of heat conduction, that is, the conduction dominates the heat transfer behavior [96]. The conductive heat transfer model is given by:

$$\rho \times C \frac{\partial T}{\partial t} + \nabla \cdot (-k \nabla T) = H \quad\quad\quad (5\text{-}1)$$

where ρ, k, and C represent the density, thermal conductivity, and thermal capacity of material, respectively. The H denotes a time- and position-dependent surface heat source we give in the simulation, which is an exponential decay form related to the absorption coefficient α (~ 3.5×10^6) of InGaAsP material. Referred to our measurement conditions, the pulse width, duty cycle, energy level, and pump area of H are set to be 25 ns, 0.5 %, 2 mW, and 1 μm in radius, respectively. Coefficients for different materials used in the simulation are listed in Table. 4-2. The simulated temperature distribution of 12-fold QPhC D$_2$ microcavity without nano-post is shown in Fig. 4-16(b). The highest temperature occurs at the cavity region with a 12.3 K increase above room temperature (300 K), which is a reasonable value under optical pulse excitation. On the other hand, the simulated temperature distributions of 12-fold QPhC D$_2$ microcavity with nano-post sizes of 440, 660, and 880 nm in diameter are also shown in Fig. 4-16(b) and the highest temperatures are 310.2, 308.9, and 307.7 K, respectively.

In addition, we also calculate the temperature decay time at the region where WG$_{6,1}$ mode most concentrates by first order exponential fitting from the transient solutions. The decay

time is defined as the time duration for the temperature drop to *1/e* of its highest value. The results obtained are 53.8, 42.0, 37.0, and 31.5 ns, respectively, which show the fast heat dissipation due to the presence of large nano-post. To further understand the heat conduction behavior, the temperature distribution of microcavity with 880 nm nano-post at different times of 30, 50, 120, and 200 ns are shown in Fig. 4-16(c). In Fig. 4-16(c), the heat flow is mainly
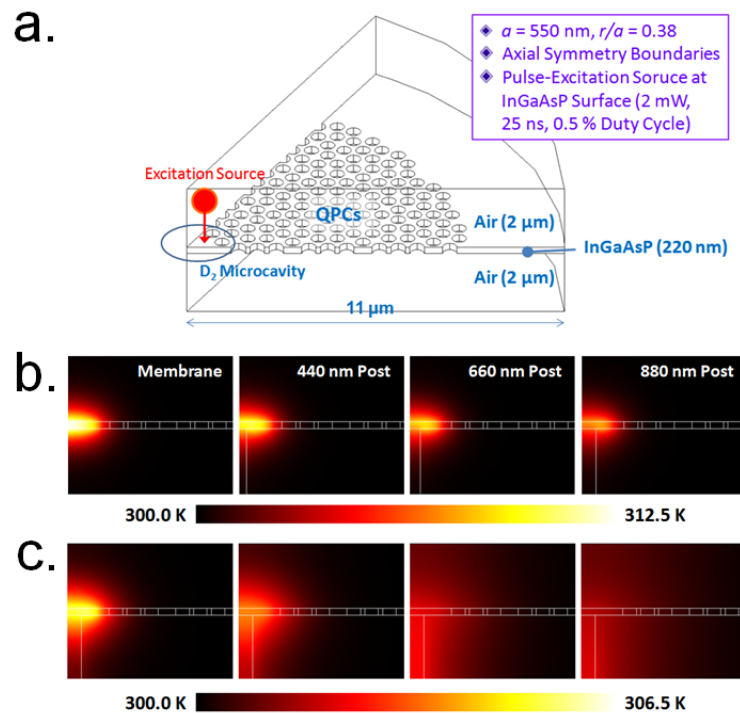
Fig. 4-16: (a) The scheme of the 12-fold QPC D_2 microcavity in FEM simulation. (b) The simulated temperature distributions of microcavities without and with nano-post sizes of 440, 660, and 880 nm in diameter. The temperature decreases when nano-post size increases. (c) The simulated temperature distributions of microcavity with nano-post size of 880 nm in diameter when the time is 30, 50, 120, and 200 ns.

Table. 4-2: Coefficients for different materials used in heat transfer simulation (in M.K.S. unit).

Material	ρ (kg/m^3)	C (J/kg.K)	k (W/m.K)
Air	1.205	1006	0.025
InP	4810	310	68
InGaAsP	5445.2	282.3	39.9

through the nano-post from $t = 30$ to 200 ns, which is a direct evidence of thermal improvement due to presence of the nano-post.

From above simulated results, comparing microcavity without nano-post beneath, although we can conclude that the better heat dissipation can be obtained by inserting large nano-post beneath the microcavity, the tolerable nano-post size is still limited to $1.6a$ in diameter when considering Q factor degradation we simulated previously.

4-2-2   Nano-Post Fabrication

To form different nano-post beneath the 12-fold QPhC D_2 microcavity, the wet-etching step in standard fabrication process has to be well controlled. The temprature of diluted HCl solution is fixed at 2 °C to slow down the InP etching rate, which is estimated to be 1.05 μm per minute along $<-1, 0, 0>$ direction of InP. Top-, tilted-, and cross sectional-view SEM pictures of fabricated 12-fold QPhC D_2 microcavity with a central nano-post beneath are shown in Fig. 4-17. In Fig. 4-17, the fabricated nano-post can be identified from the white shadow due to the electron accumlation in the top-view SEM picture or directly observed from the tilted-view SEM pictures. And we define the effective nano-post size D as twice the distance from microcavity center to the outermost position occupied by the nano-post instead
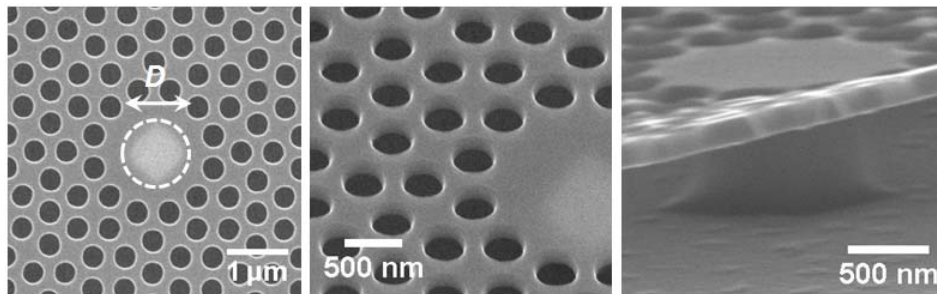
Fig. 4-17: Top-, tilted-, and cross sectional-view SEM pictures of fabricated 12-fold QPhC D_2 microcavity with central nano-post beneath are shown from left to right. The nano-post beneath the microcavity can be easily identified and observed. The fabricated r/a ratio is 0.34. (Courtesy of Wei-De Ho, Department of Photonics, National Chiao Tung University)

of the real size of nano-post, as shown in the left-most figure of Fig. 4-17. This is for the purpose of fairly estimating the influence on WG mode induced by the nano-post. Besides, by fine-tuning the wet etching time and air hole radius seperately, we can control and obtain central nano-posts with different nano-post sizes from 1.4 μm to 200 nm in diameter.

4-2-3   Measurements of Modal and Thermal Properties

In measurements, the fabricated 12-fold QPhC D_2 microcavity without and with nano-post sizes D = 200, 420, 900, and 1300 nm are used for characterizations. Under optical pulsed-pumping at room temperature, we obtain lasing actions from above devices. The measured L-L curves, lasing spectra above and near thresholds of microcavity without and with nano-posts D = 420 and 900 nm are shown in Fig. 4-18, Fig. 4-19(a) and (b), respectively. Comparing the lasing properties of microcavities without nano-post and with nano-post D = 420 nm ($\sim$ 0.8 a), their thresholds are both estimated as 0.35 mW from L-L curves in Fig. 4-18 and the measured Q factor slightly degrades from 10,000 to 8,000 as shown in Fig. 4-19(b). Besides, we also obtain $WG_{6,1}$ mode lasing action from the microcavity with small nano-post D = 200 nm ($\sim$ 0.4 a) and with $Q \sim$ 9,500, which is almost the same as that of the microcavity without nano-post. On the other hand, when D increases to 900 nm ($\sim$ 1.7 a), the threshold increases to 1.2 mW and the Q factor degrades to 5,800. Finally, when D further increases to be larger than 900 nm, the $WG_{6,1}$ single mode lasing is not observed anymore. The measured lasing performance degradation quite agrees with the trend of our simulated results presented in Fig. 4-15. It is also worthy to note that when the nano-post size comes close to the cavity size, in our case, 1.2 to 1.4 μm in diameter, the microcavity becomes an asymmetric structure. In this case, we observe the lasing mode hopping form $WG_{6,1}$ mode to the $WG_{3,2}$ mode at
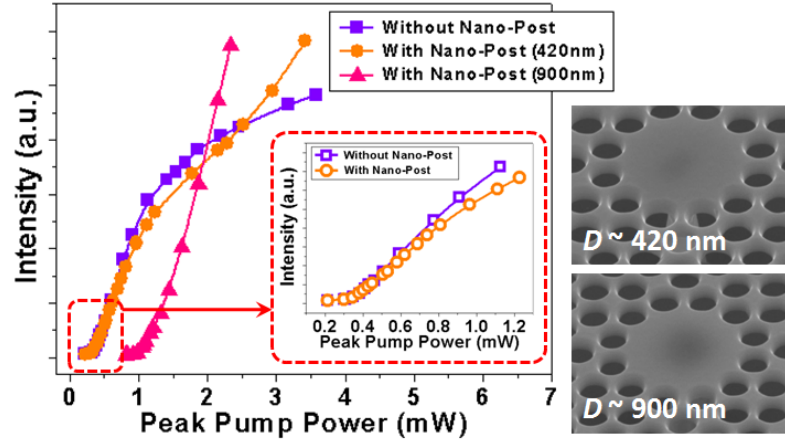
Fig. 4-18: *L-L* curves of 12-fold QPC D_2 microcavities without and with nano-posts when D = 420 and 900 nm. The thresholds are estimated to be 0.35, 0.35, and 1.2 mW, respectively. Tilted-view SEM pictures of microcavities with nano-post D = 420 and 900 nm are also shown.
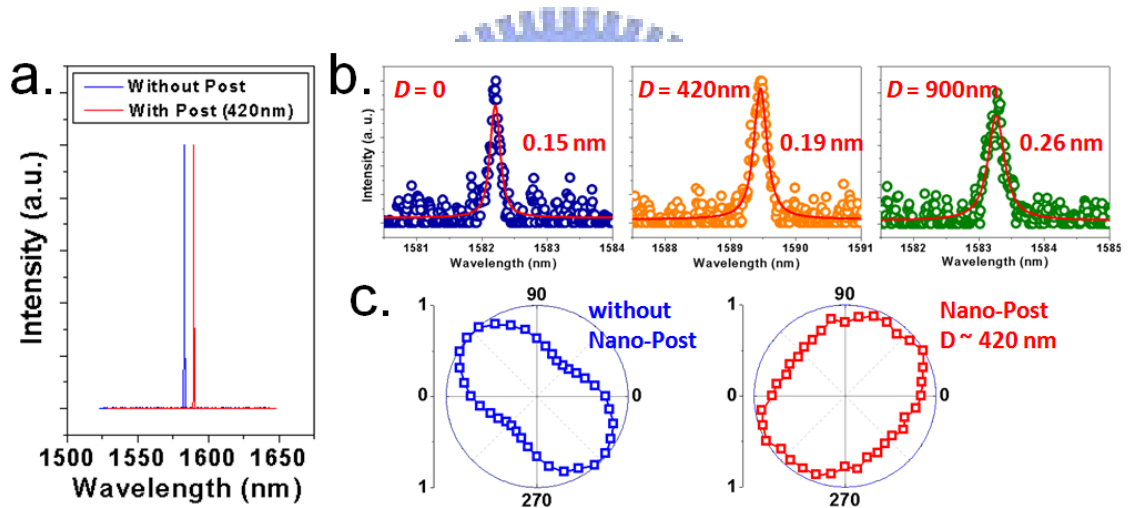
Fig. 4-19: (a) Lasing spectra above thresholds of mmicrocavity without and with nano-post D =420 nm. (b) Spectra below (~ 0.8 times) thresholds of microcavity with different nano-posts. The measured Q factor decreases from 10,000 to 5,800 when D increases from 0 to 900 nm. (c) The angular plots show the measured $WG_{6,1}$ mode polarizations before (left) and after (right) inserting the nano-post with low polarized ratios of 2.2 and 1.5.

Table. 4-3: Lasing properties of 12-fold QPhC D_2 microcavity with different nano-post sizes.

Nanopost Size (nm)	Q Factor	Threshold (mW)	Mode
0	10,000	0.35	$WG_{6,1}$
200	9,500	0.35	$WG_{6,1}$
420	8,000	0.35	$WG_{6,1}$
900	5,800	1.20	$WG_{6,1}$
1300	3,200	3.20	$WG_{3,2}$

shorter wavelengths with increased thresholds of 3.2 to 5 mW and degraded measured Q factors of 2,500 to 3,000. The measured lasing properties of 12-fold QPhC D_2 microcavity with different nano-post sizes are summarized in Table. 4-3.

In Fig. 4-19(c), the measured $WG_{6,1}$ mode polarizations show low polarized ratios (defined as maximum over minimum collected power) of 2.2 and 1.5 before and after inserting the nano-post. Although the polarized direction is changed after inserting the nano-post, the little variation in polarized ratio still indicates slight influence on $WG_{6,1}$ mode caused by the inserted nano-post. Besides, these low polarized ratios also indicate the uniformity of our fabrication process due to the low symmetry breaking [94, 97]. In fact, the ideal WG mode in the photonic crystal microcavity is un-polarized (i.e. polarized ratio is equal to 1) due to its well balanced inner symmetry of the mode and the cavity boundary (nearest air holes). However, in real case, this symmetry can be easily destroyed by perturbations, mainly from fabrication imperfections of nearest air holes. Thus, the WG mode will become polarized and the polarization degree (polarized ratio) will increase with the perturbations. Thus, small polarization degree indicates less fabrication imperfection and better uniformity of fabricated air holes of the sample.

It is also worthy to mention that the observed rolling-off phenomenon under increased pump power level with different nano-post sizes. From the *L-L* curves in Fig. 4-18, the fast rolling-off due to poor heat dissipation of the membrane structure is observed. And it is significantly improved when inserting the nano-post with $D = 420$ nm. Furthermore, when D

increases to 900 nm, the rolling-off effect disappears under the similar pump level and indicates the improvement of heat dissipation as we predicted by FEM simulations. To obtain more evidences about this improvement, thermal characterizations are performed and analyzed in the following.

In the thermal measurements, to observe significant heat dissipation improvement, the 12-fold QPhC D_2 microcavity with nano-post size equal to the limitation of 1.6a (~ 830 nm) we conclude previously is used. At first, we change the substrate temperature of the microcavity by a temperature controlling system we mentioned in Chapter 2-3-2. WG$_{6, 1}$ single-mode lasing action can still be obtained when the substrate temperature is as high as 70 °C, which is higher than the temperature limitation of 52 °C from 12-fold QPhC D_2 microcavity without nano-post. This observed lasing action at high substrate temperature of 70 °C is also better than those in PhC membrane microcavities with larger and similar microcavity sizes [95, 98], which can be attributed to the extra heat sink provided by the nano-post beneath. The measured *L-L* curves of WG$_{6, 1}$ mode lasing when the substrate temperature is varied from 20 to 70 °C are shown in Fig. 4-20(a). The threshold increases exponetially with the increased substrate temperature. This is reasonable because there would
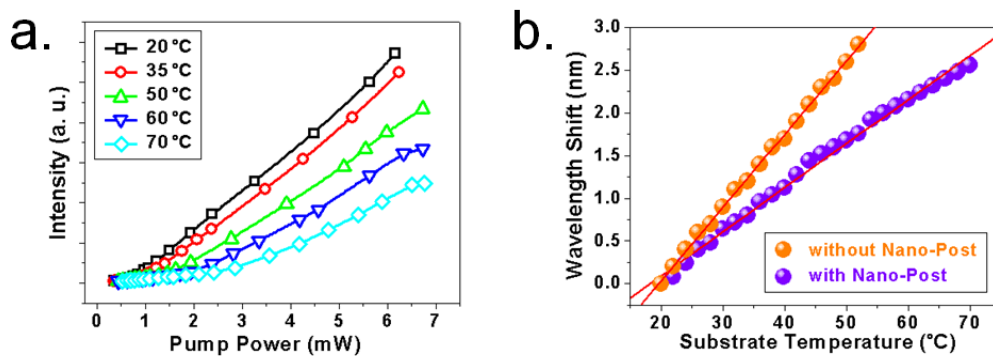
Fig. 4-20: (a) *L-L* curves of microcavity with nano-post size D = 830 nm under substrate temperatures of 20, 35, 50, 60, and 70 °C, respectively. (b) The lasing wavelength variation plot when the substrate temperature is varied from 20 to 70 °C. The red-shift rate is about 0.050 nm / °C, which is smaller than that (0.086 nm / °C) of microcavity without nano-post beneath.

be extra injected carrier wasting in non-radiative surface recombination, which leads to the increase of threshold when the substrate temperature increases. In addition, from Fig. 4-20(a), the decrease of slope efficiency monotonically with increasing substrate temperature also supports above inference.

We also observe the lasing wavelength red-shift when the substrate temperature increases from 20 to 70 °C with 2 °C increment, as shown in Fig. 4-20(b). In Fig. 4-20(b), we obtain total lasing wavelength red-shift of 2.5 nm, which corresponds to 0.050 nm / °C red-shift rate by linear fitting. For comparison, we obtain the red-shift rate of 0.086 nm / °C from 12-fold QPhC D_2 microcavity without nano-post as shown in the same figure, which is larger than 0.050 nm / °C of microcavity with nano-post under the same pump condition. Thus, we can conclude that the nano-post plays the role of heat sink and improves the heat dissipation indeed.

Due to the improved thermal properties obtained in experiments above, we then increase the duty cycle of pump source for the goal of CW operation. The measured $L\text{-}L$ curves when the pump duty cycle is varied from 0.5 to 16.0 % are shown in Fig. 4-21(a). When the pump duty cycle is increased to 8.0 %, the threshold increases as shown in Fig. 4-21(b) but there is no significant change in slope efficiency compared with that when the pump duty cycle is 0.5 %. However, when the pump duty cycle further increases to 16.0 %, the threshold increases to 1.0 mW and the slope efficiency decreases significantly, as shown in Fig. 4-21(a). The increase of threshold and decrease of slope efficiency could be both attributed to the similar reasons of the degradations due to the increased substrate temperature mentioned in the previous paragraph. Besides, we also observe broadened spectral line width with increased pump duty cycle near threshold as shown in Fig. 4-21(b), which directly indicates the increase of microcavity temperature with the increase of pump duty cycle. When the pump duty cycle further increases to 20.0 %, the $WG_{6,\,1}$ mode lasing action is not always observed and the MQWs are destroyed when the pump duty cycle is larger than 20.0 %. Although the CW
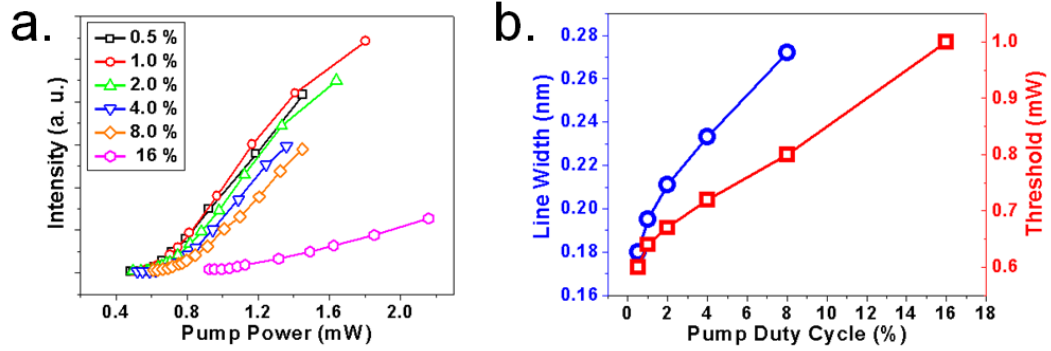
Fig. 4-21: (a) *L-L* curves of microcavity with nano-post beneath under different pump duty cycles from 0.5 to 16.0 %. (b) The relationships of the pump duty cycle versus the spectral line width and the threshold. Both spectral line width and threshold increase with the increasing pump duty cycle.

operation is not available in this study, it is evident that the nano-post plays an efficient heat sink and improves the thermal performances of 12-fold QPhC D_2 microcavity. Thus, we still believe the CW operation can be obtained by this design with optimizations, for example, MQWs gain peak (near 1550 nm at room temperature) alignment with the microcavity resonance, improvement of fabrication imperfections, and so on.

Up to date, various excellent PhC nano- and micro-cavities operated in CW mode have been demonstrated [12, 22, 99, 100]. However, most of them still lack proper electrically-driven approaches. As a result, based on this nano-post structure, we believe the realization of electrically-driven PhC microcavity laser under CW operation can be strongly expected. The nano-post can play the roles of current pathway and heat sink at the same time.

4-3 Summary

In this chapter, we investigate the resonance behaviors of 12-fold QPhC D_2 microcavity by 3D FDTD method. High simulated and measured *Q* factors of 38,000 and 10,000 from $WG_{6, 1}$ mode are obtained in FDTD simulations and experiments, respectively. From the well-fabricated devices, we obtain and identify the $WG_{6, 1}$ single mode lasing with low

threshold and high Q factor of 0.15 mW and 10,000. We also investigate and confirm the strong $WG_{6,1}$ mode dependence on the cavity geometry both in experiments and simulations by randomly varying the positions of twelve nearest air-holes and outer air-holes separately. Besides, we design and demonstrate twin and triple 12-fold QPhC D_2 microcavities, which could be served as the basis of constructing CROW devices in PICs. In experiments, we successfully obtain and identified the PM modes in each design.

On the other hand, $WG_{6,1}$ mode with significant zero-field distribution region can be a good mode candidate for microcavity laser with nano-post for electrical driving. By FDTD and FEM method, we investigating Q factor degradation and heat dissipation improvement of $WG_{6,1}$ mode induced by different nano-posts beneath the microcavity. According to the simulated results, we can conclude that there will be the best performance when the nano-post size is equal to $1.6a$ in diameter. By well-controlled wet-etching process and proper pattern design, we fabricate microcavities with various nano-post sizes. In measurements, the measured WG mode lasing performance degradation due to different nano-posts agrees with the FDTD simulated results. For experimental thermal characterizations, the $WG_{6,1}$ mode lasing action from microcavity with nano-post size $D = 830$ nm is still observed when the substrate temperature is as high as 70 °C. And we also obtain lower lasing wavelength red-shift rate of 0.050 nm / °C than that from microcavity without nano-post beneath when varying the substrate temperature. Besides, the $WG_{6,1}$ mode lasing action is still observed when the pump duty cycle is up to 16.0 %. Thus, we believe the realization of electrically-driven PhC microcavity laser under CW operation can be strongly expected based on this post structure, where the nano-post plays the roles of current pathway and heat sink at the same time.

Whispering-Gallery Modes in Photonic Crystal-Based Micro- and Nanocavities

In this chapter, base on the strong whispering-gallery (WG) mode dependence on cavity geometry we investigated in Chapter 4, we propose a photonic crystal (PhC) circular-shaped microcavity sustaining a high quality (Q) factor WG mode. The modal properties and lasing actions of sustained WG mode are investigated and obtained in numerical simulations and experiments, respectively. Due to the presence of WG mode, we initiatively investigate the uniform coupling property between the microcavity and the different inserted waveguides geometries both in simulations and experiments. Besides, in numerical simulations, we propose an idea of applying this PhC microcavity design on a double-layered structure for serving as a highly sensitive optical stress micro-sensor. In the end of this chapter, we propose a nanocavity design sustain the lowest order WG mode with ultra-small mode volume based on square PhC lattice.

5-1 Photonic Crystal CD$_2$ Microcavity

So far, we have investigated and demonstrated various WG modes lasing actions in microcavities formed by various quasi-PhC (QPhC) lattices in Chapter 3 and 4. In measurements, all of them show the properties of high Q factors and low thresholds. However, when considering the integration in photonic integrated circuits (PICs), this kind of QPhC microcavity is difficult to integrate with the present PhC-based system due to its spatially non-periodic lattice structure. Although it is possible to realize PICs by QPhC waveguide

system [55, 101], many further investigations are required. To overcome this difficult situation, one realistic approach is to enhance or well-localize WG modes in PhC microcavity by some modifications. And the strong WG mode dependence on the cavity geometry (positions of twelve nearest air holes) in 12-fold QPhC D_2 microcavity we investigate in Chapter 4 provides us a design direction to enhance WG mode in PhC D_2 microcavity.

5-1-1　Microcavity Design & Simulated Modal Prperties

According to the WG mode dependence on cavity geometry, it is possible to sustain a WG mode in PhC D_2 microcavity by modifying the twelve nearest air holes positions as the way in 12-fold QPhC D_2 microcavity. The scheme of our design is shown in Fig. 5-1. The PhCs are formed by air holes on a thin dielectric slab and the original PhC D_2 microcavity is formed by removing seven air holes. The positions of twelve nearest air holes are rearranged to be the same with those of 12-fold QPhC D_2 microcavity. Thus, six of them are shifted inward and the others are shifted outward. The microcavity is re-named as PhC circular-D_2 (CD_2) microcavity due to its cavity shape, as shown in Fig. 5-1.
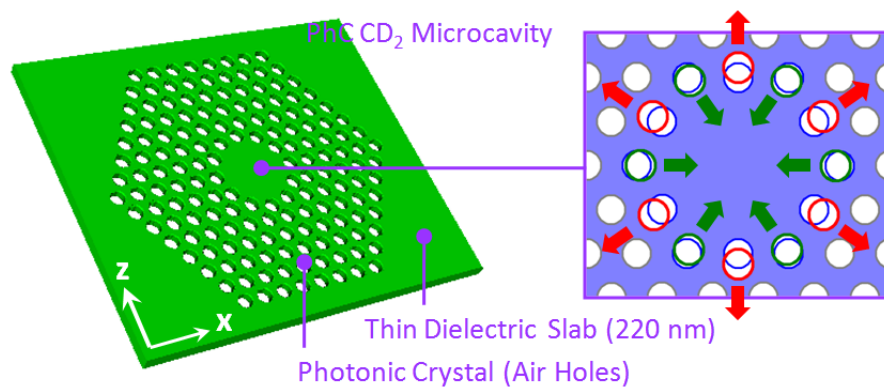
Fig. 5-1: Scheme and cavity design of PhC D_2 microcavity. The microcavity is modified from PhC D_2 to CD_2 microcavity by shifting the twelve nearest air holes inward or outward to make the spacing between air holes equal to one lattice constant.

To confirm this design, we apply three-dimensional (3D) finite-difference time-domain (FDTD) method to simulate the WG modal characteristics in PhC CD_2 microcavity. The designed lattice constant (*a*) and the air-hole radius (*r*) over *a* (*r/a*) ratio are 500 nm and 0.34. The refractive index of the dielectric material (InGaAsP) is set to be 3.4. The simulated electric- and magnetic-field distributions of sustained $WG_{6,1}$ mode whose lobes match with the gears formed by the twelve nearest air holes are shown in Fig. 5-2(a)-(c). From the mode distribution in the *x-z* plane, one can observe a significant zero-distribution region at the center of the microcavity. It is also observed from the electric field in the *x-y* plane that only a very small fraction of energy radiates into vertical directions due to the modal cancellation [102] of WG mode, which contributes to its high *Q* factor. This can also be seen from the electric-field distribution in the wave-vector (*k*) space by Fourier transformation, as shown in Fig. 5-2(d). Only very few leaky components are inside the light cone. The simulated *Q* factor and effective mode volume are 36,000 and $1.6(\lambda/n)^3$, respectively. We also calculate other resonance modes in PhC CD_2
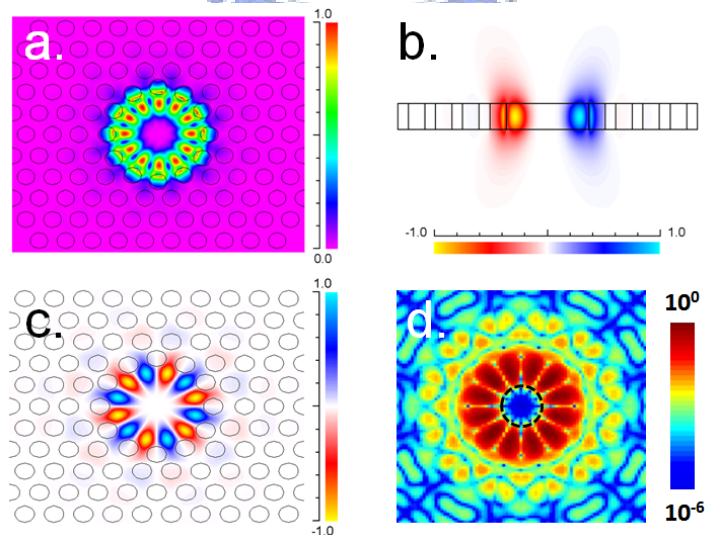
Fig. 5-2: 3D FDTD simulations of $WG_{6,1}$ mode in PhC D_2 microcavity. Electric-field distribution in (a) *x-z* and (b) *x-y* planes. (c) Magnetic-field distribution in the *x-z* plane. (d) $WG_{6,1}$ mode electric-field distribution in *k*-space by Fourier transformation.
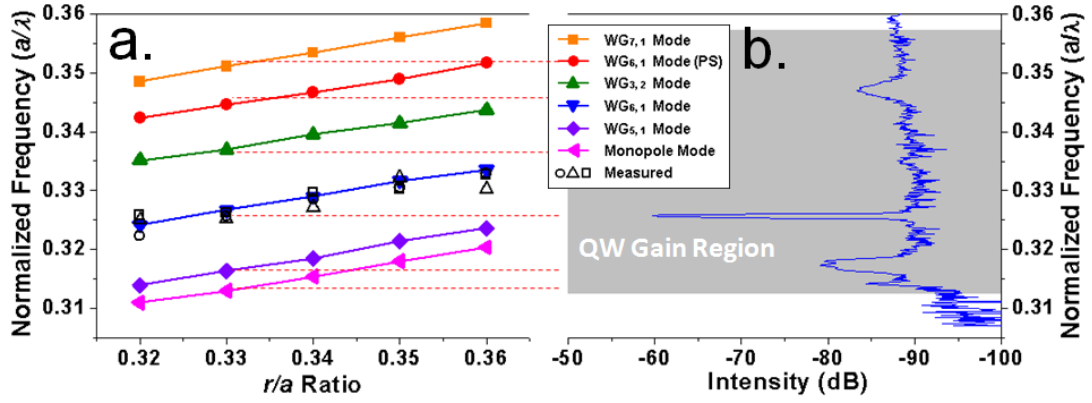
Fig. 5-3: (a) Plot of normalized frequency versus PhC r/a ratio of the resonance modes in PhC CD_2 microcavity by 3D FDTD simulations. The hollow circles, squares, and triangles denote the measured lasing actions from devices with lattice constants from 490 to 510 nm. (b) The measured resonance spectrum from well-fabricated device with lattice constant and r/a ratio of 500 nm and 0.33, respectively. The gain region of MQWs is indicated by the shadow region.

microcavity within our designed range. The plot of normalized frequency of the resonance modes versus PhC r/a ratio is shown in Fig. 5-3(a).

5-1-2   Measured Lasing Action & Mode Identification

The scanning electron microscope (SEM) pictures of well-fabricated PhC CD_2 microcavity by the fabrication process are shown in Fig. 5-4. The fabricated microcavities are optically pulse-pumped at room temperature and $WG_{6,1}$ single mode lasing action is obtained. The typical light-in light-out (*L-L*) curve of PhC CD_2 microcavity with a = 500 nm and r/a ratio ~ 0.33 is shown in Fig. 5-5(a) and the threshold can be estimated as 0.24 mW. The typical lasing spectrum at wavelength 1536 nm is shown in Fig. 5-5(b). We also show the spectrum near 0.8 times threshold in Fig. 5-5(c). The line width $\Delta\lambda_{FWHM}$ is estimated as 0.15 nm by Lorentzian fitting, which corresponds to Q factor of 10,000 by $\lambda / \Delta\lambda_{FWHM}$ in experiments [103]. Besides, the side-mode suppression-ratio (SMSR) of 18 dB is estimated from the spectrum in Fig. 5-5(d). In Chapter 3, we have proposed a simple approach to

68

increase SMSR by inserting a central air hole in the microcavity to destroy other resonance modes without affecting the WG mode. However, this approach cannot be applied here because the main side mode observed in longer wavelength in Fig. 5-5(d) is $WG_{5,1}$ mode. Nevertheless, the side mode reduction can be still achieved by other loss mechanism managements [104, 105].

In mode identification, to confirm the lasing mode is $WG_{6,1}$ mode, we increase the sensitivity of the optical spectrum analyzer to collect the weak radiations from other
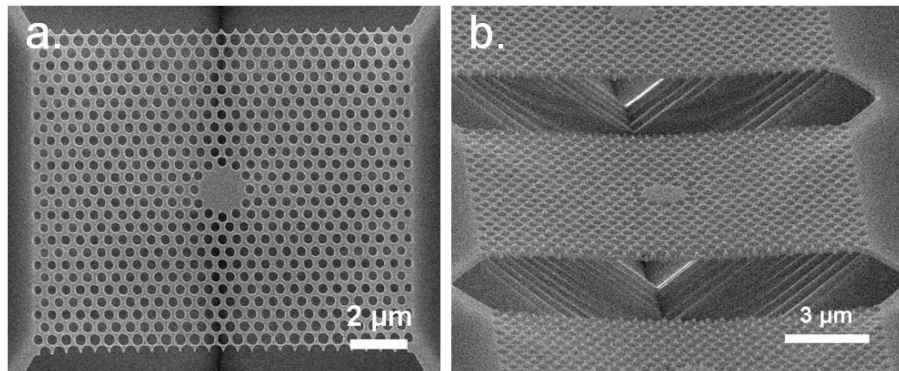
Fig. 5-4: (a) Top- and (b) tilted-view SEM pictures of fabricated PhC CD_2 microcavity lasers. The fabricated lattice constant and r/a ratio are 500 nm and 0.33, respectively.
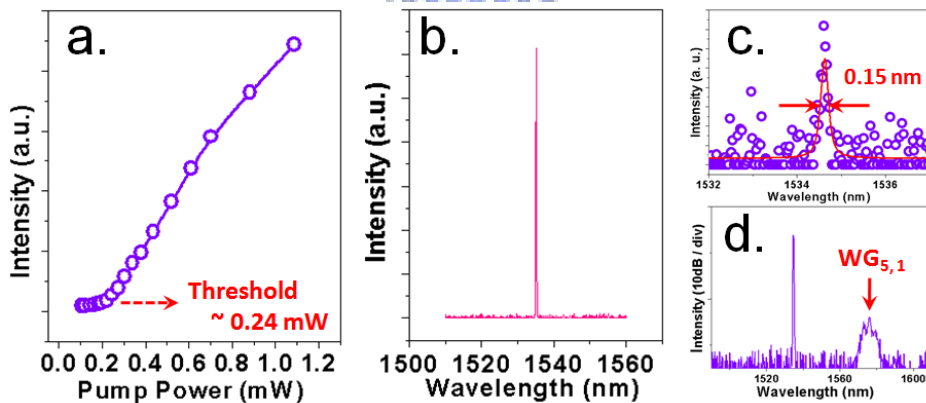
Fig. 5-5: (a) Typical L-L curve and (b) lasing spectrum at 1536 nm of PhC CD_2 microcavity laser. The threshold can be estimated as 0.24 mW from the L-L curve. The measured Q factor can be estimated as 10,000 from the line width of 0.15 nm in (c) the spectrum near threshold. The SMSR is also estimated as 18 dB from (d) the lasing spectrum in dB scale.

resonance modes of the microcavity. The measured lasing spectrum in decibel scale is shown in Fig. 5-3(b). Comparing it with the 3D FDTD simulation results in Fig. 5-3(a), we obtain a very good match and clearly identify the lasing mode as $WG_{6,1}$ mode. Almost all resonance modes are observed and identified except for $WG_{7,1}$ mode near the gain region edge of multi-quantum-wells (MQWs). Besides, statistical measured lasing actions with $a = 490 - 510$ nm and r/a ratio $= 0.32 - 0.36$ are also obtained and denoted by hollow circles, squares, and triangles (different shapes mean different lattice constants) in Fig. 5-3(a), which also match with the FDTD simulated results quite well. The slight normalized frequency differences between measured and simulated results are arisen from the fabrication imperfections and the estimation inaccuracy from SEM pictures.

5-1-3   Uniform Coupling Properties

The PhC-based microcavity-waveguide structure [106, 107] is an important basic building block for various applications in PICs, such as optical interconnectors, couplers, optical buffers, and so on. Moreover, it is also a critical approach to convert most present PhC microcavity lasers with vertical emissions to in-plane emissions in planar PICs. One of the key issues is the efficient coupling between the cavity and the waveguide. For efficient coupling, not only the mode frequencies but also the spatial mode distributions of cavity and waveguide should match with each other. Recently, A. Faraon *et al.* [108] and K. Nozaki *et al.* [109] have investigated high coupling efficiency between PhC single-defect waveguides and high Q PhC L_3 microcavity and point-shifted nanocavity, respectively. However, the coupling efficiencies are not uniform in different inserted waveguide geometries due to the specific resonance direction of the mode. This would be an un-neglected problem under some specific designs where multiple input/output ports are needed.
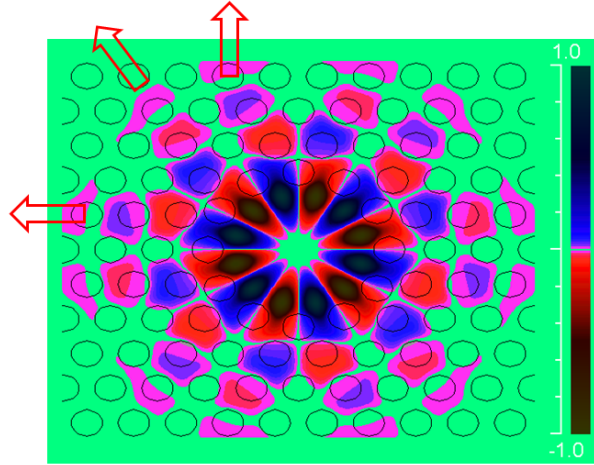
Fig. 5-6: FDTD simulated $WG_{6,1}$ mode profile reveals that the evanescent field of each lobe propagates along twelve different directions from the microcavity.

Based on PhC CD_2 microcavity, we propose our initiative design to solve this problem. It can be found that the evanescent field of each lobe of $WG_{6,1}$ mode propagates along twelve different directions from the microcavity as shown in Fig. 5-6. Intuitively, because every lobe of $WG_{6,1}$ mode is identical to each other, uniform coupling efficiencies can be obtained between the microcavity and the inserted PhC waveguides in these geometries. To investigate this uniform coupling behavior, we first numerically study the transmission of waveguide-cavity-waveguide structure in 180° line-to-line geometry (labeled as A_6 type) as shown in Fig. 5-7(a) by two-dimensional (2D) FDTD method with approximated index of 2.7. The separation between the cavity and waveguide is properly chosen as two lattice periods for the purpose of high transmission. Under the parameters of $a = 500$ nm and r/a ratio $= 0.36$, the detected transmission from the output port is around 60 %. The propagating field distribution and transmission spectrum are shown in Fig. 5-7(b) and (c), respectively. The transmission is defined as the ratio of the detected powers five lattice period distance after and before the microcavity. The transmission is also optimized by varying r/a ratio from 0.28 to 0.36. The highest transmission is over 90 % when r/a ratio $= 0.30 - 0.32$, as shown in Fig. 5-7(d). The propagation loss caused by the PhC waveguide has been considered and normalized.

71
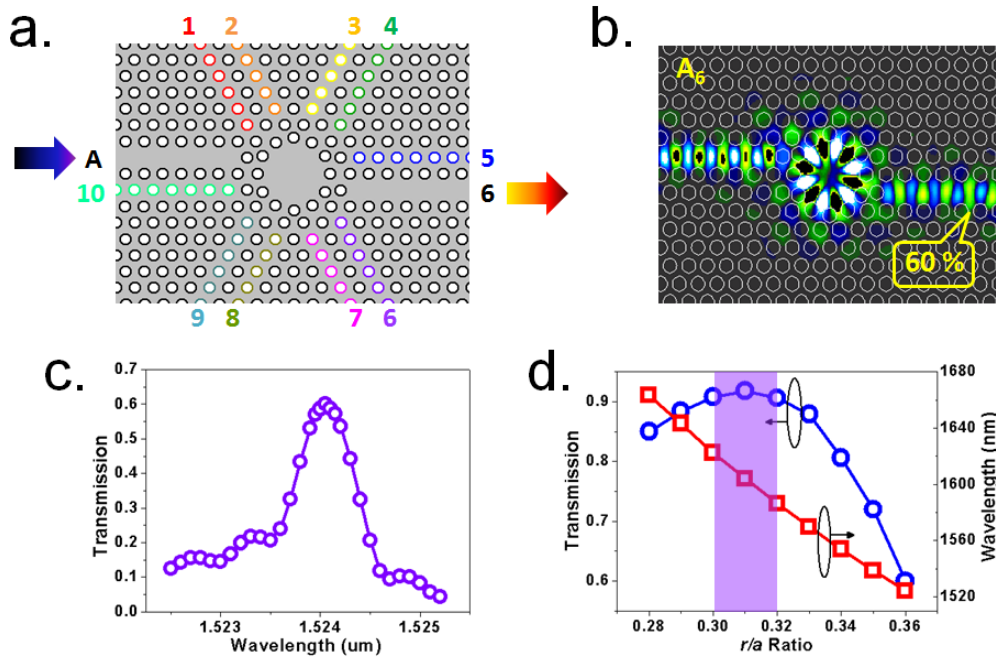
Fig. 5-7: (a) Scheme of waveguide-cavity-waveguide coupling system based on PhC CD_2 microcavity with different waveguide geometries. (Different output ports, numbered as port 1 - 10) (b) Propagating field distribution and (c) transmission spectrum of A_6 type coupler with r/a ratio of 0.36. (d) Optimization of transmission versus r/a ratio. The maximum transmission appears when r/a ratio = 0.30 - 0.32.

To initiatively confirm the uniform coupling characteristic in different propagating geometries corresponding to each WG modal lobe, we calculate the transmissions of geometries with the same input A but different output ports numbered 1 to 10 as denoted and shown in Fig. 5-7(a). The r/a ratio is set as 0.32 according to the optimization result. The simulated transmissions and wavelengths of different geometries are summarized in Table. 5-1. In Table. 5-1, the transmissions are found to be in the range of 91 – 93 %, which indicates the uniform coupling in different waveguide-cavity-waveguide geometries. We also calculate the transmission of an inserted output waveguide between ports 5 and 6 for comparison, and we find that for $WG_{6,1}$ mode, the transmission dramatically decreases to lower than 2 %. It is necessary to notice that we do not consider A_{11} type because this geometry will involve additional coupling effects for the wave propagation in the parallel waveguides [110] and make the analysis more complicated.

Table. 5-1: Transmissions and wavelengths of different waveguide-cavity-waveguide geometries named A_1 to A_{10} type.

Type	Transmission	Wavelength	Type	Transmission	Wavelength
A_1	91.9 %	1586.4nm	A_6	90.9 %	1586.2nm
A_2	91.5 %	1586.3nm	A_7	92.9 %	1586.3nm
A_3	91.9 %	1586.3nm	A_8	91.3 %	1586.3nm
A_4	92.5 %	1586.3nm	A_9	91.8 %	1586.3nm
A_5	93.0 %	1586.3nm	A_{10}	92.9 %	1586.3nm
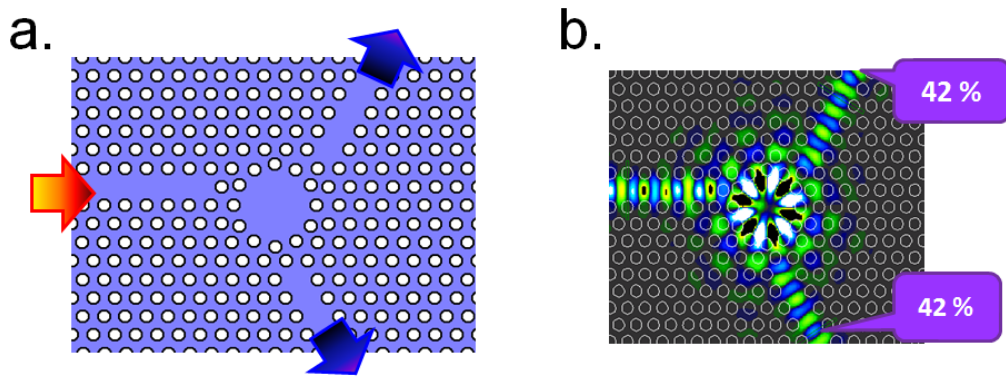
Fig. 5-8: (a) Scheme of $A_{4\text{-}8}$ coupler with power splitting function and (b) its propagating field distribution. The output powers of port 4 and port 8 are almost the same with 42 % transmission.

Based on the uniform coupling property, we also design a coupler with one input port A and two output ports 4 and 8 named $A_{4\text{-}8}$ type as shown in Fig. 5-8(a). Almost the same transmission of 42 % in each output port is achieved and the propagating field distribution is shown in Fig. 5-8(b). This indicates that PhC CD_2 microcavity with $WG_{6,\,1}$ mode combined with PhC waveguide is very suitable in designing PhC-based components that need multi-port functions.

To investigate this uniform coupling property in experiments, we fabricate PhC CD_2 microcavities with three different geometries. The SEM pictures and lasing spectra near threshold are shown in Fig. 5-9(a)-(c). The measured Q-factors degrade to around 6,900, 6,700, and 7,000 from the Lorentzian fit line width of 0.220, 0.225, and 0.215 nm near 0.8
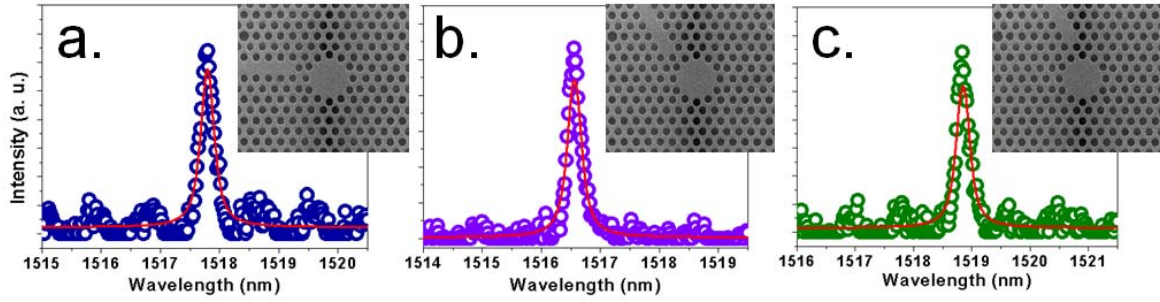
Fig. 5-9: (a)-(c) SEM pictures and measured lasing spectra near threshold of PhC CD_2 microcavities with three inserted waveguide geometries. From left to right, the Lorentzian fit line widths degrade to 0.220, 0.225, and 0.215 nm, respectively.

times threshold for the three cases. This uniform degradation also indicates the uniform coupling behavior in different cavity-waveguide geometries. We can conclude that this microcavity provides us more flexibility and freedom in designing various waveguide-cavity-waveguide geometries for applications in PICs due to its uniform coupling property.

5-2 Photonic Crystal CD_2 Microcavity for Stress Sensor Applications

Due to the high Q factor [9, 10] and small mode volume [11-13] in PhC micro- and nano-cavities, they are potential in achieving advantages of highly sensitive, portable, condensed, and so on, for serving as optical sensors. Very recently, highly sensitive optical index and particle sensors have been investigated and reported by several groups [19-23, 111-113] based on PhC micro- and nanocavities with ultra-small mode volume and high Q factors, which are potential in chemical sensing and biological labeling [114, 115]. On the other hand, optical stress sensor is another important component in mechanical and semiconductor applications, especially in micro-electromechanical systems (MEMS). Although some interesting optical stress sensor designs based on PhCs or PhC waveguides have been reported [116-120], the designs based on high Q micro- or nano-cavities are still

difficult to find in literatures and the sensitivity of present designs can be further improved.

5-2-1 Principle of Optical Stress Sensor

In optical stress sensors, according to the measured optical property change due to the structural variation, one can estimate the applied stress that leads to the corresponding structural variation. Among present reports of PhC optical stress sensors, we can roughly classify them into two categories by the detected optical property variations, optical spectrum and intensity. In the former one, researchers can measure the optical transmission spectrum shift caused by the displacement between PhC membranes [116] or by the elongated cavity length in microcavity-waveguide system on cantilever and suspended PhC membranes [117, 118] to estimate the applied stress on these structures. In the latter one, researchers can measure the transmitted optical intensity degradation due to the waveguides misalignment [119, 120] caused by the applied stress. However, in real case, there will be larger inaccuracy in measuring optical intensity variation than optical spectrum shift. Thus, estimating applied stress by optical spectrum shift would be a better and promising approach.

Generally, at first, researchers can find the relationship between the applied stress and the corresponding structural variation of their designed structure, for example, membrane displacement in ref. [116] and elongation of microcavity in ref. [117]. And then the relationship between the structural variation and the corresponding optical spectrum shift will be addressed. According to these two relationships, one can estimate the applied stress by the measured optical spectrum shift and decide how small the detectable stress variation per wavelength unit is. And the minimum detectable stress variation δF can be defined in newton unit instead of that per wavelength unit by considering the minimum spectral resolution of the measured light wave, which is decided by the measured optical line width in spectrum, or equivalently, Q factor. Thus, we can define a simple equation to illustrate this relationship:

$$\delta F = \frac{\Delta F}{\Delta d} \times \frac{\Delta d}{\Delta \lambda} \times \frac{\lambda}{Q} = \frac{\lambda}{SWQ} \qquad (5\text{-}1)$$

where $\Delta F / \Delta d$ represents the applied stress needed to cause specific structural variation and $\Delta d / \Delta \lambda$ represents the structural variation needed to cause specific optical spectrum shift, respectively. And the notations of λ, and λ / Q represent the wavelength and optical line-width in spectrum, respectively. Therefore, except for small $\Delta F / \Delta d$ and $\Delta d / \Delta \lambda$, high Q factor of the measured light wave is also necessary to achieve small δF. For simplicity, in the following investigations and discussions, we define factors of $S = \Delta d / \Delta F$ and $W = \Delta \lambda / \Delta d$ to represent the structural variation rate due to the applied stress and wavelength shift rate due to the structural variation, respectively. And the δF can be expressed as λ / SWQ as in equation (5-1).

5-2-2 Structure Design, Simulated Modal Behaviors, and Sensing Resolution

We propose a double-layered (DL) PhC membrane microcavity design with air-gap distance d, as shown in Fig. 5-10, based on the PhC CD_2 microcavity with $WG_{6,1}$ mode proposed in Chapter 5-1. The PhC CD_2 microcavity design and $WG_{6,1}$ mode profile in electric-field are both shown in the insets A and B of Fig. 5-10. At first, the modal properties of DL PhC membrane microcavity are investigated by 3D FDTD method. The simulated domain is $24a \times 24a \times 12a$ with $a/16$ computed grid size. And the PhC r/a ratio, lattice constant, and d are set to be 0.32, 420, and 440 nm, respectively. The simulated bonding and anti-bonding modes profiles in electrical field in x-z plane based on $WG_{6,1}$ mode are shown in Figs. 5-11(a) and (b), which can be analog to the electronic bonding and anti-bonding states in chemical molecules. This "photonic molecule" design has been widely considered and investigated as the key component to construct logical PICs in different micro-structures as

we have mentioned in Chapter 4-1-3. This DL structure can be realized by MEMS technologies [120] and is potential for integrating in PICs.

As we mentioned before, at first, we need to know the wavelength shift rate $W = \Delta\lambda / \Delta d$ arisen from the structural variation first. In our design, the air-gap distance d between the membranes is the structural variation parameter. In 3D FDTD simulations, d is varied from 165 to 660 nm. The relationship between d and the simulated resonance wavelength are shown in Fig. 5-11(c), which can be directly analog to the relationship between energy states and distance between atoms in chemical molecules. In Fig. 5-11(c), due to the weakened
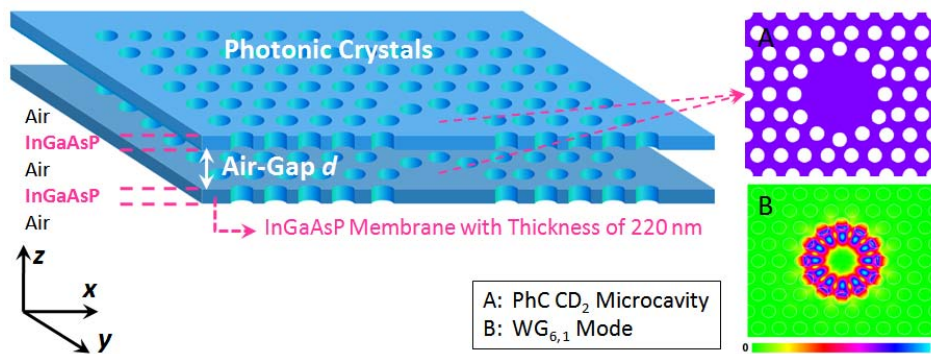
Fig. 5-10: Scheme of DL PhC CD_2 microcavity design. The microcavity design and the simulated $WG_{6,1}$ mode profile in electric-field are shown in the right inset-*A* and -*B*.
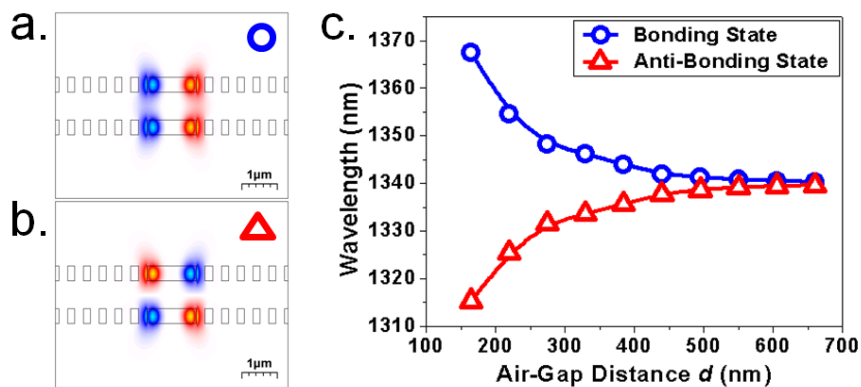
Fig. 5-11: The simulated mode profiles in electric-field in *x-z* plane of (a) bonding and (b) anti-bonding modes. (c) The simulated wavelengths of bonding and anti-bonding modes versus the air-gap distance *d*.

waveguide evanescence coupling when these two membranes become far apart, the optical mode will tend to act like the original $WG_{6,1}$ mode in single membrane and the wavelength difference between the bonding and anti-bonding modes becomes smaller when d increases. Thus, there will be different wavelength shift rate W under different d and the W factor will decrease when d increases. The calculated W factor at different d is shown in Fig. 5-12 for the bonding mode. For example, the W factors are found to be 0.235 and 0.007 nm optical spectral shifts of bonding mode for 1 nm air-gap d decreasing when the initial $d = 165$ and 550 nm, respectively. These values are higher than previous reports [116-118], which also indicate the strong optical spectral response of this DL structure in serving as an optical stress sensor. As a result, we can say that high sensitivity (small δF) can be achieved in our design by choosing small d (large W factor). However, as we mentioned in equation (5-1), in terms of optical properties, the δF is not only determined by the W factor but also by the Q factor.

Thus, we calculate the Q factors of bonding and anti-bonding modes when $d = 440$ nm. We obtain high Q factors of 75,200 and 22,700 from bonding ($Q_{bonding}$) and anti-bonding modes, respectively. The former one is even higher than that of $WG_{6,1}$ mode ($\sim$ 36,000) in original PhC CD_2 microcavity. Again, according to equation (5-1), high Q factor is benefit to obtain small δF. Therefore, in the following investigations, we will focus on the bonding mode with high Q factor. The simulated $Q_{bonding}$ with d varied from 165 to 660 nm is shown in Fig. 5-12. There are two main effects on $Q_{bonding}$ variation, waveguide evanescence coupling between two PhC membranes and optical coupling to transverse magnetic (TM) mode due to the symmetry breaking for individual PhC membrane. For small d, TM mode coupling will contribute extra optical loss and lead to low Q factor smaller than that in original PhC CD_2 microcavity. TM mode coupling loss decreases when d increases, and we observe a continuous increase of Q factor. When d is too large, Q factor decreases due to weakened waveguide evanescence coupling. As a result, in Fig. 3, we obtain a maximum $Q_{bonding}$ of 110,000 when $d = 550$ nm. Although the highest $Q_{bonding}$ is available when $d = 550$ nm, the W
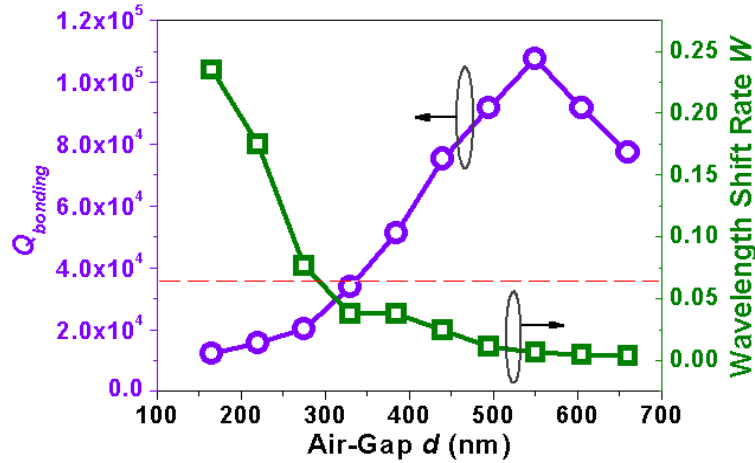
Fig. 5-12: The simulated $Q_{bonding}$ (open circle) for air-gap distance d varied from 165 to 660 nm. High $Q_{bonding} \sim 110,000$ is obtained when $d = 550$ nm. The wavelength shift rate W (open square) under different d is also presented, which decreases when the two membranes become far apart. The original Q factor ($\sim 36,000$) of $WG_{6,1}$ mode in single-membrane PhC CD_2 microcavity is also denoted by the red horizontal dash-line.

factor at this d value is smaller than the cases with small d. Since the δF in equation (5-1) depends both on the Q and W factors, we can conclude there will be an optimal design range for small δF according to the trade-off between $Q_{bonding}$ and the W factor.

So far, we have investigated and obtained the wavelength shift rate W and $Q_{bonding}$ under different d. And then we will find the relationship between the applied stress and corresponding structural variation by finite-element method (FEM) [121] simulations. We present a DL geometric design named bridge-with-wings (BwWs), as shown in Fig. 5-13. Both membranes are with thickness of 220 nm and other designed dimensions are shown in Fig. 5-13. In this BwWs geometric design, the PhC microcavities and the point stress are defined and applied on the wing and bridge regions, respectively. Two wings with PhC patterns are designed in Fig. 5-13 due to the need for structural balance and only one wing is needed in stress sensing. The structural behavior of above structure with BwWs geometry will be calculated according to Young's module by FEM and the simulation setup is illustrated as the following. The material is assumed to be isotropic, linear, and elastic. The applied point stress F and supporting are located at the center and two ends of the bridge, respectively,

according to the scheme in Fig. 5-13. The structural responses are calculated by solving material elasticity matrix according to Hoke's Law under Mindlin assumption. Some important parameters of silicon and InGaAsP, including Young's modulus (Y_0), Poisson ratio (σ), density (ρ), and thermal expansion coefficient (T), are listed in Table 5-2.

When we design the membrane geometry, two characteristics should be concerned to keep the unnecessary optical influence on PhC microcavity minimum when the stress is applied on the membrane to change the air-gap distance d. First, the air-gap displacement Δd in z-direction in PhC microcavity region should be as uniform as possible to ensure the linear relationship between F and Δd. Second, the torsion in x-y plane should be as small as possible to eliminate the elongation of PhC microcavity and distortion of PhC lattice structure, which may cause unwanted optical losses, such as PBG shift, Q factor degradation, and so on. From FDTD simulation, the in-plane Q factor of $WG_{6,1}$ mode in PhC CD_2 microcavity is close to 10^7 when the number of surrounding PhC periods is larger than 11, that is, to maintain
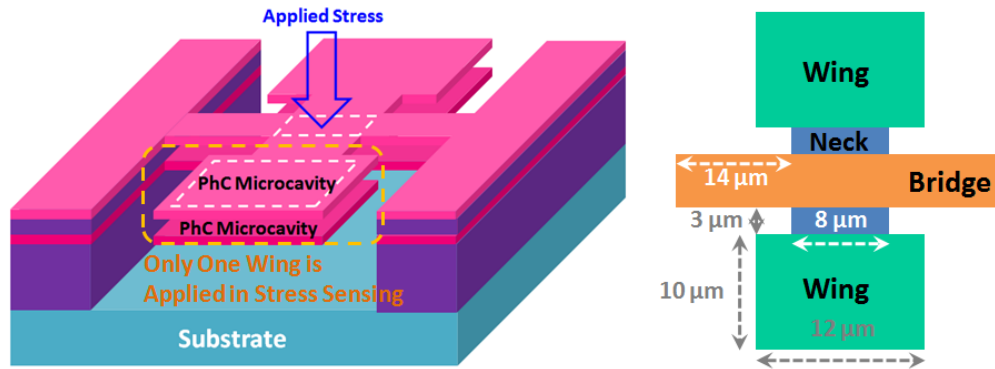
Fig. 5-13: Scheme of DL PhC microcavity in BwWs geometry. The applied stress and PhC patterns are located in bridge and wing regions, respectively.

Table. 5-2: Material parameters for silicon and InGaAsP used in FEM simulation.

Material	ρ (kg/m^3)	Y_0 (Pa)	σ	T (1/K)
Silicon	2330	1.31×10^{11}	0.27	4.170×10^{-6}
InGaAsP	4914	6.27×10^{10}	0.35	4.791×10^{-6}

sufficient in-plane PBG confinement, the PhC region should be at least $10 \times 10 \ \mu m^2$. Thus, the uniform Δd and torsion-free in $10 \times 10 \ \mu m^2$ PhC region are required.

The simulated Δd and torsion distribution when $F = 50$ nN are shown in Fig. 5-14(a) and (b). The $10 \times 10 \ \mu m^2$ PhC region mentioned above is indicated by the white dash-line enclosed region. In Fig. 5-14(a), the maximum displacement $\Delta d_{max} \sim 26.5$ nm appears at the edge of the wing. The maximum displacement difference ($\Delta d_{max} - \Delta d_{min}$) of 3.3 nm in the PhC region is along the y-direction and the uniformity $\Delta d'$ in the PhC region is only 6.6 %. In Fig. 5-14(b), significantly, the torsion mainly distributes in the bridge region and is close to zero in the wing. This torsion-free on the wing region is mainly arisen from the width design of neck region as shown in Fig. 5-13. When the width of neck region decreases, the torsion will distribute in the bridge region and not extend into the wings. This also indicates the x-y elongation in the PhC region due to torsion can be ignored in this design. Besides, the separation of stress-applying region and stress-sensing region also provides large tolerance and freedom in operation.
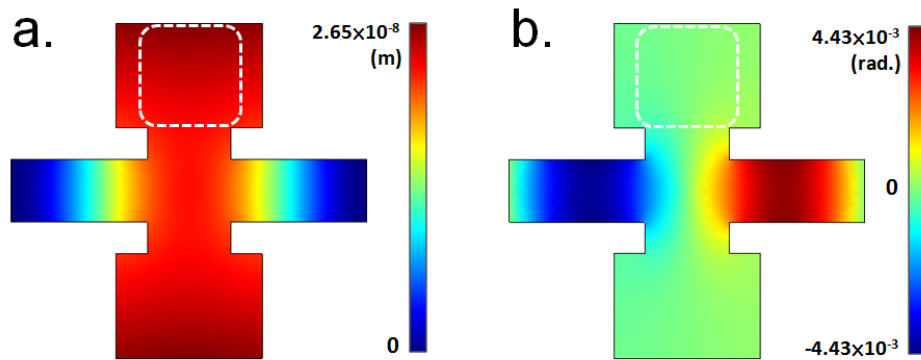
Fig. 5-14: The FEM simulated (a) air-gap displacement Δd and (b) torsion distribution of the InGaAsP BwWs geometry when $F = 50$ nN. The PhC pattern is also denoted by the white dash-line enclosed region. The torsion-free regions appear on the wings.
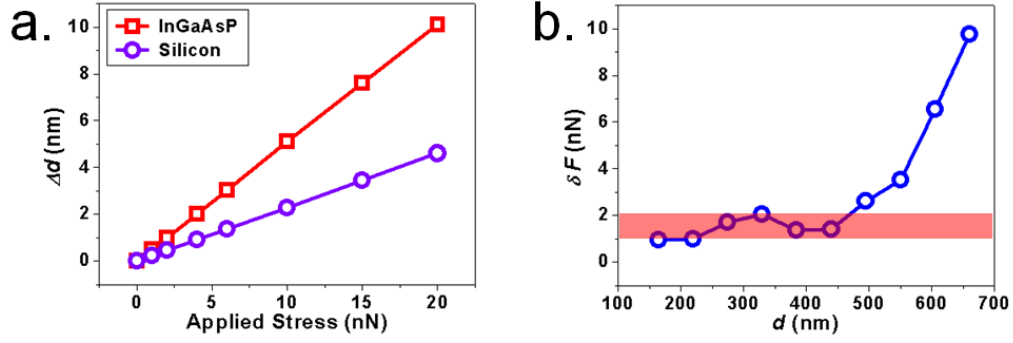
Fig. 5-15: (a) The simulated relationship between the applied stress and air-gap displacement Δd. The relationships of BwWs geometry for silicon and InGaAsP materials are presented. (b) The calculated minimum detectable stress variation δF for the BwWs geometry under different air-gap distance d.

From the FEM simulation results of above DL BwWs geometry, we can obtain the relationship between the applied stress F and the air-gap displacement Δd, as shown in Fig. 5-15(a). The calculated structural variation rate S of the BwWs geometry is 0.507 nm / nN. We also use silicon material on the same structures for comparison. The simulated result is also shown in Fig. 5-15(a). The calculated S factor of the BwWs geometry is 0.229 nm / nN, which is twice smaller than that using InGaAsP material. This means that we can have twice structural response for applied stress by using InGaAsP instead silicon under the same geometric design. This is mainly attributed to large Young's modulus of silicon, as listed in Table 5-2.

Thus, according to equation (5-1) and combining FEM and FDTD simulations, we can obtain δF from the BwWs geometry when d is varied from 165 to 660 nm, as shown in Fig. 5-15(b). The smallest δF is only 0.95 nN when $d = 165$ nm. We also find that the δF can be maintained nearly constant at a low value around 1 to 2 nN under a large range of initial d from 165 to 440 nm as indicated by the shadow region in Fig. 5-15(b), which provides a large design and fabrication tolerances in keeping high sensitivity for initial d inaccuracy after fabrication. Because of the large structural response S and optical response W, the smallest δF value in this DL design is decided by the line width (Q factor) of the WG mode. Certainly,

depending on application requirements, the δF smaller than nN level can be achieved by applying other ultra-high Q micro- and nano-cavity designs [9, 10] to the DL structure. Thus, we believe this DL structure PhC microcavity design is potential and promising in demonstrating ultra-high sensitivity optical stress sensors with large design and fabrication tolerances.

5-3   Photonic Crystal Point-Shifted D_0 Nanocavity

Due to the abilities of strongly controlling photon flow in wavelength scale, various 1D and 2D PhC nanocavities with ultra-small mode volume close to $(\lambda/2n)^3$ and high Q factors have been proposed and demonstrated [11-13, 122-124]. These nanocavities with ultra-small mode volumes are not only promising in constructing nano-scale optical laser source in PICs but also the essential of achieving threshold-less nano-lasers. Besides, it is also beneficial for enhancing interactions between light and matters in quantum-electro-dynamic researches. However, most mode candidates in above reports are mono-pole modes, which leak of proper current injection approaches. In Chapter 4, we have shown the strong potential of WG mode in achieving electrically-driven micro-laser sources by inserting a nano-post beneath the microcavity. Thus, in this section, we propose a square lattice PhC points-shifted nanocavity sustaining a lowest order $WG_{2,1}$ mode with ultra-small mode volume and large nano-post tolerance.

5-3-1 D_0 Nanocavity Design & Simulated Modal Properties

Typically, square PhC lattice has smaller PBG effect comparing with that of triangular lattice. To make sure that the defect mode will be well-confined by the PBG effect, at first, we calculate the band diagram of square lattice PhC by 3D plane-wave expansion (PWE) method. The simulated band diagram of square lattice PhC with r/a ratio of 0.38 is shown in Fig.

5-16(a). The PBG mapping extracted from the band diagrams of different r/a ratios is shown in Fig. 5-16(b). From Fig. 5-16(b), we can observed the large PBG effect when the r/a ratio is larger than 0.36 and the PBG width is proportional to the r/a ratio. Although large PBG could be obtained when r/a ratio is larger than 0.40, the PhC structure become fragile in fabrication due to the enlarged air hole radius. Thus, the r/a ration of square PhCs will be chosen as 0.38 in the following researches.

The simplest nanocavity design based on square lattice PhC is the single-defect D_1 nanocavity by removing an air hole, as shown in Fig. 5-17(a). Typically, a lowest order $WG_{2,1}$ mode will be sustained in this nanocavity design, which has been investigated [38, 125]. Recently, it has been reported that local lattice shifting in 1D or 2D PhC lattice can create various nanocavities well sustaining various ultra-small defect modes [122, 124]. In this
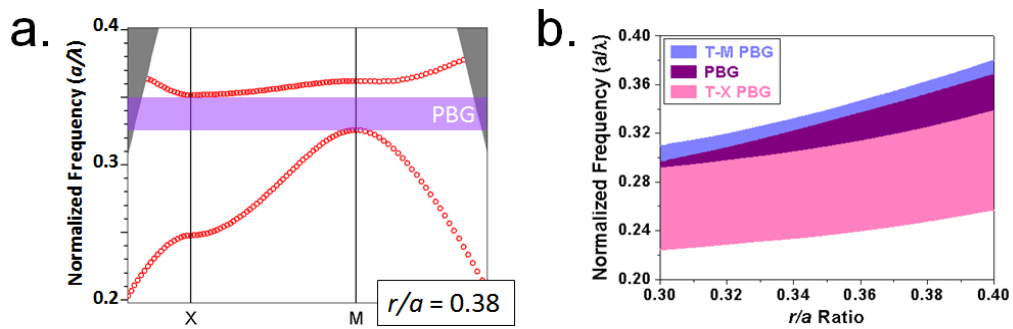
Fig. 5-16: (a) PWE simulated band diagram of square lattice PhCs with r/a ratio = 0.38. (b) The PBG mapping under different lattice orientation with r/a ratio = 0.30 – 0.40.
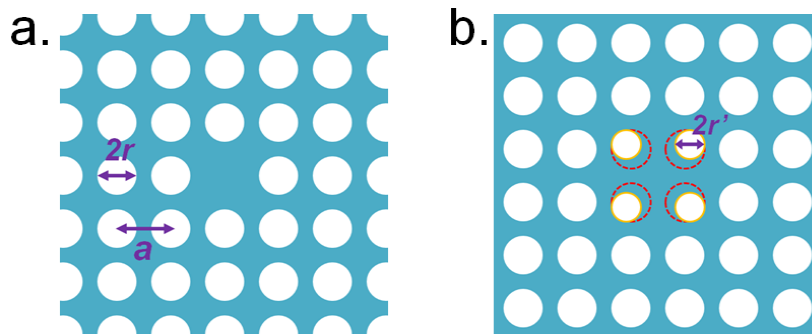
Fig. 5-17: Scheme of square PhC (a) single defect and (b) points-shifted D_0 naocavities.

section, we propose a nanocavity design in the similar approach, as shown in Fig. 5-17(b). In Fig. 5-17(b), four central air holes sizes are shrunk to be r' in radius and the positions are shifted outward to form a nanocavity region, named points-shifted D_0 nanocavity.

In 3D FDTD simulations, three defect modes are found in D_0 nanocavity, including $WG_{2, 1}$, dipole, and monopole mode. The relationship between simulated defect mode frequency and r'/a ratio of PhC D_0 nanocavity are shown in Fig. 5-18(a). All defect modes lie inside the PBG region as shown in Fig. 5-18(a). The FDTD simulated mode profiles in electrical fields of each defect mode are also shown in Fig. 5-18(b).

We also calculate Q factor and mode volume variation of $WG_{2, 1}$ mode under different r'/a ratios, as shown in Fig. 5-19(a). In Fig. 5-19(a), we can find the maximum $Q \sim 14,000$ and minimum mode volume $\sim 5.6 \ (\lambda/2n)^3$ when $r'/a = 0.30$. The calculated Purcell factor of $WG_{2, 1}$ mode under different r'/a ratio is also shown in Fig. 5-19(b). The maximum Purcell factor of 1,500 is also obtain when $r'/a = 0.30$. It is worthy to note that the mode volume of $WG_{2, 1}$ mode in this D_0 nanocavity design is smaller than that ($\sim 6.4 \ (\lambda/2n)^3$) of in D_1 nanocavity shown in Fig. 5-17(a).
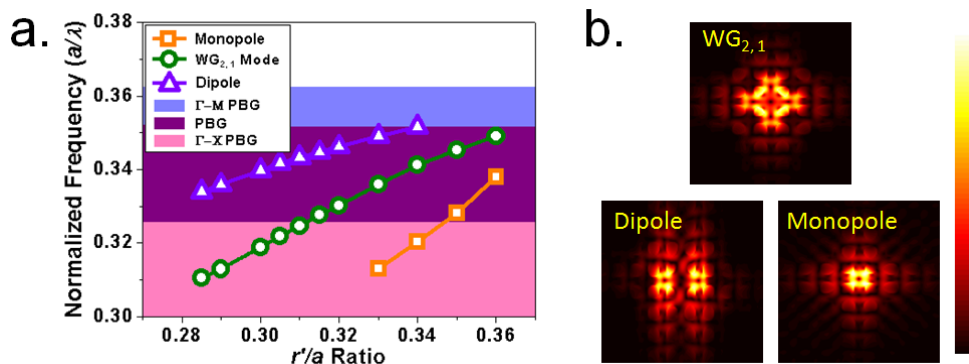
Fig. 5-18: (a) The plot of simulated defect mode frequency versus r'/a ratio in square PhC D_0 nanocavity. (b) FDTD simulated $WG_{2, 1}$, dipole, and monopole mode profiles in electric-fields.
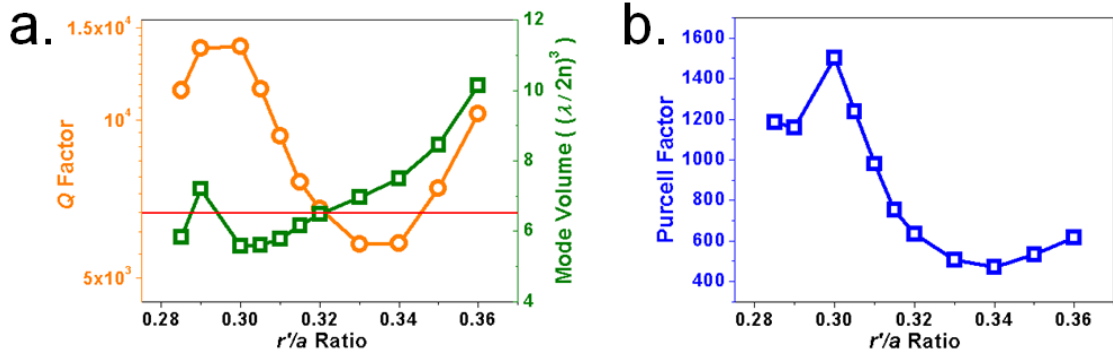
Fig. 5-19: (a) The simulated Q factor (open circles), mode volume (open squares), and (b) Purcell factor of $WG_{2,1}$ mode in D_0 nanocavity under different r'/a ratios.

Then we further investigate the tolerance of $WG_{2,1}$ mode when inserting a nano-post beneath the D_0 nanocavity. The simulated Q factor and wavelength of $WG_{2,1}$ mode under different nano-post sizes are shown in Fig. 5-20(a). There is significant degradation and variation in Q factor and wavelength when nano-post size is larger than $0.6a$ in diameter. When nano-post size is $0.6a$, the Q factor is still larger than 10,000. From the electrical field distribution of $WG_{2,1}$ mode in wave-vector space under nano-post size of $0.4a$ and $0.8a$ in diameter shown in Fig. 5-20(b), we can observe significant leaky components induced by the nano-post inside the light cone. We also show simulated Q factor variation of dipole and monopole mode in D_0 nanocavity with different nano-post sizes Fig. 5-20(a). Their Q factor both degrades to be smaller than 1,000 when the nano-post size is $0.6a$ in diameter.

Comparing with $WG_{2,1}$ mode in square PhC D_1 nanocavity, the Q factor of $WG_{2,1}$ mode in D_1 nanocavity degrades significantly when nano-post size is larger than $0.4a$. When nano-post size increases to $0.6a$, the Q factor degrades to be 5,000, which is lower than that of $WG_{2,1}$ mode in D_0 naocavity. The simulation summary of $WG_{2,1}$, dipole, monopole mode in D_0, and $WG_{2,1}$ mode in D_1 nanocavities under different inserted nano-posts beneath are shown in Table. 5-3.
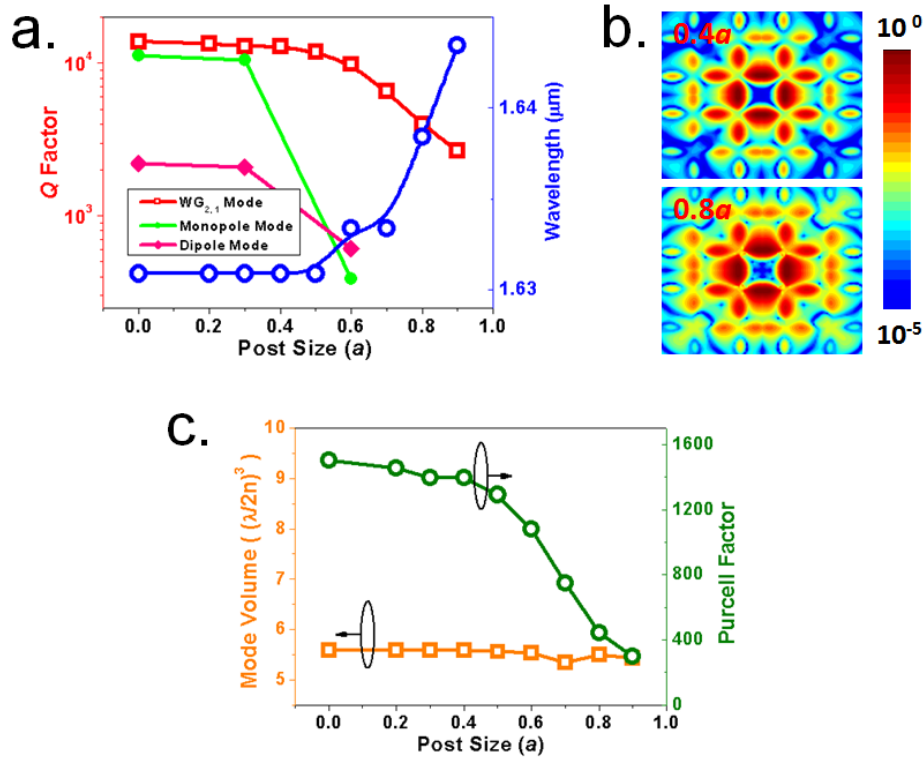
Fig. 5-20: (a) The relationships between nano-post size and Q factor and wavelength of $WG_{2,1}$ mode. The Q factor degrades to be smaller than 10,000 when the nano-post size is larger than $0.6a$ in diameter. (b) Fourier-transformed electric fields in x-z plane when the nano-post sizes are $0.4a$ and $0.8a$, which show the extra leaky components induced by larger nano-post. (c) The simulated $WG_{2,1}$ mode volume and Purcell factor under different nano-post sizes. The Purcell factor degrades to be smaller than 1,000 when the nano-post size > $0.6a$ in diameter.

Table. 5-3: (a) Q factor, (b) mode volume, and (c) Purcell factor of $WG_{2,1}$, Dipole, monopole mode in PhC D_0 nanocavity, and $WG_{2,1}$ mode in PhC D_1 nanocavity under different inserted nano-posts beneath.

a.

Q Factor

Post Size	Monopole	Dipole	$WG_{2,1}$	Single WG
0.0 a	11,236	2,195	13,821	16,390
0.3 a	10,511	2,076	12,831	16,069
0.6 a	386	607	9,847	5,187

b.

Mode Volume V ($(\lambda/2n)^3$)

Post Size	Monopole	Dipole	$WG_{2,1}$	Single WG
0.0 a	2.33	4.13	5.58	6.43
0.3 a	2.34	4.15	5.59	6.52
0.6 a	2.82	4.12	5.54	6.51

c.

Purcell Factor F

Post Size	Monopole	Dipole	$WG_{2,1}$	Single WG
0.0 a	2,936	323	1,504	1,550
0.3 a	2,725	304	1,395	1,499
0.6 a	83	90	1,081	484

From above simulation results, we can conclude that the $WG_{2,1}$ mode in our D_0 nanocavity design has smaller mode volume than that in D_1 nanocavity. Most importantly, in this design, the sustained $WG_{2,1}$ mode has larger tolerance when inserting a nano-post beneath than that in D_1 nanocavity. This large nano-post tolerance is very important in achieving good electrical and thermal properties when applying nano-post in electrically-driven structure, as we mentioned in Chapter 4-2.

5-3-2   Measurement Results & Discussions

According to the design, we fabricate square PhC D_0 nanocavities with different lattice parameters. Top-view and zoom-in SEM picture of typical fabricated PhC D_0 nanocavity are shown in Fig. 5-21(a). However, in measurements, we obtain dipole mode lasing actions instead of $WG_{2,1}$ mode after comparing the measured results with the simulated results shown in Fig. 5-18. A typical single mode lasing spectrum at 1415 nm is shown in Fig. 5-21(b). The possible reason of that we do not observe the $WG_{2,1}$ mode lasing is the fabrication imperfections. As we mentioned in Chapter 4-1, there is a very strong dependence on the cavity boundary (nearest air holes positions) for WG mode. Once the nearest air hole position is fluctuated due to fabrication imperfections, the Q factor of WG mode will be affected and degraded significantly. This effect will be more serious in a relatively small cavity like D_0
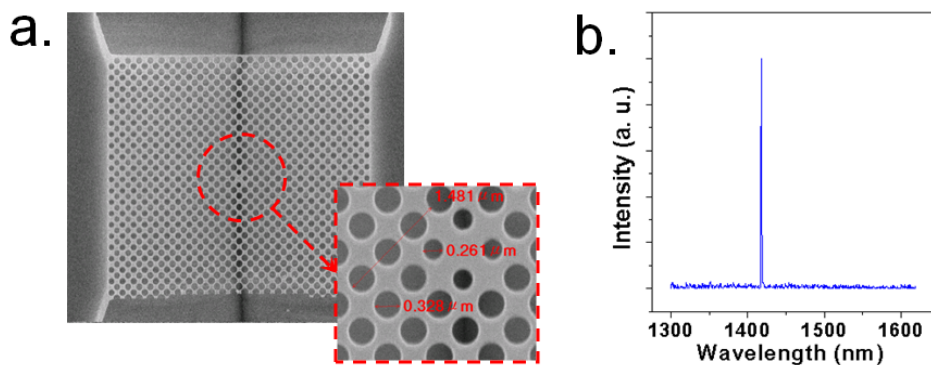
Fig. 5-21: (a) Top-, tilted-view and zoom-in SEM picture of fabricated square lattice PhC D_0 nanocavity. (b) Typical lasing spectrum form D_0 nanocavity with $r'/a = 0.29$.

nanocavity design here. Thus, to obtain $WG_{2,1}$ mode lasing actions, the fabrication imperfection, especially the nearest air hole positions, should be further optimized in the following works.

5-4 Summary

In this chapter, at first, based on the strong WG mode dependence on cavity geometry, we propose a PhC CD_2 microcavity sustaining a high Q $WG_{6,1}$ mode. In experiments, we obtain and identify $WG_{6,1}$ mode lasing actions with high Q factor of 10,000. Due to the presence of $WG_{6,1}$ mode, by the uniform transmission in simulation and Q degradation in experiments, we confirm the uniform coupling properties between the microcavity and the inserted waveguides in different geometries.

Besides, in numerical simulations, we also propose an idea of applying above PhC CD_2 microcavity on a double-layered structure for serving as a highly sensitive optical stress micro-sensor. The optical and structural responses are investing by 3D FDTD and FEM simulations. By the proposed sensing formula, the optical stress sensor with sensitivity of 0.95 nN is obtained.

In the end of this chapter, we propose a point-shifted nanocavity design sustain the lowest order $WG_{2,1}$ mode based on square PhC lattice. The smaller effective mode volume of $5.6(\lambda/2n)^3$ and larger inserted nano-post size tolerance of $0.6a$ than those of $WG_{2,1}$ mode in typical square PhC D_1 nanocavity are confirmed in 3D FDTD simulations. This design is potential in achieving electrically-driven nano-laser with good electrical and thermal properties.

<div align="right">**Chapter 6**</div>

Conclusions & Future Works

6-1 Conclusions

In this dissertation, photonic crystal (PhC) based micro- and nano-cavities sustaining whispering-gallery (WG) modes are proposed and investigated, including design, fabrication, and characterizations. At first, in Chapter 2, we introduce the well established related research resources, including numerical simulation tools and facilities for designing various PhC devices, high quality nano-fabrication process on III-V semiconductor materials, and high spectral and spatial con-focal micro-photoluminescence system with various accessories for versatile measurement requirements.

In the beginning of this dissertation, we design and fabricate various micro- and nanocavities based on quasi-PhC (QPhC), including 8-fold QPhC D_1 nanocavity and circular-PhC D_2 microcavity. The sustained WG modes in these cavities are confirmed both in simulations and experiments. Due to the isotropic photonic band gap (PBG) confinements, WG mode lasing actions with high quality (Q) factors and low thresholds are obtained, which are potential in serving as active laser sources in photonic integrated circuits (PICs). Based on 8-fold QPhC nanocavity, we also investigate several interesting properties, including side mode reduction, compact device size, and so on.

Following researches in Chapter 4, based on the designed 12-fold QPhC D_2 microcavity, we successfully obtain $WG_{6, 1}$ mode lasing actions with high Q factor of 10,000 and ultra-low threshold in experiments. We also investigate the strong $WG_{6, 1}$ mode dependence on the microcavity boundary, which is the design basis of enhancing $WG_{6, 1}$ mode in PhC micro- and nano-cavities. Besides, due to the zero-filed node of $WG_{6, 1}$ mode profile, the inserted

nano-post beneath the microcavity can be served as an efficient current pathway and provides a very promising and potential solution in electrically-driven structure. We fabricate different nano-posts under the 12-fold QPhC D_2 microcavity and investigate the optical and thermal properties. According to simulation and measurement results, we conclude an optimized nano-post size (1.6 times lattice constant in diameter) beneath the microcavity without significant laser performance degradation and with significant improved thermal properties due to the presence of nano-post.

Due to the reason of integrating in PhC-based PICs, based on the strong $WG_{6,1}$ mode dependence on microcavity boundary we investigate in Chapter. 4, we successfully project the 12-fold QPhC D_2 microcavity boundary to a PhC D_2 microcavity and enhance a well-sustained $WG_{6,1}$ mode. $WG_{6,1}$ mode lasing actions with high Q factor of 10,000 is obtained and confirmed in experiments and simulations. Due to multi-directional resonance of $WG_{6,1}$ mode, supposing this PhC CD_2 microcavity plays the role of optical transistor in planar PICs, the uniform coupling properties in different cavity-waveguide geometries are investigated and confirmed by uniform Q degradation in experiments and transmission in simulations. This property is very beneficial in PICs needs multi-port in/outputs. Based on this PhC CD_2 microcavity, in applications, we propose a double-layered structure to construct a highly sensitive optical stress sensor by the modal variation due to the gap variation between two layers. By a series of FDTD and FEM simulations, we completely present this idea and obtain high stress sensitivity of 0.95 nN.

In the end of this dissertation, we also propose a D_0 nanocavity design by locally shifting the lattice cells based on square PhCs. A lowest order $WG_{2,1}$ mode is well sustained in this nanocavity. The smaller effective mode volume of $5.6(\lambda/2n)^3$ and larger inserted nano-post size tolerance than those of $WG_{2,1}$ mode in typical square PhC D_1 nanocavity are confirmed in 3D FDTD simulations. These properties indicate the potential of realizing a nano-laser

source in PICs, which is also expected for good electrical and thermal properties in electrical driving.

6-2　Future Works & Suggestions

In this dissertation, although the basic WG modal properties in various PhC and QPhC micro- and nano-cavities have been demonstrated and investigated, many further investigations are needed to promote these devices into real applications.

In Chapter 3-2, we propose the approach of inserting a central air hole in the nanocavity, which is served as the side mode reducer to increase side-mode suppression ratio. In addition to a side mode reducer, this central air hole can also be served as the sensing core in index or bio-sensors. Due to the environmental analyte influences on the WG modal energy extends into the central air hole, the corresponding optical variation can be observed and used for sensing functionality. By integrating with the uniform coupled waveguides we investigate in Chapter 5-1, the optical sensor module with input/output could be realized in passive system.

In Chapter 4-2, we have investigated the optical and thermal properties when inserting nano-posts beneath the 12-fold QPhC D_2 microcavity. This nano-post structure is very potential in achieving electrically-driven QPhC microcavity lasers. In the following works, the current injection structure and the related fabrication processes have to be designed and developed. Besides, the 12-fold QPhC D_2 microcavity has not optimized yet. By proper optimizations, the trade-off between Q factor and heat sink should be further improved. Thus, the nano-post size tolerance could further increases and improves the heat sink. As a result, the electrically-driven QPhC microcavity laser under CW operation can be strongly expected in near future.

References

[1]   A. K. Dutta, N. K. Dutta, and M. Fujiwara, "WDM Technologies: Active Optical Components," *Academic Press* (2002).

[2]   L. Pavesi and D. J. Lockwood, "Silicon Photonics," *Spring-Verlag Berline Heidelberg* (2004).

[3]   L. A. Coldren and S. W. Corzine, "Diode Lasers and Photonic Integrated Circuits," *John Wiley* (1995).

[4]   Eli Yablonovitch, "Inhibited Spontaneous Emission in Solid-State Physics and Electronics," *Phys. Rev. Lett.* **58**, pp. 2059-2062 (1987).

[5]   S. John, "Strong Localization of Photons in Certain Disordered Dielectric Superlattices," *Phys. Rev. Lett.* **58**, pp. 2486-2489 (1987).

[6]   J. D. Joannopoulos, S. G. Johnson, J. N. Winn, and R. D. Meade, "Photonic Crystals: Molding the Flow of Light," *2nd Edition, Princeton Univ. Press* (2008).

[7]   K. J. Vahala, "Optical microcavities," *Nature* **424**, pp. 839-846 (2003).

[8]   O. Painter, R. K. Lee, A. Yariv, A. Scherer, J. D. O'Brien, P. D. Dapkus, and I. Kim, "Two-Dimensional Photonic Crystal Defect Laser," *Science* **284**, pp. 1819-1821 (1999).

[9]   M. Notomi and H. Taniyama, "On-demand ultrahigh-Q cavity formation and photon pinning via dynamic waveguide tuning," *Opt. Express* **16**, pp. 18657-18666 (2008).

[10]   H. Hagino, Y. Takahashi, Y. Tanaka, T. Asano, and S. Noda, "Effects of fluctuation in air hole radii and positions on optical characteristics in photonic crystal heterostructure nanocavities," *Phys. Rev. B* **79**, 085112 (2009).

[11]   K. Nozaki and T. Baba, "Lasing characteristics with ultimate-small modal volume in point shift photonic crystal nanolasers," *Appl. Phys. Lett.* **88**, 211101 (2006).

[12]   K. Nozaki, S. Kita, and T. Baba, "Room temperature continuous wave operation and controlled spontaneous emission in ultrasmall photonic crystal nanolaser," *Opt. Express* **15**, pp. 7506-7514 (2007).

[13]   H. S. Ee, K. Y. Jeong, M. K. Seo, Y. H. Lee, and H. G. Park, "Ultrasmall square-lattice zero-cell photonic crystal laser," *Appl. Phys. Lett.* **93**, 011104 (2008).

[14]   T. Yoshie, A. Scherer, J. Hendrickson, G. Khitrova, H. M. Gibbs, G. Rupper, C. Ell, O. B. Shchekin, and D. G. Deppe, "Vacuum Rabi splitting with a single quantum dot in a photonic crystal nanocavity," *Nature* **432**, pp. 200-203 (2004).

[15]   M. Notomi, H. Taniyama, S. Mitsugi, and E. Kuramochi, "Optomechanical Wavelength and Energy Conversion in High-Q Double-Layer Cavities of Photonic Crystal Slabs," *Phys. Rev. Lett.* **97**, 023903 (2006).

[16]   J. Chan, M. Eichenfield, R. Camacho, and O. Painter, "Optical and mechanical design of a "zipper" photonic crystal optomechanical cavity," *Opt. Express* **17**, pp. 3802-3817 (2009).

[17]   S. Strauf, K. Hennessy, M. T. Rakher, Y. S. Choi, A. Badolato, L. C. Andreani, E. L. Hu, P. M. Petroff, and D. Bouwmeester, "Self-Tuned Quantum Dot Gain in Photonic Crystal Lasers," *Phys. Rev. Lett.* **96**, 127404 (2006).

[18]   W. H. Chang, W. Y. Chen, H. S. Chang, T. P. Hsieh, J. I. Chyi, and T. M. Hsu, "Efficient Single Photon Source based on Quantum Dots in Photonic Crystal Nanocavity," *Phys. Rev. Lett.* **96**, 117401 (2006).

[19]   T. Sünner, T. Stichel, S. H. Kwon, T. W. Schlereth, S. Höfling, M. Kamp, and A. Forchel, "Photonic crystal cavity based gas sensor," *Appl. Phys. Lett.* **92**, 261112 (2008).

[20]   D. F. Dorfner, T. Hürlimann, T. Zabel, L. H. Frandsen, G. Abstreiter, and J. J. Finley "Silicon photonic crystal nanostructures for refractive index sensing," *Appl. Phys. Lett.* **93**, 181103 (2008).

[21]   A. Di Falco, L. O'Faolain, and T. F. Krauss, "Chemical sensing in slotted photonic crystal heterostructure cavities," *Appl. Phys. Lett.* **94**, 063503 (2009).

[22]   S. H. Kim, J. H. Choi, S. K. Lee, S. H. Kim, S. M. Yang, Y. H. Lee, C. Seassal, P. Regrency, and P. Viktorovitch, "Optofluidic integration of a photonic crystal nanolaser," *Opt. Express* **16**, pp. 6515-6527 (2008).

[23]   M. R. Lee and P. M. Fauchet, "Nanoscale microcavity sensor for single particle detection," *Opt. Lett.* **32**, pp. 3284-3286 (2007).

[24]   M. Eichenfield, R. Camacho, J. Chan, K. J. Vahala, and O. Painter, "A picogram- and nanometer-scale photonic crystal opto-mechanical cavity", *Nature* **459**, pp. 550-555 (2009).

[25]   C. Lee, J. Thillaigovindan, C. C. Chen, X. T. Chen, Y. T. Chao, S. Tao, W. Xiang, A. Yub, H. Feng, and G. Q. Lo, "Si nanophotonics based cantilever sensor," *Appl. Phys. Lett.* **93**, 113113 (2008).

[26]   J. K. Yang, M. K. Seo, I. K. Hwang, S. B. Kim, and Y. H. Lee, "Polarization-selective resonant photonic crystal photodetector," *Appl. Phys. Lett.* **93**, 211103 (2008).

[27]   S. Noda, A. Chutinan, and M. Imada, "Trapping and emission of photons by a single defect in a photonic bandgap structure," *Nature* **407**, pp. 608-610 (2000).

[28]   Y. Akahane, M. Mochizuki, T. Asano, Y. Tanaka, and S. Noda, "Design of a channel drop filter by using a donor-type cavity with high-quality factor in a two-dimensional photonic crystal slab," *Appl. Phys. Lett.* **82**, pp.1341-1343 (2003).

[29]   M. Notomi, A. Shinya, S. Mitsugi, G. Kira, E. Kuramochi, and T. Tanabe, "Optical bistable switching of Si high-Q photonic-crystal nanocavities," *Opt. Express* **13**, pp. 2678-2687 (2005).

[30]   T. Tanabe, K. Yamada, K. Nishiguchi, A. Shinya, E. Kuramochi, H. Inokawa, M. Notomi, T. Tsuchizawa, T. Watanabe, H. Fukuda, H. Shinojima, and S. Itabashi, "Fast All-Optical Switching using Ion-Implanted Silicon Photonic Crystal Nanocavities," *Appl. Phys. Lett.* **90**, 031115 (2007).

[31]   A. Shinya, S. Mitsugi, T. Tanabe, M. Notomi, I. Yokohama, H. Takara, and S. Kawanishi, "All-optical flip-flop circuit composed of coupled two-port resonant tunneling filter in two-dimensional photonic crystal slab," *Opt. Express* **14**, pp. 1230-1235 (2006).

[32]   M. F. Yanik and S. Fan, "Stopping Light All Optically," *Phys. Rev. Lett.* **92**, 083901 (2004).

[33]   Y. Tanaka, J. Upham, T. Nagashima, T. Sugiya, T. Asano and S. Noda, "Dynamic control of the Q factor in a photonic crystal nanocavity," *Nat. Mater.* **6**, pp. 862-865 (2007).

[34]   T. Tanabe, M. Notomi, H. Taniyama, and E. Kuramochi, "Dynamic Release of Trapped Light from an Ultrahigh-Q Nanocavity via Adiabatic Frequency Tuning," *Phys. Rev. Lett.* **102**, 043907 (2009).

[35]   A. Shinya, S. Matsuo, Yosia, T. Tanabe, E. Kuramochi, T. Sato, T. Kakitsuka, and M. Notomi, "All-optical on-chip bit memory based on ultra high Q InGaAsP photonic crystal," *Opt. Express* **16**, pp. 19382-19387 (2008).

[36]   T. Baba, M. Fujita, A. Sakai, M. Kihara, and R. Watanabe, "Lasing characteristics of GaInAsP-InP strained quantum-well microdisk injection lasers with diameter of 2-10 μm," *IEEE Photon. Technol. Lett.* **9**, pp. 878-880 (1997).

[37]   H. G. Park, J. K. Hwang, J. Huh, H. Y. Ryu, S. H. Kim, J. S. Kim, and Y. H. Lee, "Characteristics of modified single-defect two-dimensional photonic crystal lasers," *IEEE J. Quantum Eletron.* **38**, pp. 1353-1364 (2002).

[38]   H. Y. Ryu, J. K. Hwang, and Y. H. Lee, "The smallest possible whispering-gallery-like mode in the square lattice photonic-crystal slab single-defect cavity," *IEEE J. Quantum Electron.* **39**, pp. 314-322 (2003).

[39]   R-SOFT Design Group: http://www.rsoftdesign.com/

[40]   Photon Design: http://www.photond.com/

[41]   D. K. Cheng, "Field and Wave Electromagnetics," *2nd Edition, Addison-Wesley,* (1989).

[42]   K. Yee, "Numerical solution of initial boundary value problems involving Maxwell's equations in isotropic media," *IEEE Trans. Antennas and Propagation* **14**, pp. 302-307 (1966).

[43] W. H. Guo, Y. Z. Huang, and Q. M. Wang, "Resonant frequencies and quality factors for optical equilateral triangle resonators calculated by FDTD technique and Padé approximation," *IEEE Photon. Technol. Lett.* **12**, pp. 813-815 (2000).

[44] Y. Akahane, T. Asano, B. S. Song, and S. Noda, "Fine-tuned high-Q photonic-crystal nanocavity," *Opt. Express* **13**, pp.1202-1214 (2005).

[45] O. Painter, A. Husain, A. Scherer, P. T. Lee, I. Kim, J. D. O'Brien, and P. D. Dapkus, "Lithographic Tuning of a Two-Dimensional Photonic Crystal Laser Array," *IEEE Photon. Technol. Lett.* **12**, pp. 1126-1128 (2000).

[46] J. R. Cao, P. T. Lee, S. J. Choi, J. D. O'Brien, and P. D. Dapkus, "Lithographic Fine Tuning of VCSEL Pumped 2-D Photonic Crystal Lasers," *J. Nanosci. Nanotechnol.* **2**, pp. 313-315 (2002).

[47] Y. S. Choi, S. K. Kim, S. H. Kim, H. G. Park, Y. H. Lee, I. N. Kaiander, F. Hopfer, R. L. Sellin, and D. Bimberg, "Lithographic tuning of photonic-crystal unit-cell resonators with InGaAs/GaAs quantum dots emitting at 1.2μm," *J. Vac. Sci. Technol. B* **23**, pp. 252-256 (2005).

[48] M. Boroditsky, I. Gontijo, M. Jackson, R. Vrijen, E. Yablonovitch, T. F. Krauss, C. C. Cheng, A. Scherer, R. Bhat, and M. Krames, "Surface recombination measurements on III–V candidate materials for nanostructure light-emitting diodes," *J. Appl. Phys.* **87**, pp. 3497-3504 (2000).

[49] L. A. Coldren, K. Furuya, and B. I. Miller, "On the formation of planar etched facets in GaInAsP/InPdouble heterostructures," *J. Electrochem. Soc.* **31**, pp. 1918-1926 (1983).

[50] P. T. Lee, J. R. Cao, S. J. Choi, Z. J. Wei, J. D. O'Brien, and P. D. Dapkus, "Room Temperature Operation of VCSEL-Pumped Photonic Crystal Lasers," *IEEE Photon. Technol. Lett.* **14**, pp. 435-437 (2002).

[51] W. Kuang, J. R. Cao, T. Yang, S. J. Choi, P. T. Lee, John D. O'Brien, and P. D. Dapkus "Classification of Modes in Suspended Membrane 19-Missing Hole Photonic Crystal Microcavities," *J. Opt. Soc. Am. B* **22**, pp. 1092-1099 (2005).

[52] D. Cassagne, C. Jouanin, and D. Bertho, "Hexagonal photonic-band-gap structures," *Phys. Rev. B* **53**, pp. 7134-7142 (1996).

[53] A. Barra, D. Cassagne, and C. Jouanin, "Existence of two-dimensional absolute photonic band gaps in the visible," *Appl. Phys. Lett.* **72**, pp. 627-629 (1998).

[54] M. Hase, H. Miyazaki, M. Egashira, N. Shinya, K. M. Kojima, and S. Uchida, "Isotropic photonic band gap and anisotropic structures in transmission spectra of two-dimensional fivefold and eightfold symmetric quasiperiodic photonic crystals," *Phys. Rev. B* **66**, 214205 (2002).

[55]   C. Jin, B. Cheng, B. Man, Z. Li, D. Zhang, S. Ban, and B. Sun, "Band gap and wave guiding effect in a quasiperiodic photonic crystal," *Appl. Phys. Lett.* **75**, pp. 1848-1850 (1999).

[56]   M. E. Zoorob, M. D. B. Charlton, G. J. Parker, J. J. Baumberg, and M. C. Nett, "Complete photonic band-gaps in 12-fold symmetric quasicrystals," *Nature* **404**, pp. 740-743 (2000).

[57]   K. Nozaki and T. Baba, "Quasiperiodic photonic crystal microcavity lasers," *Appl. Phys. Lett.* **84**, pp. 4875-4877 (2004).

[58]   J. Chaloupka, J. Zarbakhsh, and K. Hingerl, "Local density of states and modes of circular photonic crystal cavities," *Phys. Rev. B* **72**, 085122 (2005).

[59]   S. K. Kim, J. H. Lee, S. H. Kim, I. K. Hwang, Y. H. Lee, and S. B. Kim, "Photonic quasicrystal single-cell cavity mode," *Appl. Phys. Lett.* **86**, 031101 (2005).

[60]   M. Fujita and T. Baba, "Microgear laser," *Appl. Phys. Lett.* **80**, pp. 2051-2053 (2002).

[61]   K. Nozaki, A. Nakagawa, D. Sano, and T. Baba, "Ultralow Threshold and Single-Mode Lasing in Microgear Lasers and Its Fusion With Quasi-Periodic Photonic Crystals," *IEEE J. Sel. Top. Quantum Electron.* **9**, pp. 1355-1360 (2003).

[62]   W. Kuang, J. R. Cao, S. J. Choi, J. D. O'Brien, P. D. Dapkus, "Modified Suspended Membrane Photonic Crystal D3 Laser Cavity with Improved Side Mode Suppression Ratio," *IEEE Photon. Technol. Lett.* **17**, pp. 941-942 (2005).

[63]   E. Kuramochi, H. Taniyama, T. Tanabe, A. Shinya, and M. Notomi, "Ultrahigh-Q two-dimensional photonic crystal slab nanocavities in very thin barriers," *Appl. Phys. Lett.* **93**, 111112 (2008).

[64]   H. Y. Ryu, M. Notomi, G. H. Kim, and Y. H. Lee, "High quality-factor whispering-gallery mode in the photonic crystal hexagonal disk cavity," *Opt. Express* **12**, pp. 1708-1719 (2004).

[65]   J. Scheuer and A. Yariv, "Annular Bragg defect mode resonators," *J. Opt. Soc. Am. B* **20**, pp. 2285-2291 (2003).

[66]   J. Scheuer and A. Yariv, "Coupled-waves approach to the design and analysis of Bragg and photonic crystal annular resonators," *IEEE J. Quantum Electron.* **39**, pp. 1555-1562 (2003).

[67]   J. Scheuer and A. Yariv, "Circular photonic crystal resonators," *Phys. Rev. E* **70**, 036603 (2004).

[68]   D. Chang, J. Scheuer, and A. Yariv, "Optimization of circular photonic crystal cavities beyond coupled mode theory," *Opt. Express* **13**, pp. 9272-9279 (2005).

[69]   J. Zarbakhsh, F. Hagmann, S. F. Mingaleev, K. Busch, and K. Hingerl, "Arbitrary angle waveguiding applications of two-dimensional curvilinear-lattice photonic crystals," *Appl. Phys. Lett.* **84**, pp. 4687-4689 (2004).

[70]   N. Horiuchi, Y. Segawa, T. Nozokido, K. Mizuno, and H. Miyazaki, "High-transmission waveguide with a small radius of curvature at a bend fabricated by use of a circular photonic crystal," *Opt. Lett.* **30**, pp. 973-975 (2005).

[71]   S. S. Xiao and M. Qiu, "Study of transmission properties for waveguide bends by use of a circular photonic crystal," *Phys. Lett. A* **340**, pp. 474-479 (2005).

[72]   N. Horiuchi, Y. Segawa, T. Nozokido, K. Mizuno, and H. Miyazaki, "Isotropic photonic gaps in a circular photonic crystal," *Opt. Lett.* **29**, pp. 1084-1086 (2004).

[73]   M. Fujita, S. Takahashi, Y. Tanaka, T. Asano, and S. Noda, "Simultaneous Inhibition and Redistribution of Spontaneous Light Emission in Photonic Crystals," *Science* **308**, pp. 1296-1298 (2005).

[74]   X. Zhang, Z. Q. Zhang, and C. T. Chan, "Absolute photonic band gaps in 12-fold symmetric photonic quasicrystals," *Phys. Rev. B* **63**, 081105 (2001).

[75]   S. S. M. Cheng, L. M. Li, C. T. Chan, and Z. Q. Zhang, "Defect and transmission properties of two-dimensional quasiperiodic photonic band-gap systems," *Phys. Rev. B* **59**, pp. 4091-4099 (1999).

[76]   M. Bayindir, E. Cubukcu, I. Bulu, and E. Ozbay, "Photonic band-gap effect, localization, and waveguiding in the two-dimensional Penrose lattice," *Phys. Rev. B* **63**, 161104 (2001).

[77]   C. Jin, B. Cheng, B. Man, Z. Li, and D. Zhang "Two-dimensional dodecagonal and decagonal quasiperiodic photonic crystals in the microwave region" *Phys. Rev. B* **61**, pp. 10762-10767 (2000).

[78]   Y. Wang, C. Jin, S. Han, B. Cheng and D. Zhang, "Defect Modes in Two-Dimensional Quasiperiodic Photonic Crystal," *Jpn. J. Appl. Phys.* **43**, pp. 1666-1671 (2004).

[79]   C. Reese, B. Bayral, B. D. Gerardot, A. Imamoglu, P. M. Petroff, and E. Hu, "High-Q photonic crystal microcavities fabricated in a thin GaAs membrane," *J. Vac. Sci. Technol. B* **19**, pp. 2749-2752 (2001).

[80]   S. V. Boriskina, T. M. Benson, P. D. Sewell, and A. I. Nosich, "Directional Emission, Increased Free Spectral Range, and Mode Q-Factors in 2-D Wavelength-Scale Optical Microcavity Structures," *IEEE J. Sel. Top. Quantum Electron.* **12**, pp. 1175-1182 (2006).

[81]   K. P. Huy, A Morand, and P. Benech, "Modelization of the whispering gallery mode in microgear resonators using the Floquet-Bloch formalism," *IEEE J. Quantum Electron.* **41**, pp. 357-365 (2005).

[82]   M. D. Barnes, S. M. Mahurin, A. Mehta, B. G. Sumpter, and D. W. Noid, "Three-dimensional photonic "molecules" from sequentially attached polymer-blend microparticles," *Phys. Rev. Lett.* **88**, 015508 (2002).

[83]   M. Bayer, T. Gutbrod, J. P. Reithmaier, and A. Forchel, "Optical Modes in Photonic Molecules," *Phys. Rev. Lett.* **81**, pp. 2582-2585 (1998).

[84]   A. Nakagawa, S. Ishii, and T. Baba, "Photonic molecule laser composed of GaInAsP microdisks," *Appl. Phys. Lett.* **86**, 041112 (2005).

[85]   S. Ishii, A. Nakagawa, and T. Baba, "Modal Charactristics and Bistability in Twin Microdisk Photonic Molecule Lasers," *IEEE J. Sel. Top. Quantum Electron.* **12**, pp. 71-77 (2006).

[86]   S. Ishii and T. Baba, "Bistable lasing in twin microdisk photonic molecules," *Appl. Phys. Lett.* **87**, 181102 (2005).

[87]   A. Yariv, Y. Xu, R. K. Lee, and A. Scherer, "Coupled-resonator optical waveguide: a proposal and analysis," *Opt. Lett.* **24**, pp. 711-713 (1999).

[88]   S. V. Pishko, P. Sewell, T. M. Benson, and S. V. Boriskina, "Efficient Analysis and Design of Low-Loss Whispering-Gallery-Mode Coupled Resonator Optical Waveguide Bends," *IEEE J. Lightwave Technol.* **25**, pp. 2487-2494 (2007).

[89]   S. Ishii, K. Nozaki, and T. Baba, "Photonic Molecules in Photonic Crystals," *Jpn. J. Appl. Phys.* **45**, pp. 6108-6111 (2006).

[90]   D. O'Brien, M. D. Settle, T. Karle, A Michaeli, M. Salib, and T. F. Krauss, "Coupled photonic heterostructure nanocavities," *Opt. Express* **15**, pp. 1228-1233 (2007).

[91]   K. A. Atlasov, K. F. Karlsson, A. Rudra, B. Dwir, and E. Kapon, "Wavelength and loss splitting in directly coupled photonic-crystal defect microcavities," *Opt. Express* **16**, pp. 16255-16264 (2008).

[92]   M. Notomi, E. Kuramochi, and T. Tanabe, "Large-scale arrays of ultrahigh-Q coupled nanocavities," *Nat. Photonics* **2**, pp. 741-747 (2008).

[93]   H. G. Park, S. H. Kim, S. H. Kwon, Y. G. Ju, J. K. Yang, J. H. Baek, S. B. Kim, and Y. H. Lee, "Electrically Driven Single-Cell Photonic Crystal Laser," *Science* **305**, pp. 1444-1447 (2004).

[94]   M. K. Seo, K. Y. Jeong, J. K. Yang, Y. H. Lee, H. G. Park, and S. B. Kim, "Low threshold current single-cell hexapole mode photonic crystal laser," *Appl. Phys. Lett.* **90**, 171122 (2007).

[95]   P. T. Lee, J. R. Cao, S. J. Choi, Z. J. Wei, J. D. O'Brien, and P. D. Dapkus, "Operation of photonic crystal membrane lasers above room temperature," *Appl. Phys. Lett.* **81**, pp. 3311-3313 (2002).

[96]   J. Limpert, T. Schreiber, A. Liem, S. Nolte, H. Zellmer, T. Peschel, V. Guyenot, and A. Tünnermann, "Thermo-optical properties of air-clad photonic crystal fiber lasers in high power operation," *Opt. Express* **11**, pp. 2982-2990 (2003).

[97]   O. Painter and K. Srinivansan, "Polarization properties of dipolelike defect modes in photonic crystal microcavities," *Opt. Lett.* **27**, pp. 339-341 (2002).

[98]   T. Yang, S. Lipson, J. D. O'Brien, and D. G Deppe, "InAs Quantum Dot Photonic Crystal Lasers and Their Temperature Dependence," *IEEE Photon. Technol. Lett.* **17**, pp. 2244-1246, (2005).

[99]   M. H. Shih, W. Kuang, T. Yang, M. Bagheri, Z. J. Wei, S. J. Choi, L. Lu, J. D. O'Brien, and P. D. Dapkus, "Experimental Characterization of the Optical Loss of Sapphire-Bonded Photonic Crystal Laser Cavities," *IEEE Photon. Technol. Lett.* **18**, pp. 535-537 (2006).

[100]   M. Nomura, S. Iwamoto, K. Watanabe, N. Kumagai, Y. Nakata, S. Ishida, and Y. Arakawa, "Room temperature continuous-wave lasing in photonic crystal nanocavity," *Opt. Express* **14**, pp. 6308-6315 (2006).

[101]   J. Romero-Vivas, D. Chigrin, A. Lavrinenko, and C. Sotomayor Torres, "Resonant add-drop filter based on a photonic quasicrystal," *Opt. Express* **13**, pp. 826-835 (2005).

[102]   S. G. Johnson, S. Fan, A. Mekis, and J. D. Joannopoulos, "Multipole-cancellation mechanism for high-Q cavities in the absence of a complete photonic band gap," *Appl. Phys. Lett.* **78**, pp. 3388-3390 (2001).

[103]   K. Srinivasan, P. E. Barclay, O. Painter, J. Chen, A. Y. Cho, and C. Gmachl, "Experimental demonstration of a high quality factor photonic crystal microcavity," *Appl. Phys. Lett.* **83**, pp. 1915-1917 (2003).

[104]   K. Inoshita and T. Baba, "Fabrication of GaInAsP/InP Photonic Crystal Lasers by ICP Etching and Control of Resonant Mode inPoint and Line Composite Defects," *IEEE J. Sel. Top. Quantum Electron.* **9**, pp. 1347-1354 (2003).

[105]   S. K. Kim, G. H. Kim, S. H. Kim, Y. H. Lee, S. B. Kim, and I. Kim, "Loss management using parity-selective barriers for single-mode, single-cell photonic crystal resonators," *Appl. Phys. Lett.* **88**, 161119 (2006).

[106]   M. Notomi, A. Shinya, S. Mitsugi, E. Kuramochi, and H. Ryu, "Waveguides, resonators and their coupled elements in photonic crystal slabs," *Opt. Express* **12**, pp. 1551-1561 (2004).

[107]   G. H. Kim, Y. H. Lee, A. Shinya, and M. Notomi, "Coupling of small, low-loss hexapole mode with photonic crystal slab waveguide," *Opt. Express* **12**, pp. 6624-6631 (2004).

[108]   A. Faraon, E. Waks, D. Englund, I. Fushman, and J. Vuckovic, "Efficient photonic crystal cavity-waveguide couplers," *Appl. Phys. Lett.* **90**, 073102 (2007).

[109]   K. Nozaki, H. Watanabe, and T. Baba, "Photonic crystal nanolaser monolithically integrated with passive waveguide for effective light extraction," *Appl. Phys. Lett.* **92**, 021108 (2008).

[110]   I. Park, H. S. Lee, H. J. Kim, K. M. Moon, S. G. Lee, B. H. O, S. G. Park, and E. H. Lee, "Photonic crystal power-splitter based on directional coupling," *Opt. Express* **12**, pp. 3599-3604 (2004).

[111]   S. Kita, K. Nozaki, and T. Baba, "Refractiveindex sensing utilizing a cw photonic crystal nanolaser and its array configuration," *Opt. Express* **16**, pp. 8174-8180 (2008).

[112]   S. H. Kwon, T. Sunner, M. Kamp, and A. Forchel, "Optimization of photonic crystal cavity for chemical sensing," *Opt. Express* **16**, pp. 11709-11717 (2008).

[113]   S. Kim, J. Lee, H. Jeon, and H. J. Kim, "Fiber-coupled surface-emitting photonic crystal band edge laser for biochemical sensor applications," *Appl. Phys. Lett.* **94**, 133503 (2009).

[114]   F. Vollmer anf S. Arnold, "Whispering-gallery-mode biosensing: label-free detection down to single molecules," *Nat. Methods* **5**, pp. 591-596 (2008).

[115]   A. M. Armani, R. P. Kulkarni, S. E. Fraser, R. C. Flagan, and K. J. Vahala, "Label-Free, Single-Molecule Detection wih Optical Microcavities," *Science* **317**, pp. 783-787 (2007).

[116]   W. Suh, M. F. Yanik, O. Solgaard, and S. Fan, "Displacement-sensitive photonic crystal structures based on guided resonance in photonic crystal slabs," *Appl. Phys. Lett.* **82**, pp. 1999-2001 (2003).

[117]   C. K. Lee, R. Radhakrishnan, C. C. Chen, J. Li, J. Thillaigovindan, and N. Balasubramanian, "Design and Modeling of a Nanomechanical Sensor Using Silicon Photonic Crystals," *IEEE J. Lightwave Technol.* **26**, pp. 839-846 (2008).

[118]   O. Levy, B. Z. Steinberg, M. Nathan, and A. Boag, "Ultrasensitive displacement sensing using photonic crystal waveguides," *Appl. Phys. Lett.* **86**, 104102 (2005).

[119]   Z. Xu, L. Cao, C. Gu, Q. He, and G. Jin, "Micro displacement sensor based on line-defect resonant cavity in photonic crystal," *Opt. Express* **14**, pp. 298-305 (2006).

[120]   Y. Kanamori, T. Kitani, and K. Hane, "Control of guided resonance in a photonic crystal slab using microelectromechanical actuators," *Appl. Phys. Lett.* **90**, 031911 (2007).

[121]   COSMOL: http://www.comsol.com/

[122]   M. Notomi, E. Kuramochi, and H. Taniyama, "Ultrahigh-Q Nanocavity with 1D Photonic Gap," *Opt. Express* **16**, pp. 11095-11102 (2008).

[123]   P. B. Deotare, M. W. McCutcheon, I. W. Frank, M. Khan, and M. Lončar, "High Quality factor photonic crystal nanobeam cavities," *Appl. Phys. Lett.* **94**, 121106 (2009).

[124]   Z. Zhang and M. Qiu, "Small-volume waveguide-section high Q microcavities in 2D photonic crystal slabs," *Opt. Express* **12**, 3988-3995 (2004).

[125]   K. Hennessy, A. Badolato, A. Tamboli, P. M. Petroff, E. Hu, M. Atatüre, J. Dreiser, and A. Imamoğlu, "Tuning photonic crystal nanocavity modes by wet chemical digital etching," *Appl. Phys. Lett.* **87**, 021108 (2005).

Brief Biography

Tsan-Wen Lu received his B.S. and M. S. degree from the Department of Electrical Engineering, National Tsing Hua University (NTHU) and Institute of Electro-Optical Engineering in National Chiao Tung University (NCTU) in 2003 and 2005, respectively. During 2005-2009, he is advised by Prof. Po-Tsung Lee and works for his PhD degree in Institute of Electro-Optical Engineering of National Chiao Tung University. During this period, he has published over 20 articles in international journals and conferences. His research interests are focused on photonic crystal devices and their applications, including microcavitis and waveguides.

Publication List

International Journal and Proceeding Articles:

1. Chia-Ho Chen, **Tsan-Wen Lu***, and Po-Tsung Lee, "Microcavity Laser Emissions Based on Double Hetero-Structure by Locally Modulated Photonic Crystal Waveguide," *IEEE J. Lightwave Technol.* (2009). (Accepted) (**SCI IF: 2.736**)

2. **Tsan-Wen Lu***, Yi-Hua Hsiao, Wei-De Ho, and Po-Tsung Lee, "Photonic crystal hetero-slab-edge microcavity with high quality factor surface mode for index sensing," *Appl. Phys. Lett.* **94**, 141110 (2009). (**SCI IF: 3.726**)

3. **Tsan-Wen Lu*** and Po-Tsung Lee, "Ultra-high sensitivity optical stress sensor based on double-layered photonic crystal microcavity," *Opt. Express* **17**, pp. 1518-1526 (2009). (**SCI IF: 3.880**)

4. **Tsan-Wen Lu***, Po-Tsung Lee, Chung-Chuan Tseng, and Yi-Yu Tsai, "Modal property and thermal behavior of high quality factor 12-fold quasi-photonic crystal microcavity with different central post sizes," *Opt. Express* **16**, pp.12591-12598 (2008). (**SCI IF: 3.880**)

5. Po-Tsung Lee, **Tsan-Wen Lu***, Chia-Min Yu, and Chung-Chuan Tseng, "Photonic crystal circular-shaped microcavity and its uniform cavity-waveguide coupling property due to presentation of whispering gallery mode," *Opt. Express* **15**, pp. 9450-9457 (2007). (**SCI IF: 3.880**)

6. Po-Tsung Lee, **Tsan-Wen Lu***, Jyun-Hao Fan, and Feng-Mao Tsai, "High quality factor microcavity lasers realized by circular photonic crystal with isotropic photonic bandgap effect," *Appl. Phys. Lett.* **90**, 151125 (2007). (**SCI IF: 3.726**) (Selected for *Virtual Journal of Nanoscale Science & Technology,* Vol. 15, issue 17, Apr. 30, (2007))

7. Po-Tsung Lee, **Tsan-Wen Lu***, and Feng-Mao Tsai, "Octagonal Quasi-Photonic Crystal Single-Defect Micro-cavity with Whispering Gallery Mode and Condensed Device Size," *IEEE Photon. Technol. Lett.* **19**, pp. 710-712 (2007). (**SCI IF: 2.173**)

8. Po-Tsung Lee, **Tsan-Wen Lu***, Feng-Mao Tsai, and Tien-Chang Lu, "Lasing Action of Octagonal Quasi-Periodic Photonic Crystal Micro-Cavity," *J. Jpn. Appl. Phys.* **46**, pp. 971-973 (2007). (**SCI IF: 1.309**)

9. Po-Tsung Lee, **Tsan-Wen Lu***, Feng-Mao Tsai, and Tien-Chang Lu, "Investigation of whispering gallery mode dependence on cavity geometry of quasiperiodic photonic crystal microcavity lasers," *Appl. Phys. Lett.* **89**, 231111 (2006). (**SCI IF: 3.726**)

10. Po-Tsung Lee, **Tsan-Wen Lu***, Feng-Mao Tsai, Tien-Chang Lu, and Hao-Chung Kuo, "Whispering gallery mode of modified octagonal quasi-periodic photonic crystal single defect microcavity and its side mode reduction," *Appl. Phys. Lett.* **88**, 201104 (2006). (**SCI IF: 3.726**)

International Conference Presentations:

1. Yi-Hua Hsiao, **Tsan-Wen Lu***, Wei-De Ho, and Po-Tsung Lee, "High-*Q* Photonic Crystal Hetero-Slab-Edge Microcavity Laser for Index Sensing," *IEEE/OSA CLEO/QELS'09*, CTuDD4, Baltimore, Maryland, USA (2009).

2. Wei-De Ho*, Yi-Hua Hsiao, **Tsan-Wen Lu**, and Po-Tsung Lee, "Thermal Properties of Post-Size Controlled 12-Fold Quasi-Photonic Crystal Microcavity for Electrically-Driving," *IEEE/OSA CLEO/QELS'09*, CFE4, Baltimore, Maryland, USA (2009).

3. Yi-Hua Hsiao*, Wei-De Ho, **Tsan-Wen Lu**, and Po-Tsung Lee, "Two-Dimensional Photonic Crystal Slab-Edge Microcavity for Index-Sensing Applications with High Sensitivity," *OPT'08*, Sat-S8-01, Taipei, Taiwan (2008).

4. Wei-De Ho*, Yi-Hua Hsiao, **Tsan-Wen Lu**, and Po-Tsung Lee, "Characterization of Post-Size Controlled 12-Fold Quasi-Photonic Crystal Microcavity for Electrically-Driven Structure," *OPT'08*, Sat-S7-03, Taipei, Taiwan (2008). **(Best Student Oral Paper Award)**

5. **Tsan-Wen Lu***, Chung-Chuan Tseng, Yi-Yu Tsai, and Po-Tsung Lee, "Investigation on High Quality Factor 12-Fold Quasi-Photonic Crystal Microcavities with Different Central Post Sizes," IMD4, *OSA IPNRA'08*, Boston, MA. USA (2008).

6. **Tsan-Wen Lu***, Chung-Chuan Tseng, Chia-Min Yu, and Po-Tsung Lee, "Photonic Crystal Circular-Shaped Microcavity Laser with High Quality Factor Whispering-Gallery Mode and Uniform Coupling Property," F2A-4_68, *IEEE WFOPC'07*, Taipei, Taiwan (2007).

7. **Tsan-Wen Lu***, Jyun-Hao Fan, Feng-Mao Tsai, and Po-Tsung Lee, "High quality factor circular photonic crystal microcavity lasers," TuF4-5, *IEEE/OSA CLEO-PR'07*, Soeul, Korea (2007).

8. Po-Tsung Lee, **Tsan-Wen Lu***, Feng-Mao Tsai, and Tien-Chang Lu, "Lasing Action of Octagonal Quasi-Periodic Photonic Crystal Micro-Cavities" p.407, *IEEE/LEOS IPRM'06*, Princeton, N.J., U.S.A (2006).

9. **Tsan-Wen Lu***, Feng-Mao Tsai, Po-Tsung Lee, and Tien-Chang Lu, "Modified Octagonal Quasi-Periodic Photonic Crystal Single-Defect Micro-Cavity Lasers," JWB11, *IEEE/OSA CLEO/QELS'06*, Long Beach, C.A., U.S.A. (2006).

10. Feng-Mao Tsai*, Po-Tsung Lee, **Tsan-Wen Lu**, and Tien-Chang Lu, "Fabrication and Characteristics of Two-Dimensional Quasi-Periodic Photonic Crystal Lasers," CMKK6, *IEEE/OSA CLEO/QELS'06*, Long Beach, C.A., U.S.A (2006).

11. **Tsan-Wen Lu*** and Po-Tsung Lee, "Thermal Characteristics of Two-Dimensional Photonic Crystal Lasers,'' 1064, *IEEE WOCN'05*, Dubai, U.A.E (2005).

Domestic Journal and Proceeding Articles:

1. **Tsan-Wen Lu*** (盧贊文) and Po-Tsung Lee (李柏璁), "光通訊波長二維光子晶體雷射發展簡介," 物理雙月刊, 卷廿七, 頁 693-700 (2005).

Domestic Conference Presentations:

1. **Tsan-Wen Lu***, Chung-Chuan Tseng, Yi-Yu Tsai, and Po-Tsung Lee, "High Quality Factor 12-Fold Quasi-Photonic Crystal Microcavities with Different Central Post Sizes," P-31, *MBE Taiwan '08*, Hsinchu, Taiwan (2008)

2. Jung-Rong Shih*, Chia-Ho Chen, **Tsan-Wen Lu**, Po-Tsung Lee, "Modal Analysis of Double Hetero-Structure Photonic Crystal Waveguide-Resonator for In-Plane Emission," BO-032, *OPT'07*, Taichung, Taiwan (2007).

3. Yi-Yu Tsai*, Chung-Chuan Tseng, **Tsan-Wen Lu**, and Po-Tsung Lee, "12-Fold Quasi-Photonic Crystal Microcavity with Central Post," CP-007, *OPT'07*, Taichung, Taiwan (2007).

4. **Tsan-Wen Lu***, Feng-Mao Tasi, Jyun-Hao Fan, and Po-Tsung Lee, "Beyond Photonic Crystal: High Quality Microcavity Realized by Quasi-Photonic Crystal," T01-04, *SNDT'07*, Hsinchu, Taiwan (2007).

5. **Tsan-Wen Lu*,** Feng-Mao Tsai, Po-Tsung Lee, and Tien-Chang Lu, "Octagonal Quasi-Periodic Photonic Crystal Single-Defect Micro-Cavity with Whispering Gallery Mode," BO-17, *OPT'06*, Hsinchu, Taiwan (2006).

6. **Tsan-Wen Lu*** and Po-Tsung Lee, "Thermal Characteristics of Two-Dimensional Photonic Crystal Lasers," B-SA-VII-1-6, *OPT'04*, Chungli, Taiwan (2004).

(***** : Corresponding Author)